



Image Formation with Plasmonic Nanostructures

Doctoral Programme in Physics

Universitat de València

Thesis submitted by

David Pastor Calle

Supervised by

Prof. Carlos J. Zapata-Rodríguez

Prof. Juan J. Miret-Marí



VNIVERSITAT Đ VALÈNCIA

UNIVERSITAT DE VALÈNCIA

**Image Formation with Plasmonic
Nanostructures**

by

David Pastor Calle

Doctoral Programme in Physics

Facultat de Física

Departament d'Òptica i Optometria i Ciències de la Visió

April, 2015

Declaration of Authorship

I, David Pastor Calle, declare that this thesis titled, ‘Image Formation with Plasmonic Nanostructures’ and the work presented in it are my own. I confirm that:

- This work was done wholly or mainly while in candidature for a research degree at the University of Valencia.
- Where any part of this thesis has previously been submitted for a degree or any other qualification at this University or any other institution, this has been clearly stated.
- Where I have consulted the published work of others, this is always clearly attributed.
- Where I have quoted from the work of others, the source is always given. With the exception of such quotations, this thesis is entirely my own work.
- I have acknowledged all main sources of help.
- Where the thesis is based on work done by myself jointly with others, I have made clear exactly what was done by others and what I have contributed myself.

Signed:

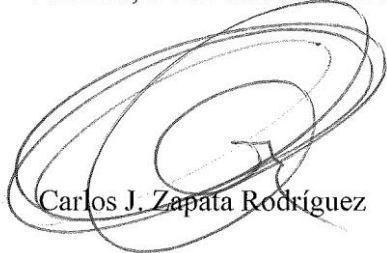
Carlos J. Zapata Rodríguez, Profesor Titular del Departamento de Òptica i Optometria i Ciències de la Visió de la Universitat de València y Juan J. Miret Marí, Profesor Titular del Departamento de Óptica, Farmacología y Anatomía de la Universitat d'Alacant,

CERTIFICAN:

Que la presente memoria “IMAGE FORMATION WITH PLASMONIC NANOSTRUCTURES” ha sido realizada bajo su dirección en el Departamento de Òptica i Optometria i Ciències de la Visió de la Universitat de València, por DAVID PASTOR CALLE y constituye su Tesis para optar al grado de Doctor por la Universitat de València.

Y para que así conste, en cumplimiento de la legislación vigente, presentan en el Departamento de Òptica i Optometria i Ciències de la Visió de la Universitat de València la referida Tesis Doctoral, y firman el presente certificado.

Valencia, a 6 de Marzo de 2015.



Carlos J. Zapata Rodríguez



Juan J. Miret Marí

To my parents Gema Calle and Paco Pastor.

In the joyful memory of my grandfather Siro Calle.

With deepest gratitude to Esther Gimeno.

“Research is what I’m doing when I don’t know what I’m doing.”

Wernher von Braun

Acknowledgements

First of all, I would like to express my deepest gratitude to my advisor Carlos J. Zapata. His passion for the research has stimulated and excited me from the very beginning. Carlos has always been a supportive advisor, and for that reason a great teacher. I also would like to thank my advisor Juan J. Miret for his support and his helpful advices, specially in numerical calculations. It has been really nice and fun to work with him. Thank you Carlos and Juan J. for your time and consideration.

Throughout these year of PhD I have met good scientists. I am grateful to Alberto Garcia to believe in me and guide my first steps in scientific research. I am indebted Ana Cros to introduce me in the experimental science and teaching me in laser spectroscopy and to Rafa Mata for introducing me how to operate the AFM. Finally, I am glad to Alejandro Molina for sharing his experience with me.

Also, I want to thank to the Department of Optics at the Faculty of Physics of the Universitat de València that gave me the possibility of making the PhD courses and to Ministerio de Economia by the financial support.

I am very grateful to my hosts during my foreign short stays at the University of Warsaw: Rafał Kotyński. His friendly behavior made me fell at home. I am also grateful to his collaborators Marek, Tomasz Stefaniuk, Piotr Wróbel, and specially to Tomasz Szoplik.

Thank you for so many persons who have crossed my path and who have helped me to grow and mature. Specially to Esther Gimeno for her affection but also to Laura, Manuel, A. Caballer, Carolina, Pablo, Vicente, Isabel, Javier, Juan, Gabriela, A. Allas, Pedro and many others.

I am grateful to my office mates by the great environment and good atmosphere. First, to my present mates Carlos and Jesus. Also to Aitor who left the office recently and with special affection to Mahin Naserpour. You left a mark on this little team and I hope we will meet again in the future.

Finally, some words of acknowledgment to my family in my mother tongue: Es un placer para mí agradecer a mi familia el apoyo demostrado. Todo lo que soy y pueda llegar a ser algún día es gracias a ella. No hay forma de agradecer lo suficiente el cariño y atención que han mostrado mis padres a la hora de educarme y ofrecerme todas las oportunidades. Han sido unos buenos guías y unos grandes amigos.

Gracias.

Resumen

En 1873, Ernst Abbe concluyó que debido a la difracción de la luz el límite de resolución de un sistema óptico es aproximadamente la mitad de la longitud de onda de trabajo [1]. Este límite, llamado el límite de difracción produce porque las ondas evanescentes no contribuyen a la formación de la imagen. En cualquier sistema óptico formado por materiales presentes en la naturaleza los detalles espaciales del objeto que sean más pequeños que el límite de resolución son transportados por ondas evanescentes. Normalmente estas ondas se pierden debido a la fuerte atenuación que experimentan viajando del objeto a la imagen.

En 1968, Veselago [2] mostró que un material con permitividad y permeabilidad negativa, es decir, con índice de refracción negativo (NIM), exhibe una serie de fenómenos poco comunes, tales como el efecto Doppler inverso, radiación de Čerenkov inversa y refracción negativa. Este último fenómeno permite a una lámina de NIM actuar como si de una lente convergente se tratase, produciendo una imagen real de objeto luminoso situado frente a la lámina. Tres décadas después, Pendry descubrió que las lentes formadas con NIMs pueden tener un límite de resolución muy por debajo de la longitud de onda. Es decir, estas lentes pueden producir imágenes perfectas en ausencia de pérdidas si la impedancia coincide con la del medio en el que están sumergidas [3, 4]. Idealmente, las lentes formadas por NIMs producen imágenes perfectas, propagando las ondas homogéneas y amplificando las evanescentes por medio de los polaritones excitados en la superficie del NIM. Esta amplificación de las ondas evanescentes compensa su decaimiento

ii Resumen

fuera del metamaterial. Llamaremos superlentes a este tipo de lentes así como cualquier otra capaz de generar imágenes cuyo límite de resolución sea menor que el límite establecido por la difracción.

La capacidad superresolvente de las lentes de índice de refracción negativo descubierta por Pendry fue cuestionada tanto teóricamente [5] como usando simulaciones numéricas [6]. La discusión versaba sobre la amplificación de los modos evanescentes que hace matemáticamente no integrables a los campos electromagnéticos en el plano imagen de la superlente. Si se tienen en cuenta las pérdidas en el NIM el problema desaparece. De hecho, los NIMs realistas siempre tienen pérdidas que no pueden ser ignoradas en los cálculos. En consecuencia, la amplificación de las ondas evanescentes en las interfases de un NIM viene siempre acompañada de la disipación de estas dentro del mismo, impidiendo su completa recuperación en el plano imagen.

Además de las pérdidas existen otros parámetros que determinan el ancho de banda espacial transmitido y por consiguiente, el poder de resolución del sistema óptico [7]. Por ejemplo, es posible aumentar la resolución con una lente plana de inmersión eligiendo una configuración asimétrica con una constante dieléctrica alta en el medio que incluye el plano imagen [8].

También se ha demostrado que cuando las permeabilidades y permitividades no son exactamente iguales (salvo signo) se pueden producir resonancias que ayudan a aumentar la resolución de la superlente [8]. También es posible aumentar la resolución mediante la reestructuración de la lente [9]. Sin embargo se cree que la introducción de materiales con ganancia es el enfoque más eficiente [4, 10–18].

La primera demostración experimental de un NIM en el rango de las microondas la realizaron Smith *et al.* [23, 24]. Su montaje experimental puede verse en la Figura 1(a). Se observó el fenómeno de la refracción negativa utilizando un NIM compuesto por una matriz de celdas unidad con un tamaño de una longitud de onda. Cada celda unidad contenía un resonador anular abierto y un hilo metálico. Posteriormente se ha mejorado este montaje usando una versión refinada de los

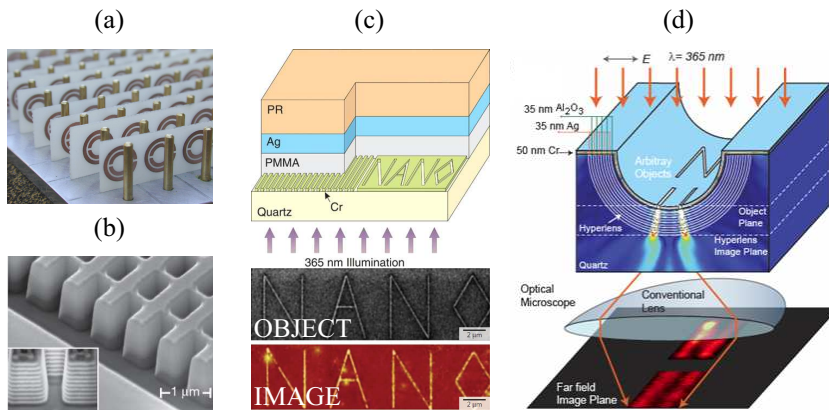


FIGURE 1: (a) Primera realización experimental de un NIM. Una estructura basada en resonadores anulares abiertos e hilos metálicos grabados en una placa (extraído de [19]). (b) Imagen SEM de una estructura fishnet con 21 capas (extraído de [20]). (c) Esquema y medidas experimentales de superresolución en una lámina de metal. La ilustración muestra una superlente óptica con una capa de plata actuando como lente (extraído de [21]). (d) Esquema de una hiperlente y simulación numérica de la formación de imágenes con resolución sub- λ (extraído de [22]).

anillos resonadores [25, 26]. Este tipo de medio sólo es eficaz para la fabricación de superlentes en el rango de microondas e infrarrojo debido a la fuerte absorción que experimenta a frecuencias más altas. Además, no poseen un μ negativo para frecuencias más allá del infrarrojo [27]. Para frecuencias mayores una estructura tipo 'fishnet' como la que se muestra en la Figura 1(b) puede sustituir a la matriz de anillos resonadores [20, 28, 29].

Todos los NIMs que se han desarrollado hasta hoy se obtienen juntando dos materiales estructurados de los cuales uno muestra permitividad negativa y el otro permeabilidad negativa. La mayoría de los estudios de metamateriales se ha centrado en conseguir un índice de refracción negativo en una banda estrecha de frecuencias, aunque también hay estudios en bandas dobles [30, 31], en multibanda [32] e incluso metamateriales sintonizables [33]. También se ha observado la refracción negativa para un amplio espectro angular en dos dimensiones a través de montajes con segmentos en forma de prisma [34, 35].

En campo cercano, es decir para frecuencias espaciales muy altas, las respuestas eléctrica y magnética de los materiales están desacopladas. Por tanto, para ondas con polarización transversal magnética (TM), sólo se necesita una permitividad negativa para formar imágenes sub- λ [3]. Los metales nobles, tales como la plata, satisfacen esta nueva condición y por tanto son candidatos naturales para el diseño de superlentes en el rango óptico. A frecuencias ópticas la permitividad de estos metales, en módulo, puede ser comparable a la permitividad del dieléctrico que lo rodee, lo que permite la excitación de plasmones polaritones de superficie (SPPs) en la interfase entre el metal y el dieléctrico. Los detalles sub- λ de la fuente se transmiten a través del sistema acoplándose a los SPPs [3, 8]. Se puede ver una realización experimental de este tipo de superlente en el montaje experimental de Fang *et al.* que se muestra en la Figura 1(c).

En particular, se han realizados experimentos que prueban la amplificación de ondas evanescentes a través de una lámina de plata [36, 37]. Los experimentos mostraron que estas ondas se amplifican hasta un espesor de las láminas que depende de la longitud de onda. Para espesores mayores la absorción tiene mayor peso y las ondas evanescentes se atenúan en lugar de amplificarse dentro del material. Sin embargo, es posible reducir los efectos de la absorción introduciendo materiales activos [11] o exfoliando la lámina original en películas más finas y distribuyéndolas entre los planos objeto e imagen como si de una matriz de superlentes elementales se tratase. Las ondas evanescentes incidentes excitan resonancias plasmónicas que a su vez transfieren esta ondas inhomogéneas por efecto túnel resonante [38–41], también llamado efecto túnel plasmónico [42]. Al amplificarse en menor medida las ondas evanescentes en cada capa se reduce la absorción en los metales, y por tanto, cuando estas estructuras se usan en formación de imágenes, este efecto contribuye a mejorar el poder de resolución del sistema [4, 43, 44].

Las superlentes compuestas por películas idénticas de metal dispuestas entre separadores dieléctricos son medios 1D metal-dieléctrico periódicos (PLMs). En estos

medios encontramos fenómenos de naturaleza plasmónica tales como la refracción negativa [45] y la formación de imágenes superresolventes [46–48]. Además, la refracción negativa y la amplificación de las ondas evanescentes no son requisitos necesarios para formar imágenes sub- λ en estos dispositivos. Los PLMs pueden diseñarse para mostrar unas curvas de isofrecuencia planas. En este caso la superlente se comporta como una guía de ondas [4]. Este régimen, llamado canalización, ha sido investigado por numerosos autores [49–52].

Desde que los PLMs fueron propuestos como candidatos para crear superlentes ha habido un gran interés en extender su rango de funcionamiento al espectro visible. Este reto ha sido abordado en varias publicaciones [39, 53–63]. La principal dificultad en el diseño de estos dispositivos son las grandes pérdidas por absorción y dispersión. Para lidiar con este problema se han realizado algunas propuestas que incluyen nuevas geometrías aperiódicas. Por ejemplo, considerar una serie de guías de onda metálicas con diferentes tamaños del orden de los nanómetros y que estén fuertemente acopladas [46]. La atenuación en esta estructura es considerablemente menor que en un PLM tanto para ondas propagantes como evanescentes.

En 2006 se propuso [64] y posteriormente se demostró experimentalmente [65, 66] un nuevo tipo de superlentes denominadas superlentes de campo lejano. Estas lentes se basan en introducir una red de difracción en la superficie de salida de una superlente metal-dieléctrico. A diferencia de las superlentes convencionales, además de amplificar las ondas evanescentes las convierten en ondas propagantes en la superficie de salida. Al diseñar este tipo de lentes es crucial dotarlas de una función de transferencia que permita numéricamente reconstruir sin ambigüedades las imágenes sub- λ . Se requiere de un diseño de la función de transferencia complejo y una intensa computación numérica para reconstruir la imagen ya que en estas lentes no se puede recuperar la imagen directamente con una red de difracción. Además, estas superlentes no pueden magnificar la imagen.

Por esta razón su aplicación en los sistemas ópticos convencionales se ve limitada, ya que la imagen ha de tener las mismas dimensiones que el objeto.

En estas mismas fechas también se propuso un nuevo tipo de superlentes que pueden aumentar el tamaño de la imagen: las hiperlentes [67, 68]. Están formadas por capas de lentes cilíndricas metal-dieléctrico y son capaces de producir imágenes sub- λ magnificadas en el campo lejano mediante la conversión de las ondas evanescentes en propagantes [69, 70]. Específicamente, las hiperlentes dispersan radialmente la luz permitiendo transportar casi punto a punto una imagen hasta la superficie de salida. A las primeras propuestas de hiperlentes les siguieron desarrollos experimentales en el rango óptico [22, 71]. Algunos de éstos se muestran en la Figura 1(d). Desde entonces se han propuesto hiperlentes en las que se sustituye la geometría cilíndrica por la esférica [72], matrices cónicas de hilos metálicos [73–76] y otros diseños singulares [77–80].

Más adelante se desarrolló otro nuevo tipo de superlentes basadas en metamateriales, conocidas como metalentes [81–84]. Una metalente se crea mediante la combinación de un metamaterial multicapa y un mecanismo de compensación de fase que enfoca una onda plana en un punto. Una limitación importante de las metalentes que comparten con las hiperlentes es el efecto de las pérdidas que limita la resolución de la lente así como la transmisión de la señal. Es posible corregir el efecto de las pérdidas de varias formas: añadiendo ganancia a los dieléctricos que conforman la superlente [15], diseñando la estructura de bandas con mejores materiales plasmónicos, dopando los ya existentes, o mediante aleaciones [85, 86]. Además, el objeto tiene que estar colocado en el campo cercano de la lente para que las superlentes sean capaces de interactuar con las ondas evanescentes. A todo esto hay que sumarle que los diseños actuales para hiperlentes y metalentes tienen un campo de visión muy limitado debido al tamaño de sistema óptico. Por todo ello el diseño de este tipo de lentes es un campo de estudio donde aún se pueden proponer nuevos diseños que mejoren sus características optogeométricas.

Las superlentes son dispositivos muy prometedores en aplicaciones tales como la microscopía o la litografía óptica a escala nanométrica. Esta última es clave a la hora de reducir el tamaño de los circuitos integrados. El almacenamiento óptico y magnético y los biosensores [87] también pueden beneficiarse de la capacidad de estas lentes, permitiendo escribir o leer información dentro de volúmenes cada vez más pequeños y por tanto aumentando la densidad de almacenamiento y la resolución de las medidas.

Objetivos

Esta tesis se centra en la formación de imágenes superresolventes utilizando NIMs y PLMs. Para ello, en primer lugar se derivará una respuesta impulsional (PSF) 3D con el fin de definir sin ambigüedades el campo difractado por una lente plana en el volumen imagen. Por medio de la transformada de Fourier 3D, se introducirá la función de transferencia generalizada con el fin de entender mejor el poder de resolución de los elementos ópticos de una superlente. Estas herramientas junto con la respuesta dipolar eléctrica se aplicarán para evaluar la resolución de los NIMs con absorción moderada al mismo tiempo que se analiza su capacidad para discriminar objetos con profundidad.

También se explorará la posibilidad de mejorar la resolución en el campo lejano solapando a una lente plana de NIM un material con un índice de refracción alto. Se analizarán desde el punto de vista de la óptica geométrica las aberraciones producidas en este tipo de lentes asimétricas. Estas aberraciones pueden dañar la imagen y reducir el poder de resolución de la superlente. A través de un análisis de aberraciones estándar se optimizará la configuración asimétrica de las superlentes basadas en NIMs.

Gran parte de esta tesis se centra en los PLMs. Se pretende señalar las limitaciones existentes en la formación de imágenes 3D con lentes planas basadas en NIMs además de investigar la reducción significativa en el límite de resolución mediante

la división de las superlentes planas en películas ultrafinas. Así mismo se estudiará cómo afecta esta redistribución de las lentes a la profundidad de campo.

También se explorará un diseño de superlente resultante de unir dos PLMs que difractan la luz de manera opuesta y complementaria. En este dispositivo tanto las ondas propagantes como un ancho de banda significativo de ondas evanescentes se transforman en ondas de Bloch propagantes dentro de cada PLM. La difracción producida en una parte del dispositivo es corregida por la difracción negativa de la otra parte.

Las propiedades ópticas de los PLMs serán también analizadas para el régimen de permitividades efectivas próximas a zero (ENZ), siendo este régimen un concepto derivado de la aproximación de medio efectivo. En este régimen los PLMs pueden canalizar sin difractar la luz emitida por emisores puntuales o producir la doble refracción de la luz para una única polarización. Para este segundo caso se propondrá una variación de la aproximación de medio efectivo y con ella una ley de la refracción generalizada que describa las dos refracciones simultáneamente. También se pretende analizar la distribución de flujo energético en las señales refractadas y la reflejada.

Por otro lado se propondrá un método para deducir la PSF tanto en intensidad como en fase de una superlente formada por un PLM. Para ello se considerará el patrón de intensidad producido por una máscara de metal con aberturas calibradas colocada a la entrada de la superlente y se procesará el patrón de intensidad medido a la salida con una variación del algoritmo de deconvolución ciega.

Aunque las superlentes basadas en PLMs están generalmente diseñadas para controlar la difracción de haces convencionales, su uso no está restringido a éstos. Se pretende demostrar la existencia haces Bessel sub- λ en estructuras multicapa y medios con hilos metálicos. En ambos casos, se estudiará el fenómeno de super-resolución producido por la interacción plasmónica entre la materia y la luz. Los patrones de intensidad producidos en estas nanoestructuras también se analizarán para su uso potencial en la formación de imágenes.

Los haces Airy son también candidatos para transportar información sub- λ a través de nanoestructuras. Para concluir presentaremos un breve tratamiento teórico de este tipo de haces incluyendo el importante papel que desempeña en ellos la fase Gouy.

Metodología

En el Capítulo 2 se han caracterizado las ondas de superficie tanto en NIM como en metales. En todos los casos los cálculos necesarios para representar las gráficas se han realizado con el programa comercial Mathematica 9. También se han definido las funciones matemáticas que se usarán en el Capítulo 4 para caracterizar un dipolo puntual eléctrico.

En el Capítulo 3 se han descrito las curvas de dispersión de medios periódicos NIM-dieléctrico y metal-dieléctrico utilizando la ecuación de Bloch así como la aproximación de medio efectivo. De nuevo los cálculos necesarios para representar las gráficas se han realizado con el programa comercial Mathematica 9. En este mismo Capítulo se ha considerado el caso de la doble refracción con una única polarización. Se han calculado las curvas de isofrecuencia y a partir de ellas los ángulos de refracción del rayo ordinario y el extraordinario, todo ello haciendo uso de las ecuaciones de Bloch y realizando los cálculos con Mathematica 9.

A continuación se ha representado la intensidad del campo magnético de un haz gaussiano incidiendo oblicuamente en un PLM y produciendo la doble refracción. Para ello se ha simulado por el método de los elementos finitos con el software comercial COMSOL 3.5 el campo magnético producido por una onda plana con diferentes ángulos de incidencia en una porción del espacio que abarca una anchura de un periodo del PLM. Los resultados obtenidos se han combinado en MatLAB R2012a para producir la imagen final.

Además se ha evaluado la reflectancia y la transmitancia distribuida entre los haces en el montaje propuesto. Para saber cuánta energía se ha reflejado y transmitido hemos considerado el cociente del flujo del vector de Poynting de las ondas reflejadas y transmitidas respecto a la incidente. No hemos considerado absorción dentro del PLM así que el flujo de energía normal a la superficie de separación aire-PLM es una constante en ambos medios. Hemos considerado las componentes normales del promedio temporal del vector de Poynting incidente, reflejado y transmitido, con polarización P. En las simulaciones numéricas hemos evaluado el campo magnético H_x . Para obtener el campo eléctrico y así poder calcular el vector de Poynting se ha hecho una simple descomposición del campo magnético, $H_x = H_{1x} + H_{2x}$. En particular H_{1x} representa el campo magnético que experimenta refracción positiva y H_{2x} el que experimenta refracción negativa. Se ha calculado la transformada de Fourier del campo total H_x a lo largo de la dirección y ; en el dominio de las frecuencias los campos H_{1x} y H_{2x} están localizados alrededor de diferentes frecuencias k_y lo que finalmente nos permitirá discernir la proporción de energía que corresponde a cada haz.

En el Capítulo 4 se ha definido la PSF 3D así como su transformada de Fourier, la ATF. Estas herramientas y su versión 2D se utilizan exhaustivamente en este capítulo y los siguientes para caracterizar elementos formadores de imágenes. También se ha representado la respuesta de un dipolo puntual eléctrico a través de una superlente utilizando el desarrollo matemático de la Sección 2.3. En todos el capítulo se ha usado Mathematica 9 para las representaciones con la excepción de la Figura 4.14 en donde se ha simulado con COMSOL 3.5 el módulo del campo eléctrico emitido por una fuente lineal y transmitido por una lámina de índice negativo.

En el Capítulo 5 se utilizan las herramientas introducidas en los capítulos anteriores para desarrollar la formación de imágenes en metales. El estudio se realiza por procedimientos estándar y haciendo uso de Mathematica 9 en la mayoría de los casos. Existen tres excepciones: la figura 5.4 donde se ha simulado un medio

periódico en el régimen de canalización haciendo uso de COMSOL 3.5. También se ha simulado con COMSOL 3.5 la Figura 5.8 en donde se combina un medio con refracción negativa y otro con refracción positiva.

En la última Sección Capítulo 5, se la PSF tanto en intensidad como en fase de una superlente formada por un PLM. Para ello se procesa la intensidad a la salida de la superlente con una variación del algoritmo de deconvolución ciega que incluyae las condiciones de simetría del PLM. De esta manera se exigirá la simetría de la PFS así como de su transformada de Fourier, la función de transferencia. La implementación del algoritmo así como las figuras se han realizado con MatLAB R2012a.

En el Capítulo 6 se analizan los haces Bessel plasmónicos. Para su estudio se recurre a Mathematica 9 a excepción de los patrones de intensidad de los haces Bessel en los medios estratificados para los que se ha utilizado COMSOL 3.5. Finalmente se introduce la formulación de los haces Airy y se desarrolla con detalle. De nuevo todas las figuras relacionadas con los haces Airy han sido realizadas con Mathematica 9.

Conclusiones

Con el objetivo de estudiar la formación de imágenes en nanoestructuras plasmónicas se ha analizado el patrón de difracción 3D producido por una fuente puntual sobre una lámina de NIM. Este patrón es la transformada de Fourier 3D de una función a la que llamamos la función de transferencia generalizada. Se observa que la ATF generalizada está compuesta por dos partes diferentes: una de ellas, con forma esférica, contiene la información del campo lejano. La otra, con forma de hiperboloide, se asocia a las componentes evanescentes del campo electromagnético. Se concluye que la resolución sub- λ viene determinada principalmente por la modulación de la ATF generalizada en la parte que se corresponde con el hiperboloide. También se concluye que el aumento de la resolución transversal

dentro del régimen de campo cercano puede producirse a costa de la pérdida de la discriminación en profundidad.

La formación de imágenes con superlentes de NIM asimétricas también se evalúa en la Tesis, centrándonos en las aberraciones primarias asociadas y en los efectos de la reflexión. Ambos son efectos no deseados que provienen del desajuste de las impedancias en las interfases. Para corregirlos se propone diseñar una superlente con un revestimiento reflejante que reduzca al mínimo la reflexión de la luz. Así mismo, se concluye que para evitar aberraciones esféricas basta con colocar el plano objeto a una distancia concreta de la interfase de entrada de la superlente. Especialmente para superlentes con anchos $\text{sub-}\lambda$ la contribución de las ondas evanescentes es significativa. Por tanto, para conseguir una superlente con una resolución óptima es necesario buscar un acuerdo entre la contribución de las aberraciones de orden superior y la contribución de las ondas evanescentes.

Volviendo a centrarnos en las superlentes simétricas, se sabe que su resolución puede mejorarse dividiendo el NIM en múltiples películas. A cambio se reduce la profundidad de campo y la capacidad de observar imágenes fuera del plano. Por tanto, a la hora de diseñar una superlente multicapa conviene alcanzar un equilibrio entre el poder de resolución requerido y la capacidad de discriminación en volumen que se desea.

En esta Tesis, además de las superlentes fabricadas con NIMs también se estudian las superlentes metálicas. En su superficie pueden excitarse plasmones polaritones. Esto permite acceder a un enorme espacio de índices de refracción efectivos que pueden ajustarse fácilmente variando los materiales, las dimensiones o la geometría. En concreto, podemos diseñar un medio metal-dieléctrico para que se comporte como un medio uniaxial con permitividad próxima a cero. En el régimen de canalización estos medios permiten la propagación de altas frecuencias espaciales. Su interacción con los modos evanescentes de la fuente permite la formación de imágenes $\text{sub-}\lambda$ a lo largo del eje óptico del metamaterial. Finalmente

hemos desarrollado un método de ajuste simple que incluye las frecuencias espaciales altas en las relaciones de dispersión, las cuales no aparecen en el modelo estándar de la aproximación de medio efectivo.

También proponemos una ley de refracción generalizada que describe la doble refracción de las ondas polarizadas-TM. El acoplamiento de los modos de la red y los efectos no locales son responsables de este efecto. Se ha llevado a cabo un análisis sobre la distribución de energía entre estos haces refractados en función del ángulo de incidencia en la PLM.

Fuera del régimen de canalización también es posible producir imágenes sub- λ . Para ello proponemos un dispositivo formado por dos PLMs altamente anisotrópicos. El primero convierte las ondas evanescentes en ondas de Bloch. La dispersión producida dentro de ese medio es compensada por la refracción negativa del medio adyacente. Su dispersión tiene una curvatura opuesta a la del primer medio. El medio con refracción negativa recoge un amplio espectro de ondas de Bloch y posteriormente las enfoca adecuadamente en el plano de salida del dispositivo.

Gran parte de los resultados presentados en esta Tesis se sustentan en el análisis de la PSF. Aunque esta función es útil en la formación de imágenes, es técnicamente complicada de medir. Para lidiar con este problema se propone una versión del algoritmo de deconvolución ciega que incluye ciertas condiciones impuestas por la física del sistema. Éste permite recuperar la PSF mediante el patrón de intensidad medido en la interfase de salida de la superlente. Mientras que en los algoritmos de deconvolución ciega estándar sólo se recupera el módulo de la PSF, la versión introducida en esta Tesis también es capaz de recuperar la fase.

Además de formar imágenes sub- λ canalizando ondas evanescentes, los PLMs también permiten la propagación de haces localizados adifraccionales con una anchura de tamaño sub- λ . Específicamente nos referimos a haces Bessel propagándose en medios dieléctrico fuera del régimen de canalización. Para producir este fenómeno hace falta excitar en una superlente un número adecuado de SPPs de alto orden y que estén en fase. Los efectos disipativos de los metales conducen

a un régimen adifraccional limitado por la longitud de atenuación de la energía. Sin embargo, la localización del haz sobre el eje se mantiene a lo largo de un intervalo que es mayor que la longitud de atenuación de la energía en más de un orden de magnitud. La posibilidad de excitar múltiples haces Bessel en estas nanoestructuras abre el camino para la formación de imágenes superresolventes.

Por último, consideramos otro tipo de haces adifraccionales: los haces Airy. Éstos haces conservan su perfil pero siguen una trayectoria parabólica en el régimen paraxial. En particular, hemos analizado la fase de Gouy que se puede expresar en este tipo de haces con una integral de línea. Las ecuaciones que describen las líneas de corriente, el vector de Poynting y la variación espacial de la velocidad de fase en estos haces proporcionan un punto de partida para explorar el flujo de energía electromagnética. Este análisis general se puede aplicar tanto a haces Airy plasmónicos como a haces propagándose por el espacio libre.

List of Publications

This dissertation is based on the following journal articles and conference proceedings.

Journal Articles

- [I] D. Pastor, T. Stefaniuk, P. Wróbel, C.J. Zapata-Rodríguez, and R. Kotyński. Determination of the point spread function of layered metamaterials assisted with the blind deconvolution algorithm. *Opt. Quant. Electron.*, 47(1):17, 2014.
- [II] C.J. Zapata-Rodríguez, D. Pastor, L.E. Martínez, M.T. Caballero, and J.J. Miret. Single-polarization double refraction in plasmonic crystals: considerations on energy flow. *Appl. Mech. Mater.*, 472:729, 2014.
- [III] C.J. Zapata-Rodríguez, D. Pastor, J.J. Miret, and S. Vuković. Uniaxial epsilon-near-zero metamaterials: from superlensing to double refraction. *J. Nanophoton.*, 8(1):083895, 2014.
- [IV] C.J. Zapata-Rodríguez, D. Pastor, L.E. Martínez, and J.J. Miret. Left-handed metamaterial coatings for subwavelength-resolution imaging. *J. Opt. Soc. Am. A*, 29(9):1992, 2012.

xvi List of Publications

- [V] C.J. Zapata-Rodríguez, D. Pastor, M.T. Caballero, and J.J. Miret. Diffraction-managed superlensing using plasmonic lattices. *Opt. Commun.*, 285(16): 3358, 2012.
- [VI] C.J. Zapata-Rodríguez, D. Pastor, and J.J. Miret. Considerations on the electromagnetic flow in Airy beams based on the Gouy phase. *Opt. Express*, 20(21):23553, 2012.
- [VII] C.J. Zapata-Rodríguez, D. Pastor, V. Camps, M.T. Caballero, and J.J. Miret. Three-dimensional point spread function of multilayered flat lenses and its application to extreme subwavelength resolution. *J. Nanophoton.*, 5(1): 051807, 2011.
- [VIII] J.J. Miret, D. Pastor, and C.J. Zapata-Rodríguez. Subwavelength surface waves with zero diffraction. *J. Nanophoton.*, 5(1):051801, 2011.
- [IX] C.J. Zapata-Rodríguez, S. Vuković, M.R. Belić, D. Pastor, and J.J. Miret. Nondiffracting Bessel plasmons. *Opt. Express*, 19(20):19572, 2011.
- [X] C.J. Zapata-Rodríguez, D. Pastor, and J.J. Miret. Three-dimensional point spread function and generalized amplitude transfer function of near-field flat lenses. *Appl. Opt.*, 49(30):5870, 2010.

Conference Proceedings

- [I] D. Pastor, T. Stefaniuk, P. Wróbel, C.J. Zapata-Rodríguez, and R. Kotyński. Determination of the point spread function of layered metamaterials assisted with the blind deconvolution algorithm. In *Proc. IP*, page 146, Warsaw, 2013.
- [II] C.J. Zapata-Rodríguez, D. Pastor, M.T. Caballero, L.E. Martínez, and J.J. Miret. Plasmon-driven Bessel beams. In *Proc. FiO/LS*, number FW1A-1, Rochester, 2012.

- [III] C.J. Zapata-Rodríguez, D. Pastor, M.T. Caballero, and J.J. Miret. Plasmonic stratified devices for superlensing in the self-focusing regime. In *Proc. FiO/LS*, number FTu3A-64, Rochester, 2012.
- [IV] C.J. Zapata-Rodríguez, D. Pastor, M.T. Caballero, and J.J. Miret. Diffraction-managed superlensing using metallodielectric heterostructures. In *Proc. SPIE*, volume 8423, page 84230U, 2012.
- [V] J.J. Miret, C.J. Zapata-Rodríguez, S. Vuković, and D. Pastor. Subwavelength diffraction-free beams in metallic wire media. In *Proc. SPIE*, volume 8423, page 84230V, 2012.
- [VI] C.J. Zapata-Rodríguez, D. Pastor, P. Cencillo, M. Avellaneda, S. Vuković, and J.J. Miret. Dual hyperbolic-elliptic media. In *Proc. SPIE*, volume 8423, page 84231Z, 2012.
- [VII] C.J. Zapata-Rodríguez, D. Pastor, J.J. Miret, M.T. Caballero, and V. Camps. Generation of nondiffracting subwavelength-beams in finite metal-dielectric structures. In *Proc. SPIE*, volume 8470, page 80700H, 2011.
- [VIII] C.J. Zapata-Rodríguez, D. Pastor, and J.J. Miret. Flat photonic lattices for near-field imaging with enhanced depth of field. In *Proc. SPIE*, volume 8470, page 807012, 2011.
- [IX] C.J. Zapata-Rodríguez, D. Pastor, and J.J. Miret. Metamaterial coatings for subwavelength-resolution imaging. In *Proc. SPIE*, volume 8470, page 807014, 2011.
- [X] C.J. Zapata-Rodríguez, S. Vuković, Z. Jakšić, D. Pastor, and J.J. Miret. Plasmon-driven nondiffracting surface beaming. In *Proc. ICTON*, DOI: 10.1109/ICTON.2011.5971069, 2011.

Abbreviations

AiB	Airy Beam
BB	Bessel Beam
EM	Electro Magnetic
EMA	Effective Medium Approach
ENZ	Epsilon Near Zero
DOF	Depth Of Field
FEM	Finite Element Method
FK	Fresnel-Kirchhoff
FWHM	Full Width at Half Maximum
GP	Gouy Phase
MD	Metallo Dielectric
NIM	Negative Index Material
PLM	Periodic Layered Media
PSI	Poynting vector StreamLines
TE	Tansverse Electric
TM	Tansverse Magnetic
SA	Spherical Aberration
SPP	Surface Plasmon Polariton

xx Abbreviations

SRR Splitting **R**ing **R**esonators

SW Surface **W**aves

Contents

Resumen	i
List of Publications	xv
Abbreviations	xviii
1 Introduction	1
1.1 Motivation	1
1.2 Scope of this Thesis	8
2 Electromagnetic Waves in Dielectrics, Metals and NIMs	11
2.1 Negative- ϵ and Negative- μ Materials	12
2.1.1 Material Dispersion	15
2.1.2 Plane Waves in Isotropic NIMs	18
2.2 Surface Waves	20
2.2.1 Surface Waves in a Dielectric-NIM Interface	21
2.2.2 Surface Waves in Metals: SPPs	26
2.3 Point Dipole Sources	30
3 1D Metamaterials	33
3.1 Bloch Modes	34
3.2 Metal-Dielectric Periodic Layered Media	37
3.2.1 Effects of Losses in PLMs	40
3.3 Dielectric-NIM Stratified Media	43
3.3.1 Dielectric-Lossy NIM Periodic Media	45
3.4 Effective Media	46

3.4.1	Hyperbolic Metamaterials	51
3.5	Dual Hyperbolic-Elliptic Media	53
3.6	Double Refraction Induced by Nonlocal Effects	55
4	Image Formation Using NIMs	59
4.1	Geometric Optics Approach	60
4.2	Electromagnetic Formulation	61
4.3	3D Point Spread Function	65
4.3.1	Far-Field Term and Near-Field Term	67
4.3.2	Generalized Amplitude Transfer Function	70
4.3.3	Out-of-Focus Response	72
4.3.4	Imaging Electric Point Dipoles	76
4.4	Asymmetric Arrangements and Aberration Correction	77
4.5	Imaging with Periodic Structures	90
5	Image Formation Using Metals	97
5.1	Monolayer metallic superlens	98
5.2	Image-Forming Multilayered Stacks	101
5.2.1	Canalization	101
5.2.2	Diffraction-Management	107
5.3	PSF Recovery Assisted by the Blind Deconvolution Algorithm	115
6	Diffraction-Free Localized Wave fields	121
6.1	Introduction to Bessel Beams	122
6.1.1	Basic Bessel-Beam Formulation in Free Space	124
6.2	Plasmonic Bessel Beams	126
6.2.1	Plasmonic Bessel Beams in Stratified Media	127
6.2.2	Plasmonic Bessel Beams in Wire Media	134
6.3	Introduction to Airy Beams	142
6.3.1	Plasmonic Airy Beams	143
6.3.2	Finite-Energy Airy Beams in the Paraxial Approximation	145
6.4	The Gouy Phase in Airy Beams	149
7	Conclusions	155
7.1	Future lines	158

A Propagation Matrix Method	161
------------------------------------	------------

Bibliography	167
---------------------	------------

Chapter 1

Introduction

1.1 Motivation

In 1873, Ernst Abbe concluded that the resolving ability of an optical imaging system is limited to half the working wavelength due to the diffraction of light [1]. This fundamental limit, called the diffraction limit is attributed to the finite wavelength of electromagnetic waves. In any optical system made of materials found in the nature the spatial details of the object smaller than a wavelength, carried by the evanescent waves, are lost due to the strong attenuation these waves experience when traveling from the object to the image.

In 1968, Veselago [2] showed that a medium with both negative permittivity and permeability, called negative index material (NIM), exhibited a number of uncommon phenomena, such as reverse Doppler shift, Čerenkov radiation and the reverse equivalents of Snell's law. The latter phenomena let a slab made of such a material to act as a focusing lens, producing a real image of a source placed in

front of the slab. It was not until 2000 when Pendry suggested another extraordinary property of the NIM slabs: they are not restricted by the diffraction limit. They can produce perfect images if they are completely lossless and impedance matched to the surrounding medium [3, 4]. The NIM lens achieves perfect imaging by focusing propagating waves as well as supporting growing evanescent waves employing surface polariton resonances excited in the near field. Evanescent waves restore at the image plane the decaying evanescent waves emanating from the source. We will refer to a piece of matter capable of sub-diffraction limit focusing as a superlens.

The ability to overcome the diffraction limit introduced in Pendry's seminar paper was questioned both theoretically [5] and in numerical simulations [6]. They discuss the fact that near-field modes amplification makes fields in the superlens image plane non-integrable. This problem must be avoided by considering losses in the NIM. It is noteworthy that realistic NIMs always have a significant amount of losses that cannot be ignored in the calculations. Consequently, the large amplification of the evanescent spatial frequencies causes large amounts of dissipation, which does prevent the complete restoration of these wave fields.

Not only losses but a variety of parameters determine the evanescent spatial bandwidth transmitted and consequently the resolution [7]. For instance, it is possible to increase the resolution of the slab lens by choosing an asymmetric configuration with a large dielectric constant on the side of the image [8]. It has also been shown that slight deviations from the impedance matched conditions can lead to the resonant excitation of slab plasmons which can also help to increase the resolution [8]. In addition, it is also possible to increase the resolution by restructuring the lens [9]. However the introduction of gain materials is believed to be the most efficient approach but also very challenging [4, 10–18].

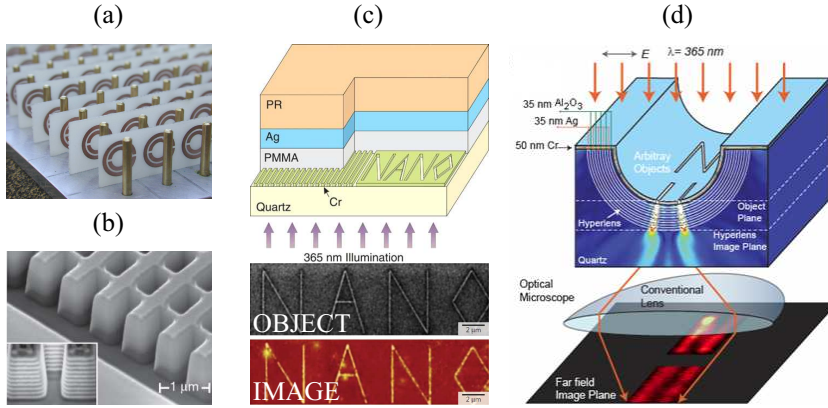


FIGURE 1.1: (a) First experimental realization of a NIM. A split ring structure etched into copper circuit board plus copper wires to give negative μ and negative ϵ . Reprinted from [19]. (b) SEM image of the 21-layer fishnet structure. Reprinted from [20]. (c) Optical superlensing experiment with a silver layer as a lens. Reprinted from [21]. (d) Schematic of an hyperlens and numerical simulation of imaging of sub-diffraction-limited objects. Reprinted from [22].

The first experimental demonstration of a NIM at microwave frequencies was performed by Smith et al. [23, 24], whose arrangement can be seen in Fig. 1.1(a). They demonstrated negative refraction at microwave frequencies using a NIM made of an array of wavelength scale unit cells. This unit cell consists of a split-ring resonator and a wire. Improved experimental results verifying negative refraction have been reported using a refined version of the same split-ring resonators and wires medium [25, 26]. This kind of medium is only efficient for the fabrication of superlenses at microwaves and infrared frequencies due to the strong absorption at higher frequencies. A fishnet structure, i.e., a perforated metal-dielectric-metal sandwich as shown in Fig. 1.1(b) can substitute the split-ring-resonator arrangement [20, 28, 29], which fails to provide negative μ above infrared frequencies [27].

All the NIMs that have been developed until today are obtained by putting together two structured materials that show separately a negative dielectric permittivity and

negative magnetic permeability. The majority of the metamaterial studies focused on achieving the desired electromagnetic response at a single frequency band, dual-band [30, 31], multi-band [32] and even tunable [33]. All-angle negative refraction in two-dimensions was then demonstrated by direct observation of plane-wave refraction through prism-shaped segments of such assemblies [34, 35].

In the near field, the electric and magnetic responses of materials are decoupled. Therefore, for transverse magnetic waves, only the negative permittivity is request for subwavelength image creation [3]. Noble metals such as silver are natural candidates for superlensing at optical ranges. Negative permittivity is easily attainable with them. At optical frequencies, $|\epsilon|$ in metals can be comparable to the dielectric permittivity of a host material, allowing the excitation of a surface plasmon-polariton (SPP) resonance on the boundaries between metal and dielectric. The subwavelength details of the source are transmitted through the system because they couple to the SPP [3, 8]. An experimental realization of this kind of superlens can be seen in Fang et al. experimental setup shown in Fig. 1.1(c). In 2003, a few optical experiments demonstrated that evanescent waves are indeed significantly enhanced across a silver slab [36, 37]. The experiments found that the evanescent enhancement factor increases exponentially until a particular film thickness related with the wavelength, then the material loss becomes more prominent. Consequently it is possible to reduce absorptive effects introducing active materials [11] or exfoliating the original thick slab into ultrathin layers and distributing it around between the source and image planes producing an array of elementary superlenses. The incident evanescent waves excite plasmon resonances which transfer the inhomogeneous waves via plasmon-mediated tunneling mechanism [38–41], often referred to as resonant plasmon tunneling [42], amplifying itself to smaller extents in each layer, reducing the absorption in the metals,

and consequently enhancing the output image resolution [4, 43, 44].

During studies of imaging in silver-air layered media it was noted that they may be understood as a particular case of a metal-dielectric periodic layered media (PLM). These media can be engineered to provide a promising platform for the study of surface plasmons related phenomena, such as negative refraction [45], and subwavelength focusing [46–48]. In addition subwavelength imaging in this kind of structures may happen due to a principle other than negative refraction and amplification of evanescent waves. The evidence of this was reported by numerous authors [49–52]. A slab of PLM may be modeled to display a flat isofrequency contour that makes it behave as a waveguide, with little or no diffraction taking place, in a scheme that helps the formation of a super-resolved image on the exit surface [4]. This regime was called canalization [52].

The problem of extending the use of structures that contain metallic components to the visible range has since been addressed in several publications [39, 53–63]. The major issues under discussion are the inherently large absorption and scattering losses which are not easily overcome. Some original non-periodic proposals came out taking into consideration new geometries to face this challenge. For instance Verslegers considered an aperiodic array of coupled metallic nanometric waveguides with different sizes [46]. Attenuation in this metamaterial during propagation is considerably lower than in the PLMs.

In 2006, a new kind of superlens referred to as a far-field superlens was proposed [65, 66] and subsequently tested [64]. The far-field superlens is made of a silver superlens with additional nanoscale corrugations on its top surface. This lens not only enhances the evanescent waves but also converts them into propagating waves. A proper transfer function of the far-field superlens is crucial, because

it ensures the 'uniqueness' required for the reconstruction process to form sub-diffraction-limit images. The main limitation of the far field superlens is that requires a subtle transfer function design and an intense numerical image reconstruction computing, as the image cannot be directly formed by a grating in this application.

The aforementioned superlenses cannot provide magnification to the image, which is one of the fundamental properties of conventional optical lenses. This drawback limits their applications in conventional optical systems, as the image would have the same dimensions as the object; the image could not be directly resolved by a conventional optical system if the object itself is already irresolvable by the same system. These superlenses have to rely on non-optical imaging systems like atomic force microscopy, focused ion beam, scanning electron microscopy, scanning probe microscopy or nontrivial numerical image reconstructions to generate images beyond the diffraction limit.

In 2006 a breakthrough in superlenses occurred when hyperlenses were proposed and theoretically studied [67, 68]. They are layered metal-dielectric cylindrical lenses producing magnified sub-diffraction-limited images in the far field by converting the evanescent waves into a propagating waves [69]. Specifically, hyperlenses provides a nearly straight dispersion in cylindrical coordinates which results in point-to-point mapping from the center surface to the outer one. While this yields sub-diffraction resolution, it implies that the hyperlens is incapable of focusing plane waves [70]. Different experimental proposals following the concept of hyperlensing were subsequently reported at the optic wavelengths [22, 71], as can be seen in Fig. 1.1(d). Other configurations rather than cylindrical, such as spherical [72], tapered metallic wire arrays [73–76] or uniquely designed material dispersions [77–80] have been proposed since then.

More recently, other metamaterial-based focusers, known as metalenses, have been developed with super-resolving power [81–84]. A metalens is created by combining a metamaterial slab and a phase compensation mechanism to bring a plane wave to a focus. The hyperlens and the metalens thus share the same material requirement, with practical realizations including multilayers [22, 88]. In addition, a coupler is needed to induce a phase compensation mechanism.

A major limitation for the hyperlenses and metalenses is the material losses that set bounds to the lens resolution and signal transmission. To overcome the effect of losses several approaches may provide solutions, such as addition of a gain medium in dielectrics [15], searching for better plasmonic materials among existing elements, band structure engineering, materials doping or alloying [85, 86]. In addition, the object has to be placed in the near field of the lens to make use of the evanescent waves that normally decay away from the object. New imaging schemes may be needed to solve this issue. Besides, current designs for both hyperlenses and metalenses have very limited field of view due to the limited physical size of the lens. Better designs may solve the problem but it remains wide open to solutions.

Both superlenses and hyperlenses are very promising in applications such as extending the optical microscope into the nanometre scale; reducing ultra-small scales optical lithography which is the key to scaling down integrated circuits. Optic and magnetic data storage and biosensing [87] may also benefit from the ability to write or read information within ultra-small volume, thereby increasing storage densities or sensing resolution.

1.2 Scope of this Thesis

In this Thesis we focus on the superlensing phenomena using either NIM or PLM. More specifically, we deeply examine the image formation process. First, we derive a nonsingular, polarization-dependent, 3D impulse response that provides unambiguously the wave field scattered by a layered lens and distributed in its image volume. By means of a 3D Fourier transform, we introduce the generalized amplitude transfer function in order to gain a deep insight into the resolution power of the optical element. With these tools and the point dipole spread function we show that NIMs with moderate absorption are appropriate for subwavelength resolution keeping a limited degree of depth discrimination. We also found out-of-focus imaging limited by the polariton resonances in the subwavelength image formation process.

By considering flat NIM lenses we report on a procedure to improve the resolution of far-field imaging using a neighbouring high-index medium coated with a NIM. Based on negative refraction, geometrical aberrations are considered in detail since they may cause a great impact in this sort of diffraction-limited imaging by reducing its resolution power. Standard aberration analysis is employed to refine the asymmetric configuration of metamaterial superlenses.

A great part of this Thesis focuses on layered media. We point out the existing limitations of NIM flat lenses in the formation of 3D images. In addition we investigated the significant reduction of the limit of resolution by exfoliating NIM flat lenses into ultrathin layers. This super-resolving effect has its counterpart in the reduction of the depth of field.

Regarding PLMs, we show a procedure to manage the subwavelength diffracted wave fields inside multilayered plasmonic devices to achieve ultra-resolving lensing. Both homogeneous waves and a broad band of evanescent waves are transformed into propagating Bloch modes by means of a metal-dielectric superlattice. Beam spreading is subsequently compensated by means of negative refraction.

Optical properties of nanostructured PLMs are also studied under the epsilon-near-zero regime, a concept derived from the effective-medium approach. The PLM may exhibit either superlensing driven by broadband canalization from point emitters or single-polarization double refraction, and conventional positive as well as negative, even at subwavelength regimes. For the latter case, we formulated a modified effective medium approximation (EMA), and subsequently a generalized refraction law, that describes both refractive behaviors concurrently. We analyze the energy-flow concerning both positive and negative refraction as well as the reflectance.

While the most conventional way to achieve superresolution is by diffraction-managed nanostructures, new avenues arise by direct manipulation of the wave fields. We will demonstrate the existence of subwavelength nondiffracting Bessel beams propagating in both layered and wire media. In both cases the superresolution phenomena provided by the plasmonic interaction between matter and light is studied. Intensity patterns produced in these nanostructures are also analyzed with a view to the imaging formation.

Airy beams are also candidates to transport subwavelength information through nanostructures. We introduce a brief theoretical treatment of this sort of beams including the important role of the Gouy phase. Finally, Airy beams propagating

10 Chapter 1 Introduction

inside plasmonic nanostructures are developed in the same way as we did previously using Bessel beams.

Chapter 2

Electromagnetic Waves in Dielectrics, Metals and NIMs

Before presenting the main results of this Thesis, some fundamental concepts have to be introduced. In Chapter 2 we review the basic electromagnetism that will be applied in the following chapters. For instance NIMs also known as double negative materials are briefly characterized. Additionally plane wave propagation inside a NIM is reviewed. This background is useful to describe surface waves generally, and particularly in the study of surface polaritons. Finally, the mathematical tools to easily describe the fields emitted by a point dipole source are outlined for the free space, and their propagation through a slab of any material. In Chapter 4 the dipole source analysis will be applied to the image formation with NIM slabs.

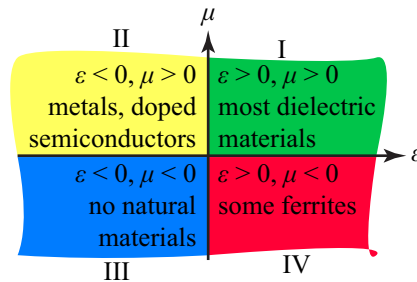


FIGURE 2.1: Material parameter space characterized by electric permittivity and magnetic permeability.

2.1 Negative- ϵ and Negative- μ Materials

Electric permittivity, ϵ , and magnetic permeability, μ , are two fundamental parameters in electromagnetism. They characterize the electromagnetic (EM) properties of a medium. Physically, permittivity (permeability) describes how an electric (magnetic) field affects, and is affected by a medium. That is determined by the ability of a material to be polarized in response to the electric (magnetic) field.

A common way to represent the different kind of isotropic materials and their EM properties is by representing it in the *material parameter space* as shown in Fig. 2.1. Region I in the upper-right quadrant covers materials with simultaneously positive permittivity and permeability, which include most dielectric materials. Quadrant II embraces metals, ferroelectric materials, and doped semiconductors that could exhibit negative permittivity at certain frequencies (below the plasma frequency). Despite the fact that quadrant III materials with simultaneous permittivity and permeability do not exist in nature, it can be manufactured with the existing technology. Region IV is comprised of some ferrite materials with negative permeability, the magnetic responses of which, however, quickly fade away above microwave frequencies.

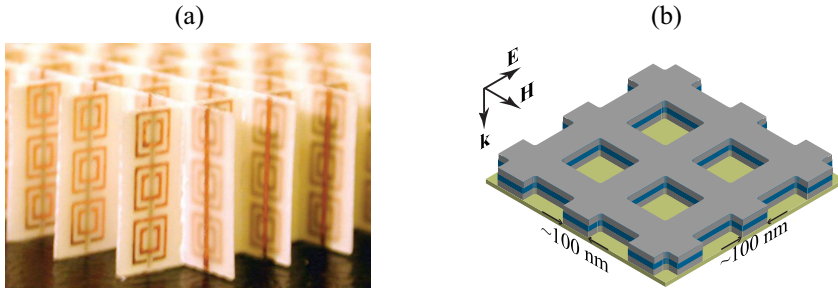


FIGURE 2.2: (a) NIMs working at microwave frequencies consisting of copper SRRs and wires deposited lithographically on standard circuit boards. Reprinted from [24]. (b) Fishnet structure in which two layers of metal meshes (gray) are separated by a dielectric layer (cyan).

Metamaterials from region III are nanocomposites that exhibit exceptional properties not readily observed in nature. These properties arise from response functions that are not observed in the constituent materials and result from the inclusion of artificially fabricated, extrinsic, low dimensional inhomogeneities. Veselago medium is probably the most famous class of metamaterial in the present wave of complex EM media. In his study of 1960's [2], Viktor G. Veselago discussed the peculiar behavior of EM waves in connection with materials that have simultaneously negative permittivity and negative permeability. These phenomena (negative refraction, reversed Doppler shift, inverse Cherenkov radiation, etc.) were unexpected. Now, after 40 years, ways have been developed to create resonating structures which, when embedded in a support matrix, make the macroscopic response negative in both ϵ and μ , although only within a narrowband [23]. The possibility of creating optical negative index metamaterials using nanostructured metal–dielectric composites has triggered intense basic and applied research over the last decade [3, 89–93].

Simultaneous negative ϵ and μ can be reached with different designs. The first experimental realization was performed by Smith and colleagues in the microwave

domain [23, 24]. They used a periodical structure of splitting ring resonators (SRRs) like the one from Fig 2.2(a). The elements size and spacing are much smaller than the wavelength of EM waves in the same frequency window. Such a collection of inhomogeneous objects can be characterized by an equivalent homogeneous material with effective relative permittivity, and permeability at the macroscopic level. A negative effective refractive index, was achieved by overlapping these materials.

Ever since then, considerable interest has been sparked in the field of metamaterials. Within several years, magnetic metamaterials, and consequently NIMs have been advanced from microwave frequencies to the visible region [92, 94, 95]. Approaches moving to shorter wavelengths were initially based on concepts from the microwave regime (such as SRR) with scaled down unit cell sizes. The main idea was that the magnetic resonance frequency of the SRR is inversely proportional to its size. Using a single SRRs, this approach works up to about 200 THz [96–98]. However, this scaling breaks down for higher frequencies in a single SRR case because at frequencies smaller than about 200 THz, the metal behavior starts to strongly deviate from an ideal conductor. The non-ideal metal behavior leads to a modified scaling law where the frequency approaches a constant and becomes independent of the SRR size [98]. This scaling limit combined with the fabrication difficulties of making nanometer-scale SRRs along with metal wires led to the development of alternative designs that are more suitable for the THz and optical regimes. Nonetheless, feature sizes for metamaterials operating in the infrared or visible range may be smaller than the resolution of state-of-the-art photolithography (due to the diffraction limit), thus requiring nanofabrication processes with 100- or sub-100-nm resolution.

The most successful optical NIMs so far are the fishnet structures [90, 99, 100], outlined in Fig 2.2(b), which consists of two layers of metal meshes separated by a dielectric spacer layer. The paired stripes oriented parallel to the electric field provide negative ϵ , while the other pairs of stripes parallel to the magnetic field offer negative μ . Since the thickness of the spacing dielectric is easily controlled, the simple design of the fishnet structure significantly eases the fabrication burden, compared to the conventional approach of combing SRRs and metallic wires. Another key benefit of the fishnet structures is that the EM waves impinge normal to the fishnet sample surface to produce the negative refractive index while the SRR configurations works better with oblique incidence.

2.1.1 Material Dispersion

Dispersion properties of isotropic materials may be properly characterize in the classical electromagnetism formulation by the *Lorentz model*. In this model the permittivity and permeability as functions of the frequency, ω , follow very similar formulas due to the symmetry of EM waves. It may be derived from the oscillation equation of electric charges or fictitious magnetic charges driven by an external EM wave [101]. If there are many oscillating charges of different resonant frequencies, the dielectric and magnetic functions for a multiple-oscillator model are

$$\epsilon(\omega) = 1 - \sum_j \frac{\omega_{pj}^2}{\omega^2 - \omega_{0j}^2 + i\gamma_j\omega}, \quad (2.1a)$$

$$\mu(\omega) = 1 - \sum_j \frac{\omega_{pmj}^2}{\omega^2 - \omega_{0mj}^2 + i\gamma_{mj}\omega}, \quad (2.1b)$$

respectively. From now on, we will consider the most simple situation in which only one oscillation is considered so the index j disappears. This approach is valid provided that the neglected resonances are far from the working spectral band. Taking this into consideration, ω_p (ω_{pm}) is the plasma frequency, ω_0 (ω_{0m}) is the resonant frequency and γ (γ_m) is the damping factor for the permittivity (permeability). The subscript m denotes the magnetic response. Substituting the proper values into Eqs. (2.1), we can characterize material properties over a wide frequency range from microwave to visible. In the optical regime, $\mu = 1$ holds for most of the materials that we can find in the nature. Natural materials that exhibit electric responses are far more common. This is particularly true when we move beyond the gigahertz region, where the magnetic response of most materials begins to tail off.

For noble metals, ω_p is at visible or UV frequency. In addition, ω_0 vanishes under the free electron approximation. Under these assumptions Eq. (2.1a) simplifies to, $\varepsilon(\omega) = 1 - [\omega_p^2/(\omega^2 + i\gamma\omega)]$, the expression for ε in the *Drude model* of metals [102]. This formulation implies that the permittivity of metals is always negative below the plasma frequency. In addition, they do not have magnetic activity ($\mu = 1$). Metals are often optically described by their refractive index, n , defined as $n^2 \equiv \varepsilon$. For values of the damping frequency different from zero the refraction index is complex, $n = n' + in''$, due to the complex values of the permittivity, $\varepsilon = \varepsilon' + i\varepsilon''$. Tabulated datasets for n' , and the extinction coefficient, n'' , are most often described from Johnson and Christy in Ref. [103] and Palik Handbook of Optical Constants [104] in the literature. Optical constants of silver in Johnson and Christy were determined through measurements of reflection and transmission at normal incidence and transmission of p -polarized light at 60 deg.

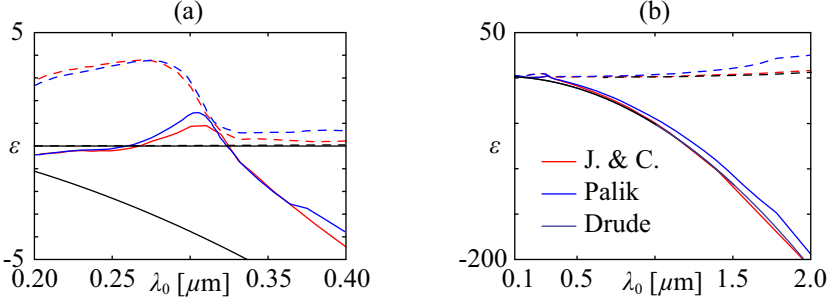


FIGURE 2.3: $\epsilon(\omega)$ tabulated values of Ag interpolated from Johnson and Christy (red), Palik (blue), Drude model (black). The permittivity is plotted (a) in part of the ultraviolet spectrum and (b) for a broad range of wavelengths. The continuous lines correspond to the real part of ϵ . Dashed lines fit the imaginary part of ϵ .

In contrast, the optical constants compiled by Palik were obtained via reflectance measurements using synchrotron radiation and polarimetric measurements.

One of the most common metals for the design of plasmonic nanostructures in the optical range is silver. Lower losses compared to other metals make it especially attractive in this frequency range. Figure 2.3 shows the dielectric function of Ag as derived from the data of both Johnson and Christy, and Palik. The Drude model with $\omega_p = 13.7$ rad/fs and $\gamma = 274 \times 10^{-4}$ rad/fs is also included [105]. Note that $\gamma \ll \omega$ so that Eq. (2.1a) can be approached by $\epsilon(\omega) \approx 1 - (\omega_p/\omega)^2$.

Silver permittivity in the vicinity of the plasma frequency is depicted in Fig. 2.3(a). At these shorter wavelengths there is a region of anomalous dispersion where ϵ' increases with the wavelength, λ_0 . The Drude model itself is inaccurate in this range in part cause by the contribution of the bound electrons. Despite the transparency of metals within this regime, ϵ'' may be substantially higher than the real component for such frequencies. For most visible and infrared wavelengths we can see in Fig. 2.3(b) that the metal exhibits a large, negative, real component of the permittivity while the imaginary part remains small compared with ϵ' . Under

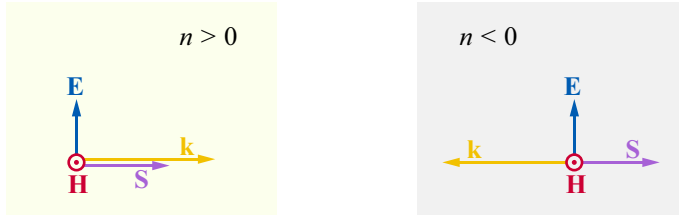


FIGURE 2.4: Schematic representation of a plane wave propagating in a dielectric (left) and a NIM (right). Note that in the NIM, the wave vector \mathbf{k} and Poynting vector \mathbf{S} are antiparallel.

these circumstances the EM field hardly penetrates inside the metal and the energy losses decrease. In Chapter 3 we will see that metals are suitable for the design of 1D plasmonic metamaterials.

2.1.2 Plane Waves in Isotropic NIMs

Fields in NIMs have a unique behavior that can be inspected through the propagation of a plane wave. Let us consider a monochromatic plane wave, $\mathbf{E} = \mathbf{E}_0 e^{i(\mathbf{k}\cdot\mathbf{r} - \omega t)}$, propagating in an isotropic, homogeneous medium in the absence of charges and currents. Considering the constitutive relations $\mathbf{D} = \epsilon\epsilon_0\mathbf{E}$ and $\mathbf{B} = \mu\mu_0\mathbf{H}$, Maxwell equations became

$$\mathbf{k} \times \mathbf{E} = \mu\mu_0\omega\mathbf{H}, \quad (2.2a)$$

$$\mathbf{k} \times \mathbf{H} = -\epsilon\epsilon_0\omega\mathbf{E}. \quad (2.2b)$$

It can be readily seen that the wave vector, \mathbf{k} , the electric field, \mathbf{E} , and the magnetic field, \mathbf{H} , form a right-handed triplet of vectors, as a plane wave propagates in dielectric materials with $\epsilon > 0$ and $\mu > 0$. In contrast, these vectors form a left-handed triplet in materials with $\epsilon < 0$ and $\mu < 0$. Moreover, the Poynting vector, defined as $\mathbf{S} = \mathbf{E} \times \mathbf{H}$, is antiparallel to the wave vector \mathbf{k} in such materials. As a

consequence there is a backward propagation in the phase velocity, v_p . Fields in dielectric and NIMs are both simultaneously plotted in Fig. 2.4. Refractive index in NIMs must take a negative sign as a consequence of the fields orientation [2].

It must be noted that dispersionless material parameters $\epsilon < 0$ or $\mu < 0$ cannot exist. Negative ϵ or μ for static fields would, for example, imply that its energy density,

$$W = \frac{1}{2}(\epsilon_0\epsilon\mathbf{E}^2 + \mu_0\mu\mathbf{H}^2) < 0 \quad (2.3)$$

is negative, which is clearly not possible. Negative ϵ and μ are resonant effects and they are necessarily dispersive and dissipative. A non-dispersive NRI would imply, for example, that time runs backwards for light in the medium [3]. For this reason is necessary to consider the permittivity and permeability as complex numbers.

Another remarkable property of the NIMs is negative refraction when light originally propagates in a dielectric. Negative sign in the refractive index gives to an unusual behavior of the wave vector in the plane interface between a dielectric and a NIM. The wave vector component that is orthogonal to the normal surface is preserved as usual. However, the parallel component has opposite signs in the dielectric and NIM and then refraction angle takes a negative value. This phenomenon can be understood in geometrical optics basis as a consequence of the negative sign of the refractive index in the Snell's law.

2.2 Surface Waves

Surface waves (SWs) are waves guided along an interface between two media of different EM properties. EM fields associated with SWs are localized in the vicinity of the interface and are damped out on both sides of it unlike the conventional bulk EM waves.

Although SWs have been studied theoretically since the beginning of the 20th century [106] only a close circle of specialists were interested on it. At that time there were not utilized except in radiophysics [107]. SWs start to be significant in optics for the first time in the 1970s when a laser source, coupling prism, and grating couplers were used to excite and detect them [108].

It is worth stressing that SWs are strongly confined in the interface leading to an enhancement of the EM field. Consequently, SWs have an extraordinary sensitivity to the boundary conditions. In particular, surface plasmon polariton-based devices exploiting extraordinary sensitivity to surface conditions are widely used in chemo- and bio-sensors [109]. Phenomena such as Raman scattering, second harmonic generation, and fluorescence are consequences of the optical enhancement of the EM field near the metal-dielectric interface [109–113].

Assuming passive media, NIMs are able to amplify waves that otherwise would have an exponential decay. We shall consider again the field of a plane wave spreading inside a NIM, but we now assume the optical parameters to be complex. The real parts of these parameters remains negative for NIMs, $\{\epsilon', \mu'\} < 0$. In addition, in a passive medium the imaginary components must be positive

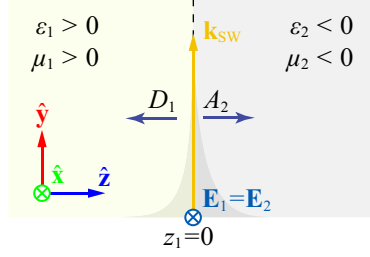


FIGURE 2.5: Surface wave propagation along a single dielectric-NIM interface for TE polarization. The propagation constant and the electric field are included.

$\{\varepsilon'', \mu''\} > 0$ in agreement with the Poynting theorem [114]. Under these conditions $\text{Im}(\mathbf{k}^2) < 0$ and

$$\{\text{Re}(k) > 0, \text{Im}(k) < 0\} \text{ or } \{\text{Re}(k) < 0, \text{Im}(k) > 0\}, \quad (2.4)$$

that means that the wave intensity decreases in a direction where light flux propagates but opposite to the wave vector propagation as we can expect from a lossy medium.

2.2.1 Surface Waves in a Dielectric-NIM Interface

By exciting an electromagnetic wave in a dielectric-NIM interface we produce a dipole-carrying excitation. The coupling state between the surface wave and a dipole-carrying excitation is commonly called a surface polariton [115].

To characterize the surface polaritons phenomenon we consider the simplest case: a planar interface normal to the z axis at $z_1 = 0$ as shown in Fig. 2.5. Waves propagate along the y direction without spatial variation in the perpendicular. We consider a dielectric medium with positive ε_1 and μ_1 at $z < 0$ and a NIM with

negative ϵ_2 and μ_2 at $z > 0$. Permittivities and permeabilities are both real for the sake of clarity.

As mentioned above, these SWs are confined in the dielectric-NIM interface. Therefore the field amplitudes in the dielectric and the NIM exponentially decay as we move away from the surface. To satisfy this condition the component of the wave vector that is perpendicular to the interface must be purely imaginary, $k_{zj} = i\kappa_j$. Consequently, in both media $j = \{1, 2\}$, the parameter

$$\kappa_j = \sqrt{k_{\text{SW}}^2 - k_0^2 \epsilon_j \mu_j}, \quad (2.5)$$

must be a real positive number, and the wave vector component along the propagation direction of the SW, called the propagation constant must satisfy the condition $k_{\text{SW}}^2 > \max\{k_0^2 \epsilon_1 \mu_1, k_0^2 \epsilon_2 \mu_2\}$ being $k_0 = 2\pi/\lambda_0$ the vacuum wavenumber.

Equations (A.1) and (A.4) and their dual equations from Appendix A can be applied to the electric and magnetic field of a SW by considering two semi-infinite media. Amplitudes of the propagating waves in the dielectric medium, C_1 , and counterpropagating waves in the NIM medium, B_2 , vanish since we do not consider any external source. In the dielectric halfspace $z < 0$

$$\mathbf{E}_1(y, z) = D_1 e^{\kappa_1 z} e^{ik_{\text{SW}} y} \hat{\mathbf{x}}, \quad (2.6a)$$

$$\mathbf{H}_1(y, z) = \frac{-D_1}{\omega \mu_0 \mu_1} e^{\kappa_1 z} e^{ik_{\text{SW}} y} (i\kappa_1 \hat{\mathbf{y}} + k_{\text{SW}} \hat{\mathbf{z}}), \quad (2.6b)$$

and in the NIM halfspace,

$$\mathbf{E}_2(y, z) = A_2 e^{-\kappa_2 z} e^{ik_{\text{SW}} y} \hat{\mathbf{x}}, \quad (2.7a)$$

$$\mathbf{H}_2(y, z) = \frac{A_2}{\omega \mu_0 \mu_2} e^{-\kappa_2 z} e^{ik_{\text{SW}} y} (-i\kappa_2 \hat{\mathbf{y}} + k_{\text{SW}} \hat{\mathbf{z}}). \quad (2.7b)$$

Applying the boundary conditions (A.5) in $z_1 = 0$ we conclude that $D_1 = A_2$. We also conclude that

$$\frac{\kappa_2}{\kappa_1} = -\frac{\mu_2}{\mu_1}. \quad (2.8)$$

It should be recalled that κ must be real and positive. Thus, μ_1 and μ_2 must have opposite signs to verify Eq. (2.8). This is why TE surface modes exist only at interfaces between materials with opposite signs in their magnetic permeabilities.

Combining Eq. (2.8) and (2.5) we arrive to the dispersion relation for a SW propagating along the interface at $z_1 = 0$,

$$k_{\text{SW}} = k_0 \sqrt{\frac{\mu_1 \mu_2}{\mu_1 + \mu_2} \frac{\varepsilon_2 \mu_1 - \varepsilon_1 \mu_2}{\mu_1 - \mu_2}}. \quad (2.9)$$

It can be proved that this function is also valid for both real and complex permittivities and permeabilities.

The TE SWs have been characterized applying the transfer matrix method in a dielectric-NIM interface. It is possible to characterize SWs for TM-modes by following an analogous procedure. Alternatively, an expression for TM-modes can be inferred applying the duality theorem summarized in Table A.1, on the above-deduced TE-modes expressions. In this particular case, the permittivities must have opposite signs in both materials to satisfy the dual of Eq. (2.8), namely $\kappa_2 \varepsilon_1 = \kappa_1 \varepsilon_2$.

Surface waves properties in air-NIM interfaces are examined by taking a closer look at their dispersion relation (2.9) and its dual for TM-modes. Figure 2.6(a)

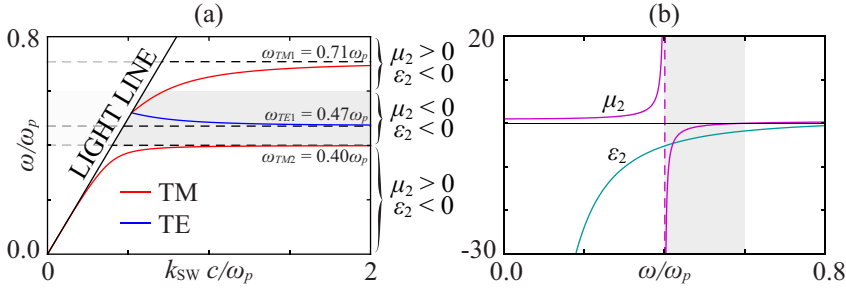


FIGURE 2.6: (a) Dispersion relation for TE and TM SWs sustained at an air-NIM interface. NIM optical parameters are depicted on (b). Shaded region corresponds to frequencies where ϵ_2 and μ_2 are negative simultaneously.

shows the SW dispersion curves in a NIM with optical parameters

$$\epsilon_2(\omega) = 1 - \frac{\omega_p^2}{\omega^2}, \quad (2.10a)$$

$$\mu_2(\omega) = 1 - \frac{F\omega^2}{\omega^2 - \omega_0^2}, \quad (2.10b)$$

similar to those that have been achieved with artificial structures [115]. This dispersive parameter are plotted in Fig. 2.6(b) being $\omega_p = 10$ GHz, $\omega_0 = 4$ GHz, and $F = 0.56$ extracted from Ref. [115]. The frequency range in which both ϵ_2 and μ_2 are negative extends from ω_0 up to $0.6\omega_p$. While it is possible to find SW modes out of this range as long as the sign of μ_1 and μ_2 (ϵ_1 and ϵ_2) are opposite in TE (TM) modes, we focus on modes connected with a NIM. In this regard, only the TE-mode branch in Fig. 2.6(a) lies completely within the frequency range in which the media are left-handed. The upper branch, is only partially inside this range, while the lowest branch, lies outside this range. It is also important to highlight that due to their bound nature, the SW must be evanescent at both sides of the interface. That only can be achieved in the part of the dispersion curves lying at the right side of the light line in Figure 2.6(a).

There are three dashed lines in Fig. 2.6(a) denoting the frequencies in which the three surface mode branches approach asymptotically to a limit value. The TE asymptotic values can be found by inserting the ε_j and μ_j dispersive values into the dispersion relation (2.9) yielding to

$$\omega_{\text{TE1}} = \frac{\omega_0}{\sqrt{1 - \frac{F}{1 + \mu_1}}}. \quad (2.11)$$

In this limiting case k_{SW} goes to infinity as the frequency approaches to ω_{TE1} , and the group velocity, v_g , goes to 0. The mode thus acquires electrostatic character. Following the same procedure we can obtain the corresponding frequencies for TM-modes,

$$\omega_{\text{TM1}} = \frac{\omega_p}{\sqrt{1 + \varepsilon_1}}, \quad (2.12a)$$

$$\omega_{\text{TM2}} = \omega_0. \quad (2.12b)$$

At these frequencies the p -polarized waves acquire a magnetostatic character.

The above discussions for Fig. 2.6 implicitly assume an ideal NIM with real ε_2 and μ_2 . However, permeability and permittivity both suffer from losses, therefore, ε_2 and μ_2 are complex. Furthermore, the wave vector component k_{SW} is also complex. That makes bound SWs having a propagation constant $\text{Re}(k_{\text{SW}})$ that approaches a maximum finite value. There is also an attenuation on its amplitude as the SW propagates since $\text{Im}(k_{\text{SW}}) > 0$. This attenuation is especially relevant in the optic and infrared range.

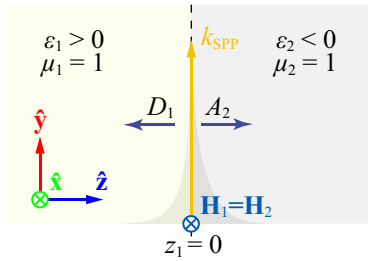


FIGURE 2.7: Surface plasmon polariton propagation at a single dielectric-metal interface. The SPP propagation constant and the magnetic field are included.

2.2.2 Surface Waves in Metals: SPPs

The SW in metal-dielectric interface, also called surface plasmon polariton (SPP) refers to the coupling in a surface between the quanta of the collective excitation of free electrons with a surface polariton. We are going to approach this phenomenon from the point of view of the classical electromagnetism.

The simplest geometry sustaining SPPs, depicted in Fig. 2.7, is that of a single flat interface between a dielectric non-absorbing half space with positive real dielectric constant ϵ_1 and an adjacent metal half space described via a dielectric function ϵ_2 . Both are nonmagnetic materials. In this scenario SWs are confined to the interface, i.e. with evanescent decay in the z direction. The procedure followed in Section 2.2.1 to infer the fields and dispersion relation for a SW in a dielectric-NIM interface remains valid in terms of the wave field formulation. TE SWs cannot exist due to the presence of nonmagnetic materials. However, for TM polarization, the dispersion relation,

$$\frac{\kappa_2}{\kappa_1} = -\frac{\epsilon_2}{\epsilon_1}, \quad (2.13)$$

can be satisfied. The corresponding SPP wavenumber results,

$$k_{\text{SPP}} = k_0 \sqrt{\frac{\epsilon_1 \epsilon_2}{\epsilon_1 + \epsilon_2}}. \quad (2.14)$$

Now we want to examine the properties of SPPs by inspecting their dispersion relation depicted in Fig 2.8(a) for an air-metal interface. The metal permittivity may be characterized using Eq. (2.1a) in the limit case when $\omega_0 \rightarrow 0$ and considering only one oscillator mode,

$$\epsilon_2(\omega) = 1 - \frac{\omega_p^2}{\omega(\omega + i\gamma)}. \quad (2.15)$$

Due to their bound nature, SPP only exist in the part of the dispersion curve lying at the right of the light line. The red lines in Fig. 2.8(a) draws (2.14) for a lossless metal, i.e. $\gamma = 0$. For large wave vectors the frequency of the SPP approaches the characteristic surface plasmon frequency

$$\omega_{\text{SP}} = \frac{\omega_p}{\sqrt{1 + \epsilon_1}}, \quad (2.16)$$

which is formally similar to Eq. (2.12a). As mentioned previously, the mode acquires a magnetostatic character [116].

The above discussions illustrated in Fig. 2.8(a) have assumed an ideal conductor. On that context the damping frequency have a non zero value and therefore ϵ_2 and k_{SPP} are both complex. Blue lines in Fig. 2.8(a) shows the dispersion relation of SPPs propagating in an air-silver interface, following the Drude model for the metal. Finally a more realistic SPP dispersion relation is depicted in Fig. 2.8(b). Johnson and Christy tabulated values for Ag [103] are introduced in Eq. (2.14).

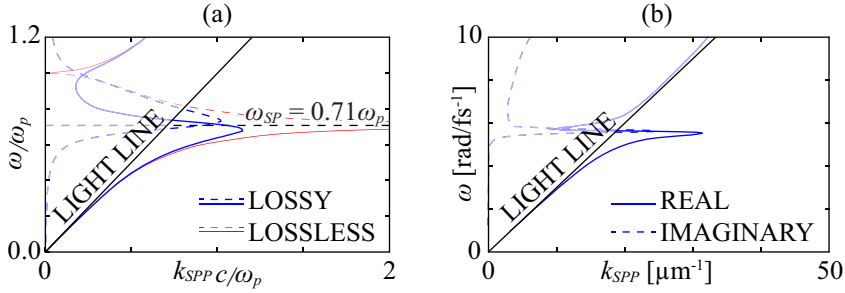


FIGURE 2.8: Dispersion relation of SPPs at a air-metal interface. Solid line represent the real part of k_{SPP} and dashed lines represent the imaginary part. (a) Drude damping $\gamma = 0$ (red) and $\gamma = 97.5 \times 10^{-3} \omega_p$ (blue). (b) Same dispersion relation replacing the Drude metal by Johnson and Christy tabulate values for Ag [103].

Compared with the dispersion relation of completely undamped SPPs it can be seen that the bound SPPs approach a maximum, finite wavenumber.

Due to the penetration of the evanescent fields inside the materials sustaining the SPP, we may define an evanescent decay length for the dielectric ($j = 1$) and for the metal ($j = 2$) as

$$l_j = \frac{1}{2\text{Re}(\kappa_j)}, \quad (2.17)$$

which is of particular relevance in subwavelength-resolution image formation in the canalization regimen [56], as we will see in Chapter 5. By substituting (2.14) into Eq. (2.5), l_j can be rewritten in terms of permittivities, in the media,

$$l_j = \frac{1}{2k_0} \sqrt{\frac{\epsilon_1 + \epsilon_2}{-\epsilon_j^2}}. \quad (2.18)$$

We see from this equation that the evanescent decay length goes to zero at ω_{SP} where $\epsilon_2 = -\epsilon_1$ disregarding losses. At frequencies close to the surface plasmon frequency, in which the confinement is maximum, l_1 and l_2 are of the same order

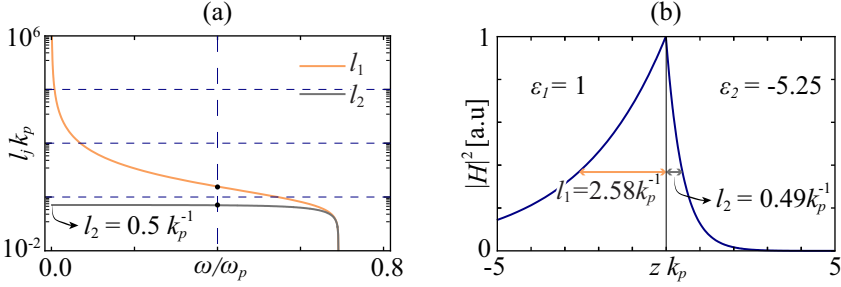


FIGURE 2.9: (a) Evanescent decay length of the SPP in the dielectric (orange) and a lossless Drude metal (gray). (b) The magnetic field intensity of a given SPP at a frequency $\omega = 0.4\omega_p$.

of magnitude, however, at lower frequencies these two decays increasingly become dissimilar. This can be clearly seen in Fig. 2.9(a) where l_j is plotted as a function of ω in an air-metal interface. The evanescent decay lengths are normalized to the inverse of the plasma wavenumber, $k_p = \omega_p/c$. The metal permittivity has been described by the Drude model (2.15) with zero damping frequency. It is noteworthy that the evanescent decay length of the metal is limited to the limiting value $1/2k_p$. If we consider a realistic metal like silver, with $\omega_p = 13.7$ fs [105] then $k_p^{-1} = 21.9$ nm and the evanescent decay length can never be longer than ~ 10 nm. Note that the decay l_2 remains close to its maximum value except in the vicinity of ω_{SP} . Indeed, Fig. 2.9(b) shows that l_2 is $0.49 k_p^{-1}$ by evaluating $|\mathbf{H}|^2$ at $\omega = 0.4\omega_p$. As a consequence, the design of SPP-based structures with coupling of SWs has to be performed in nanoscale.

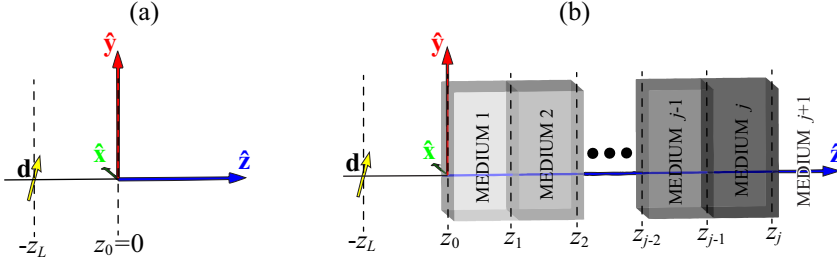


FIGURE 2.10: Schematic of a point dipole (a) in free space and (b) in a layered medium.

2.3 Point Dipole Sources

In this Section we evaluate the electric field generated by a point dipole in free space and near a multilayered nanostructure, with a particular interest in the distribution of the transmitted field. The free space field solution is examined as a starting point. Consider a point dipole placed at $\mathbf{r}_L = (0, 0, -z_L)$ in a homogeneous and isotropic medium characterized by μ_1 and ϵ_1 depicted on Fig. 2.10. The electric field at $\mathbf{r} = (x, y, z)$ can be expressed as [117]

$$\mathbf{E}(\mathbf{r}, \omega) = \mu_1 \mu_0 \omega^2 \overline{\mathbf{G}}(\mathbf{r}, \mathbf{r}_L, \omega) \cdot \mathbf{d}, \quad (2.19)$$

where $\overline{\mathbf{G}}$ is the Green tensor in free space and \mathbf{d} is the electric dipole moment of the point source. Using Weyl scalar representation to develop spherical waves into plane wave function, the electric dipole field in the half-space $z > -z_L$ can be described as [118, 119]

$$\mathbf{E}(\mathbf{r}, \omega) = \frac{i\mu_1 \mu_0 \omega^2}{8\pi^2} \int \int_{-\infty}^{\infty} \frac{e^{i[\mathbf{k}_\perp \cdot \mathbf{R} + k_{z1}(z+z_L)]}}{k_{z1}} [(\hat{\mathbf{s}} \otimes \hat{\mathbf{s}} + \hat{\mathbf{p}} \otimes \hat{\mathbf{p}}) \cdot \mathbf{d}] d^2 \mathbf{k}_\perp, \quad (2.20)$$

being $\mathbf{k}_\perp = (k_x, k_y)$, $\mathbf{R} = (x, y)$ and \otimes the tensor product. The unitary vectors $\hat{\mathbf{s}}$ and $\hat{\mathbf{p}}$ points in the directions of the electric field for s - and p -polarization respectively: $\hat{\mathbf{s}} = (\mathbf{k}_\perp/k_\perp) \times \hat{\mathbf{z}}$ and $\hat{\mathbf{p}} = \hat{\mathbf{s}} \times \hat{\mathbf{k}}_u$ where $k_\perp = |\mathbf{k}_\perp|$ and $\hat{\mathbf{k}}_u$ is the unitary vector in the direction of \mathbf{k} .

Let us now consider a stratified medium composed of $j-1$ layers shown schematically in Fig. 2.10. Provided that the point source is set in the medium number 1, the electric field generated by the dipole in the $j+1$ space at z_L can be written as

$$\mathbf{E}(\mathbf{r}, \omega) = \omega^2 \mu_1 \mu_0 \bar{\bar{\mathbf{G}}}_{\text{MLayer}}(\mathbf{r}, \mathbf{r}_L, \omega) \cdot \mathbf{d}, \quad (2.21)$$

where the Green tensor of the multilayer is [120]

$$\bar{\bar{\mathbf{G}}}_{\text{MLayer}}(\mathbf{r}, \mathbf{r}_L, \omega) = \frac{i}{8\pi^2} \int_0^\infty \frac{k_\perp}{k_{z1}} e^{ik_{z1}(z-z_L)} (T_s \bar{\bar{\mathbf{S}}} + \frac{Z_{j+1}}{Z_1} T_p \bar{\bar{\mathbf{P}}}) dk_\perp, \quad (2.22)$$

being T_s the transmittance for the electric field at s -polarization [see Eq. (A.11a)] and T_p its dual quantity for the magnetic field at p -polarization. It must be emphasized that T_p applies to a magnetic field. Is necessary to add in (2.22) the ratio Z_{j+1}/Z_1 , where

$$Z_j = \sqrt{\frac{\mu_0 \mu_j}{\epsilon_0 \epsilon_j}}, \quad (2.23)$$

is the impedance of the medium j , to include T_p in a function that applies to an electric field.

The elements of the tensor $\overline{\mathbf{S}}$ are

$$S_{11} = \pi J_0(k_{\perp} R) + \pi J_2(k_{\perp} R) \cos(2\varphi), \quad (2.24a)$$

$$S_{12} = S_{21} = \pi J_2(k_{\perp} R) \sin(2\varphi), \quad (2.24b)$$

$$S_{22} = \pi J_0(k_{\perp} R) - \pi J_2(k_{\perp} R) \cos(2\varphi), \quad (2.24c)$$

$$S_{13} = S_{23} = S_{31} = S_{32} = S_{33} = 0. \quad (2.24d)$$

In Eqs. (2.24) the function J_i represents the Bessel function of order i , $R = |\mathbf{R}|$ and φ is the azimuthal angle of \mathbf{R} as measured with respect to the x axis. Similarly the elements of $\overline{\mathbf{P}}$ are

$$P_{11} = \frac{k_{z1}^2}{k_1^2} [\pi J_0(k_{\perp} R) - \pi J_2(k_{\perp} R) \cos(2\varphi)], \quad (2.25a)$$

$$P_{12} = P_{21} = -\frac{k_{z1}^2}{k_1^2} [\pi J_2(k_{\perp} R) \sin(2\varphi)], \quad (2.25b)$$

$$P_{13} = P_{31} = -\frac{k_{\perp} k_{z1}}{k_1^2} [2\pi i J_1(k_{\perp} R) \cos(\varphi)], \quad (2.25c)$$

$$P_{22} = \frac{k_{z1}^2}{k_1^2} [\pi J_0(k_{\perp} R) + \pi J_2(k_{\perp} R) \cos(2\varphi)], \quad (2.25d)$$

$$P_{23} = P_{32} = -\frac{k_{\perp} k_{z1}}{k_1^2} [2\pi i J_1(k_{\perp} R) \sin(\varphi)], \quad (2.25e)$$

$$P_{33} = \frac{k_{\perp}^2}{k_1^2} [2\pi J_0(k_{\perp} R)]. \quad (2.25f)$$

The electric field dipole function will be applied to a NIM slab in Chapter 4.

Chapter 3

1D Metamaterials

Photonic band-gap materials, sometimes referred as photonic crystals, are artificial inhomogeneous structures composed of periodic regions of material with a specific permittivity and permeability different from the surrounding homogeneous background media. We want to focus our attention in the 1D case of the periodic layered media (PLMs): a special kind of multilayered media in which thin films of different material are stacked in a periodic fashion. Allowed and forbidden energy bands will be determined by the periodic potential function modifying the propagation of EM waves. The spatial dispersive response of the PLM depends on the direction of the wave vector in a more complicated manner than a homogeneous material. Nonetheless, the metamaterial periodicity may be at scales much smaller than the wavelength for which an effective medium approach can simplify the calculations. Wave propagation in these media exhibits many potentially useful phenomena including birefringence, Bragg reflection and optical stop bands.

In Chapter 3 we introduce a way to solve the fields and dispersion relations in an infinite PLM through the Bloch waves. Band structures and dispersion curves for metal-dielectric are also analyzed, paying special attention to the losses. A complementary analysis for dielectric-NIM dispersion curves is done. We also evaluate the consequences of deviating from the ideal matching conditions between the optical constants of the two media.

As an alternative to the Bloch formulation the effective media theory is introduced for the analysis of PLM with subwavelength periodicity. Metal-dielectric PLM dispersion relations are revised within this approach. A more in-depth analysis of effective media in the EMA shows that their dispersion curves can be either hyperbolic or elliptic. The agreement between these predictions and the real dispersion curves is analyzed. We found that nonlocal effects lead to relevant disparities and propose some corrections in the EMA theory to solve it.

Finally the possibility to induce single-polarization double refraction by nonlocal effects is considered and numerically tested.

3.1 Bloch Modes

Consider the propagation of EM radiation in a PLM like the one outlined in Fig. 3.1. We assume that the period has a width, $\Lambda = w_1 + w_2$, where $w_1 = z_{j+1} - z_j$ and $w_2 = z_{j+2} - z_{j+1}$ are the thickness of the layers $j + 1$ and $j + 2$, respectively, thus $\Lambda = z_{j+2} - z_j$. The layers are set normally to the z axis, and

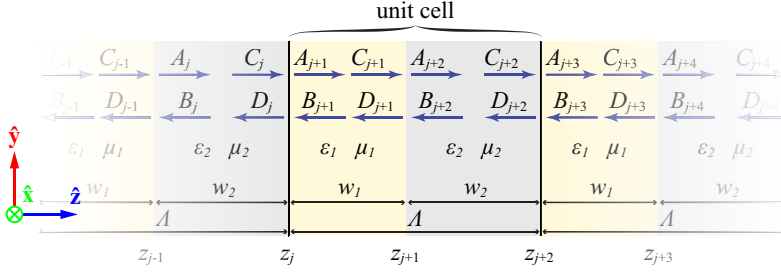


FIGURE 3.1: Periodic layered media outline. Amplitudes of propagating (A_j and C_j) and counterpropagating waves (B_j and D_j) are included

therefore the permittivity and permeability profile in a unit cell are,

$$(\epsilon, \mu) = \begin{cases} (\epsilon_1, \mu_1), & z_j < z < z_{j+1}, \\ (\epsilon_2, \mu_2), & z_{j+1} < z < z_{j+2}. \end{cases} \quad (3.1)$$

PLMs are invariant under lattice translation and consequently $\epsilon(z) = \epsilon(z + \Lambda)$. Correspondingly, permeability satisfies the condition $\mu(z) = \mu(z + \Lambda)$. The shift invariance constraint also applies to the electromagnetic fields. From here on we will consider only TE modal wave fields in order to deduce the dispersion relation in PLMs. By using the duality theorem we may infer the dispersion relation for TM waves straightforwardly. Thus, considering the Floquet-Bloch theorem and TE-modes, the electric field satisfies [121]

$$\mathbf{E}_{j+2}(y, z + \Lambda) = \mathbf{E}_j(y, z) e^{iK\Lambda}, \quad (3.2)$$

where K is known as the Bloch wavenumber and \mathbf{E}_j is the field inside the j th layer analytically shown in (A.1). The phase gained by the Bloch wave between z_j and

z_{j+2} in terms of the column vector representation introduced in the Appendix A is

$$\begin{pmatrix} C_j \\ D_j \end{pmatrix} = e^{-iK\Lambda} \begin{pmatrix} C_{j+2} \\ D_{j+2} \end{pmatrix}. \quad (3.3)$$

Expanding the left column vector evaluated at z_j via the transfer matrix method it follows that the previous equation satisfies the eigenvalue problem

$$\bar{\bar{M}}_{s\text{cell}} \begin{pmatrix} C_{j+2} \\ D_{j+2} \end{pmatrix} = e^{-iK\Lambda} \begin{pmatrix} C_{j+2} \\ D_{j+2} \end{pmatrix}, \quad (3.4)$$

being the unimodular transfer matrix,

$$\bar{\bar{M}}_{s\text{cell}} = \bar{\bar{D}}_{s_j}^{-1} \bar{\bar{D}}_{s_{j+1}} \bar{\bar{P}}_{j+1} \bar{\bar{D}}_{s_{j+1}}^{-1} \bar{\bar{D}}_{s_{j+2}} \bar{\bar{P}}_{j+2}. \quad (3.5)$$

To solve the eigenvalue problem we look for non-trivial solutions of

$$\det \left[\bar{\bar{M}}_{s\text{cell}} - e^{-iK\Lambda} \bar{\bar{I}} \right] = 0, \quad (3.6)$$

where $\bar{\bar{I}}$ is the 2×2 identity matrix. After some algebraic manipulations we found two independent equations,

$$e^{-iK\Lambda} = \text{tr}_s/2 \pm i\sqrt{1 - (\text{tr}_s/2)^2}, \quad (3.7)$$

where

$$\text{tr}_s = 2 \cos(w_1 k_{z1}) \cos(w_2 k_{z2}) - \frac{k_{z1}^2 \mu_2^2 + k_{z2}^2 \mu_1^2}{k_{z1} \mu_1 k_{z2} \mu_2} \sin(w_1 k_{z1}) \sin(w_2 k_{z2}). \quad (3.8)$$

is the trace of the unimodular transfer matrix. Equation (3.7) can be reduced to

$$\cos(K\Lambda) = \text{tr}_s/2, \quad (3.9)$$

by trigonometric manipulations. A p -polarization equivalent equation can be found by applying the duality theorem from Table A.1. The dispersion curve is reproduced periodically in adjacent K -frequency bands with a $2\pi/\Lambda$ period.

By simple inspection of the wave dispersion equation we found that in lossless materials the regimes where $|\text{tr}_s|/2 < 1$ correspond to real values of K . These propagating waves travel along the metamaterial without attenuation. When $|\text{tr}_s|/2 < 1$ the amplitude of the Bloch waves will exponentially decay as it goes forward in the z axis. The band edges are the regions in-between allowed and forbidden bands, therefore they satisfy $\text{tr}_s = \{2, -2\}$. This criterion will be revised further when the material losses are taken into account.

The group velocity, $\mathbf{v}_g \equiv \nabla_{\mathbf{k}} \omega$, can be determined through the dispersion curves. Moreover, for a monochromatic beam, the group velocity of this wavepacket is always perpendicular to the dispersion curves. Finally, the dispersion curves provide information about the evanescent decay length of a given Bloch wave, as we will discuss later.

3.2 Metal-Dielectric Periodic Layered Media

Let us examine the spatial dispersion in PLMs composed of a dielectric and a metal. In Fig. 3.2(a)-(d) TM and TE propagating Bloch wave domains are plotted

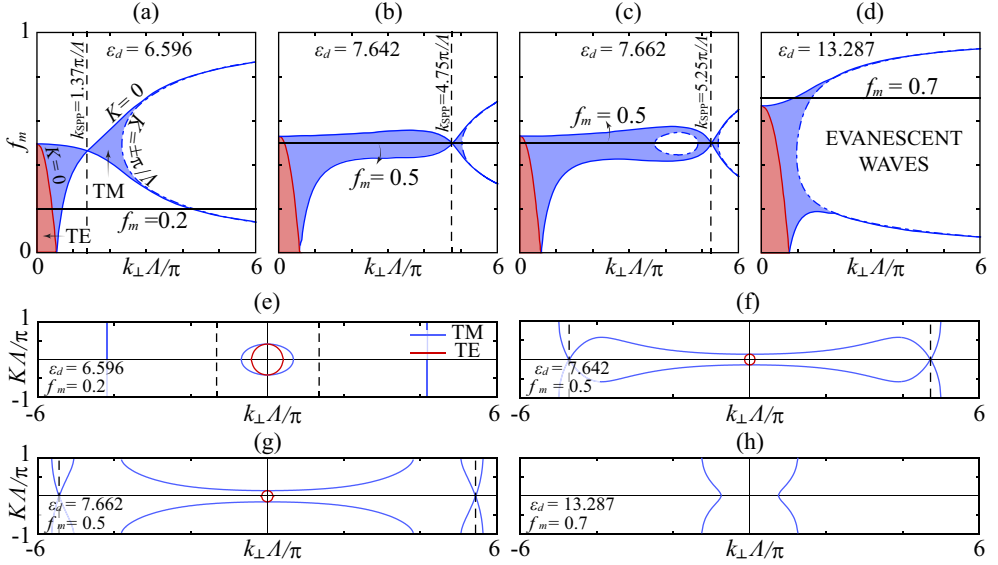


FIGURE 3.2: (a)-(d) allowed bands for TE-modes (red area) and TM-modes (blue area) in periodic metal-dielectric media. The metal permittivities are set to $\epsilon_m = -7.754$ at the wavelength 485 nm. In every case, cells have a thickness of 50 nm. (e)-(h) exact dispersion curves for the f_m highlighted in subfigures (a)-(d).

for different PLMs as a function of the metal filling factor,

$$f_m = w_m/\Lambda, \quad (3.10)$$

where w_m is the width of the metallic layers. The wavelength in the plots is set to $\lambda_0 = 485$ nm. The lossless permittivity is $\epsilon_m = -7.754$ while the dielectric permittivities, ϵ_d , changes from one plot to another.

We found band structures that significantly differ depending on the polarization. The TE-modes that do not allow the propagation of SWs, as we introduced in Section 2.2.2, have a simple band structure. The band edges of spatial frequencies k_{\perp} occurring at $K = 0$ and $K = \pi/\Lambda$ are shown in Fig. 3.2(a)-(d) with a solid red

(blue) line for the TE (TM) modes. In the limit case in which $f_m = 0$, the PLM will become a dielectric. Dielectrics are homogeneous and isotropic media thus, the TE- and TM-modes have the same spatial band structure. Consequently, both band edges will be found at $k_{\perp} = k_0\sqrt{\epsilon_d}$. The higher TE propagating frequencies became evanescent as f_m increase and thus, the spatial bandwidth goes to 0. In the other hand, employing higher ϵ_d the spatial bandwidth will increase. Furthermore, the range of f_m allowing to transmit TE-modes gets larger as ϵ_d grows.

As we mentioned above TE- and TM-modes dispersion relations are equal when $f_m = 0$. They are also equal in the normal incidence case, $k_{\perp} = 0$. However, in some cases we found a broader spatial band structure for the TM-modes, primarily due to the propagation and tunneling of SWs in the metal-dielectric interface. Thus, it is possible for TM-modes to have a superresolving behavior, propagating frequencies that are over the diffraction limit. The spatial bandwidth is connected with the k_{SPP} of a single metal-dielectric interface, introduced in Eq. (2.13). This spatial frequency is outlined with black dashed lines in Fig. 3.2. Is easy to prove that there is only one f_m at the given k_{SPP} where we can find TM-polarized solutions to the Eq. (3.9), $f_{\text{SPP}} = \epsilon_d/(\epsilon_d + |\epsilon_m|)$. The band edges in Fig. 3.2(a)-(d) cut at $k_{\perp} = k_{\text{SPP}}$. We see in Eq. (2.13) that this point moves to higher k_{\perp} as ϵ_d increases. This displacement to higher frequencies could allow broader spectral bandwidths, however, the spatial bandwidth cannot get indefinitely broader. There is a limit k_{SPP} up to which the first band splits. Comparing Fig. 3.2(b) and (c) we can see the gap in the TM spatial bands created by this splitting. In addition it always exists another TM allowed band over the k_{SPP} frequency. It is sustained exclusively by plasmon resonances, thus, it is limited to the range of spatial frequencies close to these resonances. However, the losses strongly limit the higher bandwidths as will be discussed later.

Figure 3.2(e)-(f) plots the contour lines derived from Eq. (3.9) for the filling factors outlined with black solid lines in Figs. 3.2(a)-(d). By simple inspection of these plots we realize that the TE-modes have circular dielectric-like contours so this polarization is spectrally isotropic. As we get far from the normal incidence, $k_{\perp} = 0$, TM dispersion curves differ from the TE curves. For instance, Fig. 3.2(e) reveals that the TM band is clearly anisotropic, and there is a second allowed band purely sustained by plasmons resonances at frequencies over k_{SPP} . In Fig. 3.2(f) dispersion for a PLM with high k_{SPP} and filling factor close to f_{SPP} . A very large spatial allowed band appears. Furthermore, in a wide k_{\perp} range the Bloch wavenumber, K , remains almost constant. As the group velocity is perpendicular to the dispersion curves the light propagation will be nearly diffraction free. This kind of propagation regimen is called canalization [56]. At high ϵ_d we find that a new band gap divides this band creating a structure of three bands as we can see in Fig. 3.2(g). Figure 3.2(h) shows spatial dispersion at a higher f_m . Consequently, dispersion dominantly has a metallic-like behavior. There is only an small TM propagating band far from the normal incidence. There are no solutions for propagating TE-modes.

3.2.1 Effects of Losses in PLMs

The above discussion has been made without taking into account the metal losses. The EM waves are commonly considered propagation modes at spatial frequencies k_{\perp} at which the complex Bloch wavenumber, $K \equiv K' + iK''$ satisfies $K'' = 0$ and evanescent when $K' = 0$. However, the nature of the waves in real metal-dielectric periodic media cannot longer be set as purely propagating or evanescent by the previous criterion because K is always a purely imaginary number. These

Bloch waves with mixed components are always attenuated during their propagation. It is convenient to classify these waves as a function of their evanescent decay length l_{PLM} ,

$$l_{\text{PLM}} = \frac{1}{2K''}. \quad (3.11)$$

Having in mind applications like near-field image formation, we will call *low decay inhomogeneous waves* to the waves with l_{PLM} longer than $\lambda_0/4$. Similarly, the Bloch waves with $l_{\text{PLM}} < \lambda_0/4$ will be referred as *high decay inhomogeneous waves*. It is worth stressing that losses strongly affect, specially in the visible and near-IR, thus we do not expect a l_{PLM} longer than few wavelengths for Bloch waves within the PLM. That fact limits the range of functional performance of PLM to the near field.

By considering that K'' is connected with k_{\perp} throughout Eq. (3.9) we will split the spatial bandwidth of a PLM in bands. We will refer to the k_{\perp} spatial frequency ranges in which $K'' < 2/\lambda_0$ as low decay bands. Complementary to this, we will call high decay bands to the spatial frequency ranges in which $K'' > 2/\lambda_0$. Moreover, we will define cutoff frequencies k_{cut} , separating the low and high decay bands. Note that low decay bands and high decay bands are, in practical terms, the same than allowed bands and forbidden bands in lossless PLMs.

In Fig. 3.3 the dispersion curves from Figs. 3.2(e)-(h) have been replotted taking into account realistic losses in silver ($\epsilon_m = 7.754 + 0.727i$). The cutoff frequencies have been pointed with dotted vertical lines. High decay bands are shaded in blue. If we compare K' in Fig. 3.3 with its equivalent disregarding losses in Figs. 3.2(e)-(h) we find differences that are significant in the high decay bands. Metal losses in the structured media leads to a reduction of the bandwidth in the low decay band, however K' remains almost unaltered within this spectral band.

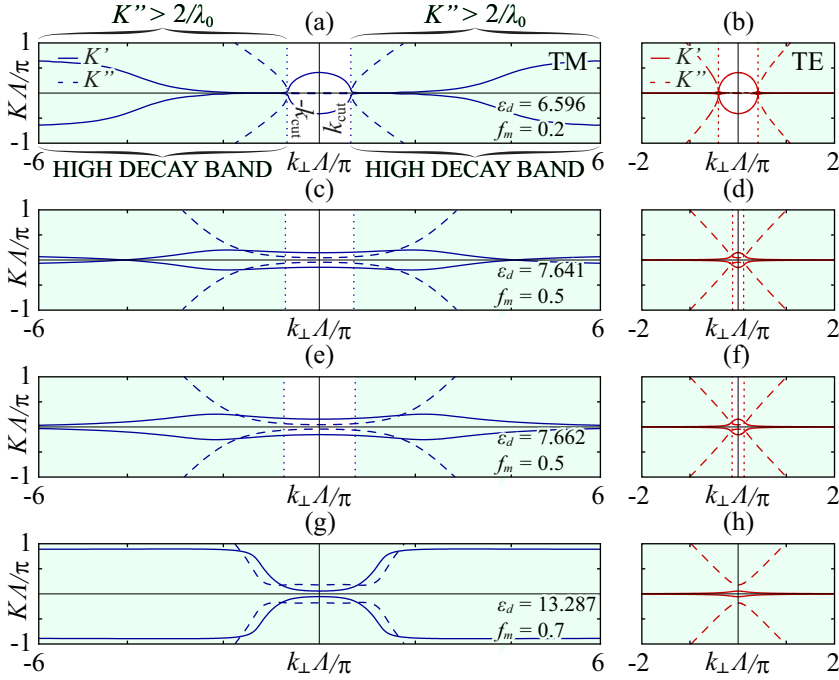


FIGURE 3.3: Spatial dispersion for TM-modes (blue) and TE-modes (red) in periodic metal-dielectric media with $\Lambda = 50$ nm. The metal permittivity is set to $\epsilon_m = -7.754 + 0.727i$ and the wavelength is 485 nm.

For instance, $k_{\text{cut}} = 0.682\pi/\lambda_0$ for TM-modes in Fig. 3.3(a) while the equivalent lossless cutoff frequency is $0.686\pi/\lambda_0$. On the other hand, low decay bands in the TE-modes from Figs. 3.3(d) are strongly reduced compared with the lossless case. Figure 3.3(d) cutoff frequency is $0.11\pi/\Lambda$ while the equivalent frequency in the lossless periodic medium is $k_{\text{cut}} = 0.15\pi/\Lambda$. Also TM-modes low decay band from Figs. 3.3(c) are drastically reduced due to the presence of losses and k_{cut} is reduced to $k_{\text{cut}} = 0.73\pi/\Lambda$ with $5.00\pi/\Lambda$ in Fig. 3.2(c). Hence very large bandwidth predicted in lossless TM Figs. 3.2(f)-(g) are not realistic. Nevertheless, by making $f_m = 0$ we found that the cutoff frequency for the dielectric, $k_{\text{cut}} = 0.57\pi/\Lambda$, is smaller than the previous lossy k_{cut} . Thus the metal-dielectric PLM can show wider low decay bandwidths rather than the dielectric itself. In the

opposite scenario, Fig. 3.3(g) does not show low decay bands at all in the TM modes. The equivalent lossless medium has low decay bands from $k_{\perp} = 0.75\pi/\Lambda$ to $k_{\perp} = 1.33\pi/\Lambda$. The large presence of a lossy metal in the PLM, a 70 per cent of it, prevents in practical terms the propagation of Bloch waves within the nanostructure. In conclusion, the filling factor of the metal governs the dissipative effects in the metamaterial, thus low values of f_m are of great convenience to achieve large spatial bandwidths.

3.3 Dielectric-NIM Stratified Media

So far, we have considered metal-dielectric periodic structures. Moving on to dielectric-NIM structures, TM and TE SWs can exist. Consequently both polarizations are able to interact with free-space evanescent waves. Despite the different possibilities that NIMs confer to the design of PLM, in this Thesis we will focus on the particular case that $f_{\text{NIM}} = 0.5$, and the optical constants are related by $\epsilon_d = -\epsilon_{\text{NIM}}$ and $\mu_d = -\mu_{\text{NIM}}$. We will refer to these last conditions as the perfect matching conditions. In principle, this kind of structures allow the propagation of an extremely large number of k_{\perp} without either diffraction or attenuation. For that reason dielectric-NIM structures are of particular relevance in superlensing [122].

In the limit case when the perfect matching conditions are fulfilled the dispersion relation becomes $K(k_{\perp}) = 0$, thus, v_g will point in the direction of the layers periodicity for all the frequencies. It is noteworthy that all the frequencies, even the evanescent ones will propagate without attenuation in the perfect matching case caused by the enhancement of evanescent waves near the interfaces. Unavoidable losses in realistic NIMs are the main reason why the perfect matching conditions

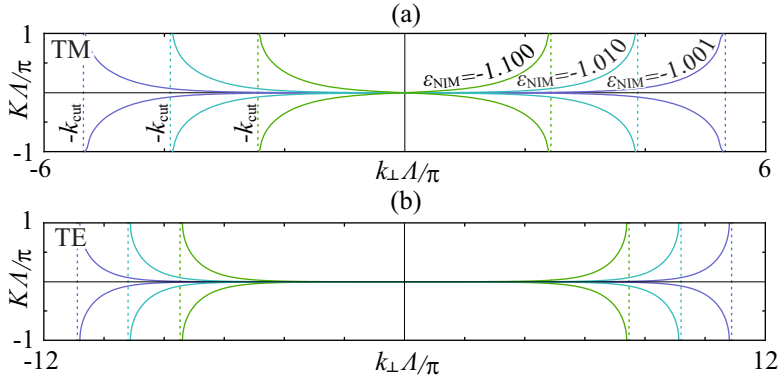


FIGURE 3.4: (a) Full wave air-NIM TM-modes dispersion curves and (b) TE-modes dispersion curves. The wavelength is set to $10\ \mu\text{m}$ with a NIM filling factor $f_{\text{NIM}} = 0.5$. The period is $500\ \text{nm}$ long and the permeability is set to $\mu_{\text{NIM}} = -1$ in the NIM.

cannot be fulfilled. Besides, even in lossless NIMs small deviations from the perfect matching conditions on the electromagnetic constants modifies the dispersion curves as we can see in Fig. 3.4. The TE- and TM-modes dispersion curves for an air-NIM periodic structure have been plotted. Permeability in the NIM is set to $\mu_{\text{NIM}} = -1$ while the permittivity takes values that deviate slightly from the perfect matching conditions, from $\epsilon_{\text{NIM}} = -1.001$ to $\epsilon_{\text{NIM}} = -1.100$. Insofar as the permittivity deviates from the perfectly matching conditions, k_{cut} shifts to smaller spatial frequency. Accordingly, the spatial bandwidth reduces as ϵ_d deviates from the perfect matching conditions. This phenomenon occurs for both polarizations, however, TE-modes bandwidth decreases at a slower rate. On the contrary, we can deduce through the duality theorem that TE-modes bandwidth decreases faster than TM-modes bandwidth under permittivity deviations from the perfect matching conditions.

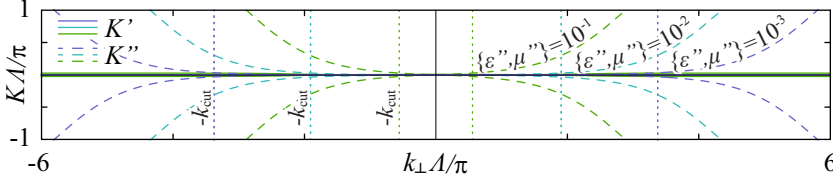


FIGURE 3.5: Real (solid) and imaginary (dashed) part of the exact TE- and TM-modes dispersion curves in periodic air-NIM media with $f_{\text{NIM}} = 0.5$ at the wavelength of $10 \mu\text{m}$. The period is 500 nm long and $\epsilon'_{\text{NIM}} = \mu'_{\text{NIM}} = -1$.

3.3.1 Dielectric-Lossy NIM Periodic Media

The lossless approach serves as an useful qualitative description of dielectric-NIM PLM dispersion curves. For an accurate characterization it is necessary to consider that realistic NIMs have losses. Moreover, these losses are of special relevance in the near infrared range and higher frequencies. In order to analyze the effect of losses the dispersion relations of periodic media composed of air and lossy NIM slabs are plotted in Fig. 3.5. The structural parameters of the PLM are $\Lambda = 500 \text{ nm}$ and $f_{\text{NIM}} = 0.5$. Besides, permittivities and permeabilities for the metamaterial are equal, $\epsilon_{\text{NIM}} = \mu_{\text{NIM}}$ at $\lambda_0 = 10 \mu\text{m}$. Their real parts are $\mu'_{\text{NIM}} = \epsilon'_{\text{NIM}} = -1$ while the imaginary parts take values from 10^{-1} to 10^{-3} . By simple inspection of Fig. 3.5 we observe that by increasing the imaginary part in the electromagnetic constants we reduce the propagating-waves bandwidth. Losses should decrease exponentially to obtain a linear improvement in the spatial resolution [123]. In the particular case that the perfect matching conditions are fully satisfied all the k_{\perp} will propagate without attenuation. However the imaginary part of ϵ_d and μ_d must be negative and this entails the use of an active medium. It should be feasible to use gain materials to compensate for the losses introduced by plasmonic nanostructures in NIMs. For example, we may combine

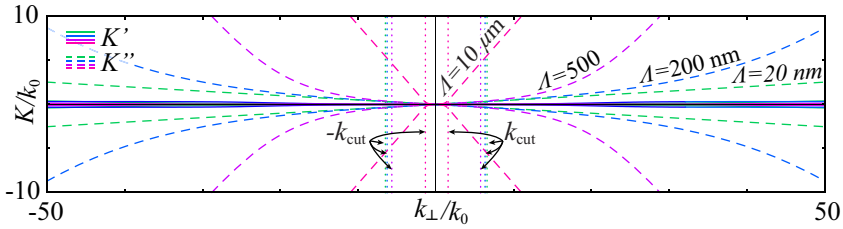


FIGURE 3.6: Exact TE- and TM-modes dispersion curves for a periodic air-NIM medium where air and NIM layers have the same width. The permeability and permittivity are set to $\epsilon_{\text{NIM}} = \mu_{\text{NIM}} = -1 + 0.1i$ at $\lambda_0 = 10 \mu\text{m}$. Real and imaginary part of K are plotted for different values of Λ .

metamaterials with electrically and optically pumped gain media such as semiconductor quantum dots [124], semiconductor quantum wells, and organic dyes [125] embedded into the metal nanostructures.

Finally, in Fig. 3.6 the consequences on changing the period, Λ , in lossy media have been evaluated. The Bloch modes are still transmitted without significant on-axis dephase (diffraction). We see that by decreasing Λ the number of transmitted frequencies limited by k_{cut} grows. This results as a consequence of the coupling of SWs in the air-NIM interfaces. The closer they get the more intense is the modal coupling.

3.4 Effective Media

We have analyzed metamaterials which consist of periodically distributed structured elements, whose size and spacing are much smaller than the wavelength of EM waves. As a result, the nanoscopic detail of each individual structure cannot be sensed by EM waves. What matters is the average result of the collective

response of the whole assembly. In other words, such a collection of inhomogeneous objects can be characterized by an equivalent homogeneous material with effective relative permittivity and permeability at the macroscopic level. The most attractive aspect of metamaterials is that effective permittivity and permeability can be controlled, using properly designed structures.

The effective medium approach, as Rytov exposed in his seminal paper [126], involves representing MD multilayered metamaterials as an uniaxial plasmonic crystal, whose optical axis is normal to the layers. Under this condition, the periodic lattice behaves as an uniaxial crystal characterized by the permittivity and permeability tensors [127]

$$\bar{\bar{\epsilon}} = \begin{pmatrix} \epsilon_{\perp} & 0 & 0 \\ 0 & \epsilon_{\perp} & 0 \\ 0 & 0 & \epsilon_{\parallel} \end{pmatrix} \quad \text{and} \quad \bar{\bar{\mu}} = \begin{pmatrix} \mu_{\perp} & 0 & 0 \\ 0 & \mu_{\perp} & 0 \\ 0 & 0 & \mu_{\parallel} \end{pmatrix}, \quad (3.12)$$

being ϵ_{\perp} and μ_{\perp} the effective optical constants in the direction perpendicular to the periodicity. Additionally ϵ_{\parallel} and μ_{\parallel} are the effective optical constants in the direction of the periodicity. The dispersion equation within the EMA for TE modes is

$$\frac{k_z^2}{\epsilon_{\perp}\mu_{\perp}} + \frac{k_{\perp}^2}{\epsilon_{\perp}\mu_{\parallel}} = k_0^2. \quad (3.13)$$

Similarly, the dispersion equation for TM-modes is

$$\frac{k_z^2}{\epsilon_{\perp}\mu_{\perp}} + \frac{k_{\perp}^2}{\epsilon_{\parallel}\mu_{\perp}} = k_0^2. \quad (3.14)$$

Provided that $\bar{\bar{\mu}}$ were a constant, TE- and TM-modes correspond to the well-known ordinary and extraordinary waves respectively. Equations (3.13) and (3.14) are obtained from Eq. (3.9) in the limit that the period Λ tends to zero. As can be

easily seen, Eq. (3.9) is periodic in k_z , while Eqs. (3.13) and (3.14) for the EMA are not. To avoid this, k_z in (3.13) and (3.14) can be replaced by $(2/\Lambda)\sin(k_\perp\Lambda/2)$ to obtain the quasi-effective medium approximation (QEMA) [128].

The permittivity and the permeability along the optical axis are given by

$$\epsilon_{\parallel} = \Lambda \left(\frac{w_1}{\epsilon_1} + \frac{w_2}{\epsilon_2} \right)^{-1}, \quad (3.15a)$$

$$\mu_{\parallel} = \Lambda \left(\frac{w_1}{\mu_1} + \frac{w_2}{\mu_2} \right)^{-1}. \quad (3.15b)$$

Complementarity to this,

$$\epsilon_{\perp} = \frac{w_1\epsilon_1 + w_2\epsilon_2}{\Lambda}, \quad (3.16a)$$

$$\mu_{\perp} = \frac{w_1\mu_1 + w_2\mu_2}{\Lambda}, \quad (3.16b)$$

corresponding to the permittivity and permeability in the transversal direction.

Dispersion relations (3.13) and (3.14) can be applied to the perfect matching conditions: $\epsilon_1 = -\epsilon_2$, $\mu_1 = -\mu_2$, and $f_m = 0.5$. Under these conditions we need to take into account that $\mu_{\perp}/\mu_{\parallel} = 0$ same as $\epsilon_{\perp}/\epsilon_{\parallel} = 0$. As a result K is 0 for all the values of k_{\perp} at both polarizations. This is an ideal configuration for diffraction-free beam propagation.

The agreement between the EMA and the exact Bloch dispersion curves depends on Λ/λ ratio. The TE and TM dispersion curves given in Eq. (3.13) and (3.14) within the EMA, and the Bloch dispersion curves derived from Eqs. (3.9) are plotted in Fig. 3.7 for periodic structures containing SrTiO₃-lossless metal and GaP-lossless metal. Exact dispersion equations are plotted with different Λ for TE and TM polarization in Figs. 3.7(a) and (b). For high values of Λ the shape

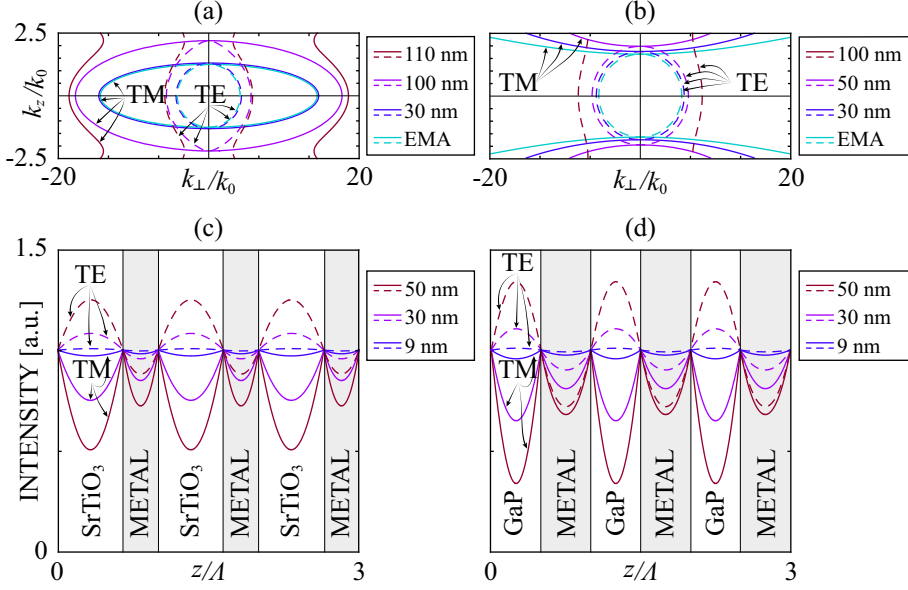


FIGURE 3.7: Exact PLM dispersion curves and EMA for TE-polarized waves (solid line) and TM-polarized waves (dashed line) in (a) and (b) at different Λ listed in the legend. In (c) and (d) the TM field intensity (line) and the TE field intensity (dashed) propagating in periodic media at different Λ and $k_{\perp} = k_0$ are plotted. The metal permittivity is set to $\epsilon_m = -7.754$ at a wavelength $\lambda_0 = 485$ nm. SrTiO₃ is set as the dielectric in (a) and (c) with $f_m = 0.35$ and $\epsilon_d = 6.596$. In (b) and (d) we take GaP with $\epsilon_d = 13.287$ for the dielectric and the filling factor is set to 0.50.

of the EMA curves does not fit with the Bloch dispersion equations. However, it is obvious that the contour lines from Bloch TE- and TM-modes reach a limiting shape that match the EMA contour lines by reducing Λ . Consequently the EMA is able to characterize the contour lines of a periodic structure when the thickness of the periods is small enough, roughly about $\lambda_0/10$. Additionally, it should be emphasized that the EMA TE-polarized dispersion curves have a circular shape and the TM-polarized curves may be either hyperbolic, as in Fig. 3.7(a), or elliptic like in Fig. 3.7(b).

There exists the second TM-band out of range in Figs. 3.7(a) and (b). Thus, in a

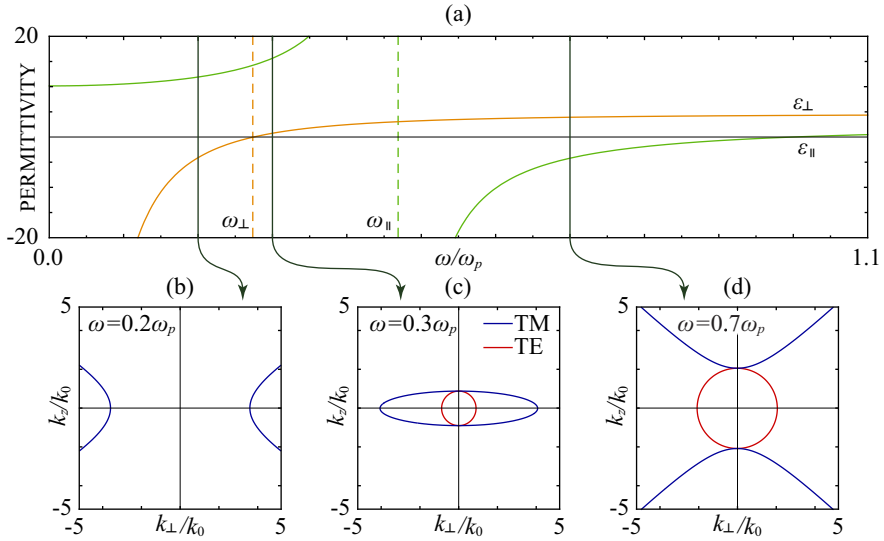


FIGURE 3.8: (a) Effective permittivities ϵ_{\perp} and ϵ_{\parallel} of 1D periodic media composed by a dielectric and a lossless Drude metal. The permittivity of the dielectric (SrTiO_3) is $\epsilon_d = 6.596$ and the metal filling factor is $f_m = 0.35$. EMA dispersion curves for TM- and TE-modes using material parameters from subfigure (a) and different frequencies are plotted in subfigures (b)-(d).

metal-dielectric superlattice we have two extraordinary TM-polarized modes and the ordinary TE-polarized mode.

Photonic layered media under the EMA has the properties of homogeneous and anisotropic media. In this kind of media the Bloch waves propagate with constant intensity as a consequence of the absence of non local effects. In the Figs. 3.7(c) and (d) the TM magnetic field and the TE electric field intensity normalized to their intensities at $z = 0$ are plotted. As Λ gets smaller the dependence of the field with z disappears and the wave intensity becomes constant. This effect does not depend either on the material permittivities, or on the polarization.

3.4.1 Hyperbolic Metamaterials

EMA is used to approach the PLM as an effective uniaxial anisotropic medium. The anisotropy of the resulting effective media is modulated not only by the filling factor of the metal but also by its strong dispersive character [55]. In Fig. 3.8(a) we represent the permittivities ϵ_{\parallel} and ϵ_{\perp} of the plasmonic crystal shown in Fig. 3.1 for a wide range of frequencies. There are two noteworthy frequencies in the plot. The lower one,

$$\omega_{\perp} = [1 + \epsilon_d(1 - f_m)/f_m]^{-1/2} \omega_p, \quad (3.17)$$

sets the point in which $\epsilon_{\perp} = 0$ while the highest one,

$$\omega_{\parallel} = [1 + \epsilon_d f_m / (1 - f_m)]^{-1/2} \omega_p, \quad (3.18)$$

sets the point in which ϵ_{\parallel} diverges and change its sign. In Fig. 3.8 $\omega_{\perp} = 0.274\omega_p$ and $\omega_{\parallel} = 0.469\omega_p$. Also, for frequencies far under the plasma frequency, $\omega \ll \omega_p$, we come near the following expressions: $\epsilon_{\perp} \approx f_m \epsilon_m$ and $\epsilon_{\parallel} \approx \epsilon_d / (1 - f_m)$. It is noteworthy that $\omega_{\perp} < \omega_{\parallel}$ if $f_m < 0.50$, however, if $f_m > 0.50$ it may be just the opposite.

The TE-modes contour lines are plotted in Figs. 3.8(b)-(d) by using Eq. (3.13) for nonmagnetic materials ($\mu_{\perp} = \mu_{\parallel} = 1$), that is

$$k_z^2 + k_{\perp}^2 = k_0^2 \epsilon_{\perp}. \quad (3.19)$$

This is the equation of a circumference with radius $k_0 \sqrt{\epsilon_{\perp}}$. Hence, TE-modes dispersion equation within the EMA is equivalent to that of a dielectric with permittivity ϵ_{\perp} . It clear in Fig. 3.8(a) that for frequencies lower than ω_{\perp} the effective

permittivity $\epsilon_{\perp} < 0$. The latter condition prevents propagating TE-modes to exist in effective media since they behave like a metal.

Equivalently TM-modes in the EMA for nonmagnetic materials can be deduced from Eq. (3.14),

$$\frac{k_z^2}{\epsilon_{\perp}} + \frac{k_{\perp}^2}{\epsilon_{\parallel}} = k_0^2. \quad (3.20)$$

The latter equation predicts different kinds of spatial dispersion depending on the sign of ϵ_{\perp} and ϵ_{\parallel} . A hyperbolic dispersion illustrated in Fig. 3.8(b) exists up to a frequency ω_{\perp} . It is noteworthy that Bloch waves having low spatial frequencies k_{\perp} cannot propagate in the medium. Only at k_{\perp} higher than $k_0\sqrt{\epsilon_{\parallel}}$ we can find real solutions in the dispersion curves. From ω_{\perp} to ω_{\parallel} both ϵ_{\parallel} and ϵ_{\perp} are positive. The contour line given by Eq. (3.20) becomes an ellipse centered in the origin as can be seen in Fig. 3.8(c). The semi-axis, $k_0\sqrt{\epsilon_{\perp}}$, is thinner than the semi-axis $k_0\sqrt{\epsilon_{\parallel}}$. Furthermore, by increasing the frequency ω the ellipse stretches along the k_{\perp} axis. Nearby the limit case when $\omega = \omega_{\parallel}$, the ellipse becomes almost a straight line. This is the canalization regimen behavior [56] that allows the transmission of a wide number of frequencies without diffraction. In the range $\omega_{\parallel} < \omega < \omega_p$, dispersion curves turn to a hyperbola centered at $k_{\perp} = 0$ as can be seen in Fig. 3.8(d). Finally, at frequencies beyond ω_p , the TM-modes dispersion curve turns again into an ellipse. The main difference with the elliptic dispersion curves in the range $\omega_{\perp} < \omega < \omega_{\parallel}$ is that now $\epsilon_{\perp} > \epsilon_{\parallel}$, thus the ellipse is stretched in the k_z axis.

3.5 Dual Hyperbolic-Elliptic Media

A major problem in the description of the spatial dispersion curves for TM waves arises when the EMA provides positive values of ε_{\perp} and ε_{\parallel} leading Eq. (3.20) to an ellipsoidal shape. In this case the plasmonic band is completely missed. In order to recover it a simple curve-fitting method is proposed in Ref. [122, 129]. We will include in the curve fitting a set of data involving points from solutions of the exact dispersion equation (3.9) placed in the vicinity of the Brillouin boundaries, $k_z = (2m + 1)\pi/\Lambda$ where m is an integer. To find a formula that best fits this given set of data we propose a new off-center ellipsoid or revolution centered in $k_z = (2m + 1)\pi/\Lambda$ with semiaxis $k_0\sqrt{\tilde{\varepsilon}_{\parallel}}$ and $k_0\sqrt{\tilde{\varepsilon}_{\perp}}$,

$$\frac{k_{\perp}^2}{\tilde{\varepsilon}_{\parallel}} + \frac{[k_z - (2m + 1)\pi/\Lambda]^2}{\tilde{\varepsilon}_{\perp}} = k_0^2. \quad (3.21)$$

For convenience, the data set is better fitted to the Taylor expansion of Eq. (3.21) around $k_z = (2m + 1)\pi/\Lambda$. Up to a second order, we write $k_{\perp} = A - B[k_z - (2m + 1)\pi/\Lambda]^2$, where $A = k_0\sqrt{\tilde{\varepsilon}_{\parallel}}$ and $B = (2k_0\tilde{\varepsilon}_{\perp})^{-1}\sqrt{\tilde{\varepsilon}_{\parallel}}$. Once we determine A and B from the parabolic-curve fitting, we may derive the semi-axes.

Figure 3.9 shows the exact TM dispersion curves for lossless Ag-GaAs PLM with different w_d . We also include the ellipsoids derived from Eq. (3.21) after the corresponding curve fitting. The proposed ellipsoids provide accurate results except in the vicinities of $k_z = 0$ (more generally around $k_z = 2m\pi/\Lambda$). In this region, two neighboring ellipsoids cut at a certain value of k_{\perp} , what happens merely if $\sqrt{\tilde{\varepsilon}_{\perp}} > \pi/k_0\Lambda$. From physical fundamentals we expect that a bandgap emerges as a consequence of Bragg reflections. Note that Eq. (3.21) itself does not provide an accurate spatial dispersion near the bandgap but it reveals its presence in a simple

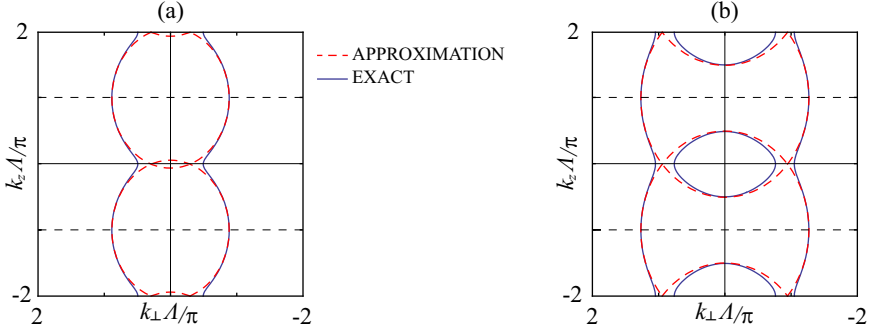


FIGURE 3.9: Equifrequency dispersion curves for an Ag-GaAs PLM at $\lambda_0 = 1.55 \mu\text{m}$. The refractive index of Ag is set to $\epsilon_m = -116$ and the GaAs permittivity is 12.4. Exact solutions from Eq. (3.9) are drawn in blue solid line, and the approximation followed from Eq. (3.21) in red dashed line. $w_m = 12 \text{ nm}$ while $w_d = 90 \text{ nm}$ in (a) and 150 nm in (b).

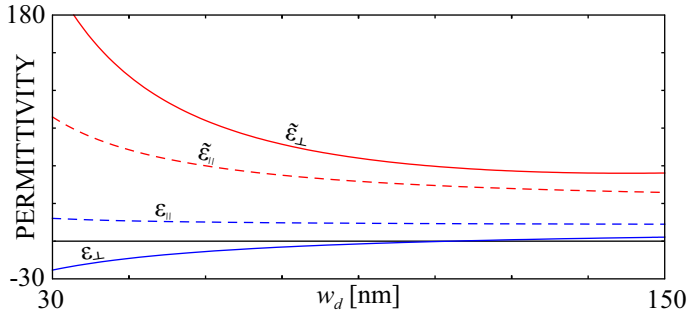


FIGURE 3.10: Estimations of $\tilde{\epsilon}_{\parallel}$ and $\tilde{\epsilon}_{\perp}$ from the curve-fitting method in a Ag-GaAs multilayer with $w_m = 12 \text{ nm}$ at $\lambda_0 = 1.55 \mu\text{m}$. We included the average permittivities predicted by the EMA.

way. In the case that two TM-mode allowed bands are present we estimate that $k_0\sqrt{\tilde{\epsilon}_{\perp}} = k_0\sqrt{\epsilon_{\perp}} + \pi/\Lambda$ provided $\epsilon_{\perp} > 0$. This equation may be rewritten as

$$\tilde{\epsilon}_{\perp} = \left(\sqrt{\epsilon_{\perp}} + \frac{\pi}{k_0\Lambda} \right)^2. \quad (3.22)$$

This equation can estimate analytically the value of $\tilde{\epsilon}_{\perp}$ instead of employing the proposed curve fitting.

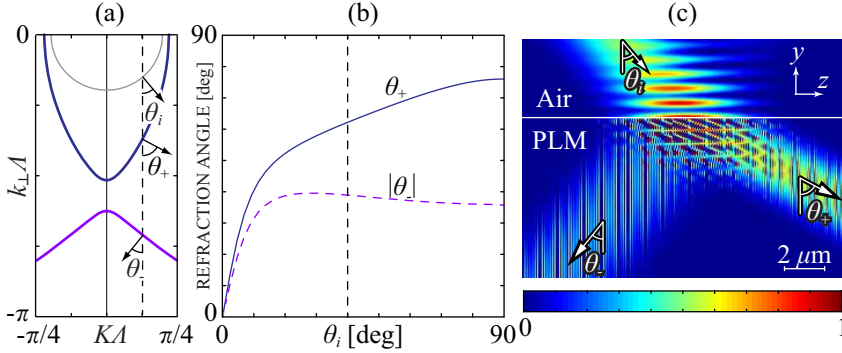


FIGURE 3.11: (a) Isofrequency curve at the wavelength $\lambda_0 = 1.129 \mu\text{m}$ for a PLM with Ag layers of $w_m = 10 \text{ nm}$ and GaAs layers of $w_d = 100 \text{ nm}$ (thick blue lines) and the vacuum (thin gray line). The permittivities of the dielectric and metal are $\epsilon_d = 6.2$ and $\epsilon_m = -57.8$ respectively. (b) Angles of refraction θ_+ (solid line) and θ_- (dashed line) in terms of the angle of incidence from the vacuum. (c) Numerical experiment of single-polarization double refraction in our metal-dielectric periodic medium.

In Fig. 3.10, we represent the values of $\tilde{\epsilon}_{\perp}$ and $\tilde{\epsilon}_{\parallel}$, which were calculated for a Ag-GaAs PLM of $w_m = 12 \text{ nm}$ at telecoms wavelength. These estimates are depicted together with ϵ_{\parallel} and ϵ_{\perp} EMA-based. Note that ϵ_{\parallel} and $\tilde{\epsilon}_{\perp}$ are positive parameters, despite the fact that ϵ_{\perp} changes their sign. Along with increasing values of w_d , both permittivities $\tilde{\epsilon}_{\parallel}$ and $\tilde{\epsilon}_{\perp}$ decrease. We point out that some plasmonic metamaterials are of the form such that the EMA estimates an hyperboloidal dispersion, specifically when $\epsilon_{\perp}/\epsilon_{\parallel} < 0$, in opposition of the ellipsoidal dispersion given by our approach.

3.6 Double Refraction Induced by Nonlocal Effects

As discussed above, the existence of two branches representing the solutions of Eq. (3.9) involves that harmonic excitations of a given K_i spatial frequency lead to propagation of twin beams inside the PLM. This phenomena has been shown

in [130]. Additionally, the same phenomena have been reported using graphene [131]. In Ref. [122, 132] the double refraction phenomenon in PLM is numerically simulated with a TM-mode analysis in COMSOL Multiphysics. In this section the simulations and further analysis with PLM are reviewed.

We consider a wave-field pattern of a spatial wave packet propagating in air at $\theta_i = 40$ deg with respect to the layers orientation and impinging in an Ag-TiO₂ PLM. In Fig. 3.11(a) its air and Ag-TiO₂ PLM isofrequency curves are plotted. We also plot $K_i = k_0 \sin \theta_i$ with a vertical dashed line. The propagation direction of the incident and scattered twin rays is indicated by arrows at the cutoff point between K_i and the isofrequency curves. Scattered twin rays propagate at an angle $\theta_+ = 62.2$ deg for positive refraction and $\theta_- = -38.9$ deg for negative refraction. The angles θ_{\pm} were evaluated from the normal vector of each one of the two branches appearing in the isofrequency curve, pointing the direction of power flow of the scattered fields under positive and negative refraction. In Fig. 3.11(b) we represent θ_+ and $|\theta_-|$ for different angles θ_i of incidence. As we observe, θ_+ increases for high θ_i and it is limited by 76.0 deg at grazing incidence. On the other hand, the $|\theta_-|$ curve reaches a plateau at $|\theta_-| = 35.9$ deg approximately, and does not increase any further at high θ_i as a consequence of the hyperbolic-like spatial dispersion of this second branch. Therefore negative refraction is related to canalization of subwavelength signals [55].

Figure. 3.11(c) plots the intensity $|H|^2$ of the TM wave field considering a wavelength of $\lambda_0 = 1.129\mu\text{m}$. In order to achieve an increased resolution, we first computed the spatial distribution of the incident beam and the scattered fields in the Fourier domain. We verify the values of θ_{\pm} as deduced from the isofrequency curve derived from Eq. (3.9) and plotted in Fig. 3.11(a), which are in excellent agreement with our numerical simulations shown in Fig. 3.11(c). The incident

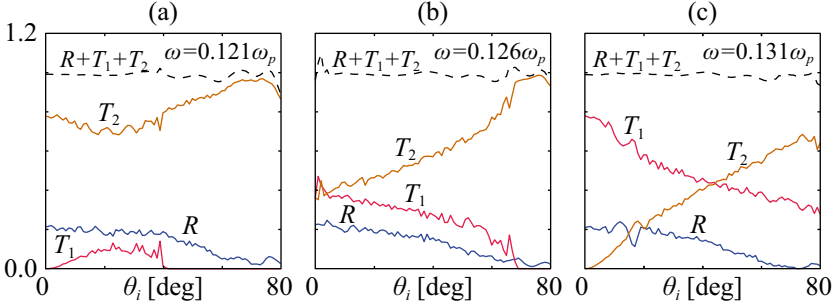


FIGURE 3.12: Transmittance distributed between the twin beams (T_1 and T_2) in our PLM for different frequencies around $\omega_{\perp} = 0.126 \omega_p$. Reflectance R is also included.

Gaussian beam has a waist (FWHM equal to $4\lambda_0$) placed close to the air-PLM interface.

Finally we evaluate the reflectance and the transmittance distributed between the twin beams in our air/PLM arrangement. To find out how much energy is reflected from the boundary and transmitted into the second medium, we need to consider the ratios of the Poynting power flow of the reflected and the transmitted waves to that of the incident wave. Since we are disregarding absorption inside the PLM, the power flow normal to the boundary surface is a constant throughout the medium. Thus we consider the normal component of the time-averaged Poynting's vectors of the incident, reflected and transmitted p -polarized waves. In numerical simulations using the TM-mode analysis in our finite-element method (FEM) software, we evaluate the magnetic field H_x in the optical arrangement; subsequently we will treat the field inside the PLM and in the vacuum independently.

In Fig. 3.12(a)-(c) we show transmittances T_1 and T_2 of the Bloch modes undergoing positive refraction and negative refraction, respectively, for different frequencies near $\omega_{\perp} = 0.126 \omega_p$ as derived from Eq. (3.17) and angles of incidence. We

include the reflectance R evaluated on air, which takes its highest values (around 0.2) at angles near $\theta_i = 0$. Note that $T_1 + T_2 + R$ yields the unity, apart from small deviations attributed to FEM-limited accuracy. In general, T_1 decreases as the angle θ_i increases, attaining a zero transmittance from its critical angle, which is equal to 41.1 deg in Fig. 3.12(a) and 68.4 deg in Fig. 3.12(b). In Fig. 3.12(c) no critical angle may be found. On the other hand, T_2 increases along with θ_i enhancing negative refraction. Moreover, negative refraction caused by hyperbolic dispersion is dominant at frequencies below ω_{\perp} and positive refraction attributed to elliptic dispersion is more vigorous above ω_{\perp} in clear agreement with the EMA. For high angles of incidence, however, this phenomenon may be reversed. As a simple demonstration, note that the equilibrium condition $T_1 = T_2$ is reached at an angle $\theta_i = 44.4$ deg in Fig. 3.12(c); for higher values of θ_i the beam with negative refraction carries the most power flux (along the y direction). As a conclusion, negative refraction plays an essential role in regimes of the EMA related to elliptic dispersion. We reported the results of this Section in Ref. [132].

Chapter 4

Image Formation Using NIMs

In this Chapter we will develop the concept of image formation with NIMs. We start from the simplest approach based on geometrical optics and move forward to the electromagnetic formulation. The fundamentals will be reviewed: transmission and reflection coefficients, transfer function, and point spread function (PSF). Particular attention should be paid to a 3D formulation of the PSF and its peculiarities in comparison with the most well-known 2D PSF, especially, in the depth of focus. We will also review the asymmetric superlenses as image forming system including an aberration analysis. In addition, we will evaluate the transmitted fields of a linear dipole through a NIM superlens for both TE and TM polarization. Finally we will analyze the effect of exfoliating a NIM superlens in multiple slabs by means of the PSF.

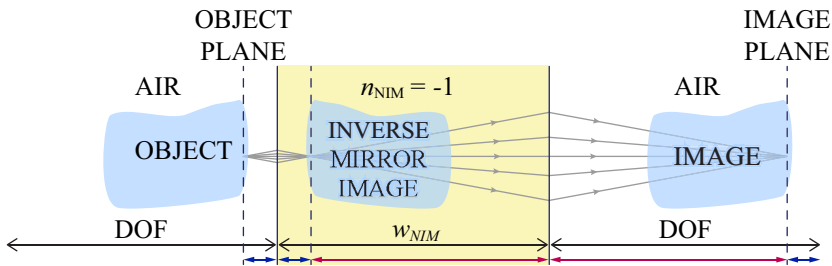


FIGURE 4.1: Veselago's lens schematic

4.1 Geometric Optics Approach

A new kind of flat lens with negative index of refraction was proposed by Veselago in 1968 [2]. Note that the Snell law is valid in this material. Therefore, a lens with a refractive index $n_{\text{NIM}} = -1$ surrounded by air will transform a diverging bundle of rays to a converging ray bundle, as shown in Fig. 4.1. A negative refractive index medium bends light to a negative angle relative to the surface normal. Light formerly diverging from a point source is set in reverse and converges stigmatically back to a point. Released from the medium the light reaches a focus for a second time. The image-forming system reproduces an inverse mirror image inside the NIM and a real image at the outer plane with lateral and axial magnification equal to 1. The distance from the object to the image is always twofold the NIM layer width, $2w_{\text{NIM}}$. Importantly, in the Veselago lenses the optical distance covered by the rays in the dielectric cancels the optical distance in the NIM and consequently the optical length is zero. Additionally, the depth of field (DOF) is equal to the width of the flat lens, w_{NIM} , being the DOF defined as the width of each of the two zones where we may encounter real conjugate pairs of objects and images, simultaneously.

Real NIMs have always losses that should be considered. They reduce the intensity transmission and modify the rays paths. Note that, NIMs are strongly dispersive and hence the superlens behavior of this kind of media is limited to a short bandwidth. From the point of view of the geometric optical approach the ray under grazing incidence gives maximum value for the wavenumber $k_{\perp} = k_0$. Spatial frequencies over this maximum value are not considered and consequently some purely electromagnetic properties of the NIM lenses are not taken into account in the geometrical approach.

4.2 Electromagnetic Formulation

The analysis of the NIM lensing performed by Veselago was conducted from the geometric point of view. In 2000 Pendry revealed in his seminar paper [3] that these NIM lenses can enhance evanescent waves which otherwise will rapidly decay in free-space propagation. The contribution of these waves allows to recover details from the image smaller than the wavelength in the object plane. Evanescent waves are enhanced due to the coupled SWs excited at the input and output interfaces of the NIM slab [5, 7, 133]. It is also remarkable that a phase reversal is accomplished for the homogeneous part of the field within the NIM, compensating the phase gathered by the wave when traveling away from the source. In principle, the image can recover all the Fourier frequencies provided that the perfect match condition are fulfilled. An unbounded range of evanescent-wave frequencies will contribute to the field intensity in the image plane. Consequently this kind of lenses are referred as perfect lenses [8]. Nonetheless, this ideal reconstruction of the object cannot be reached since the metamaterial always exhibits losses, leading to a cutoff frequency on the flat-lens transmittance. This is particularly true for

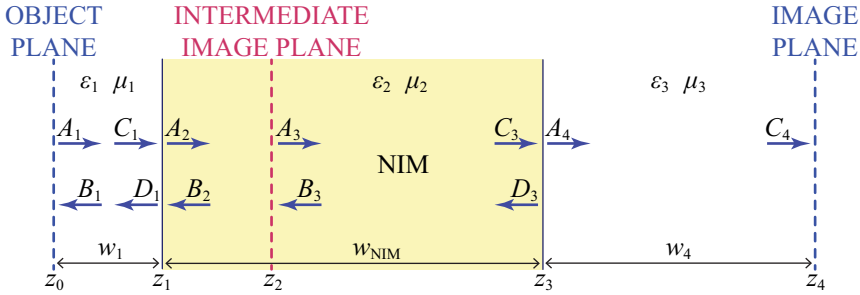


FIGURE 4.2: Schematic geometry of the planar perfect lens. Incident fields A_j , C_j and reflected fields B_j , D_j are plotted

the optical range. The contribution of μ'' to the metamaterial losses is especially significant at this range of frequencies. In spite of the fact that compensation of amplitudes results impossible in practice, superresolution can be achieved. In the past years, this attractive property combined with new improvements in nanofabrication have triggered the fabrication of NIMs [20, 28, 100, 134, 135]. Negative refraction and subwavelength imaging have been demonstrated at microwave [136], infrared [58, 137] and visible wavelengths [88].

It should be noted that extremely-high resolution could be obtained at the price of signal delay [138]. Only at the stationary solution the enhancement of the evanescent frequencies by means of the SW excitation and propagation is fully accomplished. The smaller details take the longer time to be developed. Therefore, an infinitely high resolution would need an infinitely long time for its realization.

Consider the flat lens from Fig. 4.2 where a NIM layer of width w_{NIM} is surrounded by dielectrics. The TE field in the object space $z < z_1$ is evaluated as the superposition of an incident wave field

$$\mathbf{E}_{\text{in}} = \iint \mathbf{A}(\mathbf{k}_{\perp}) \exp[i\mathbf{k}_{\perp} \mathbf{R} + ik_{z1}(z - z_0)] d^2\mathbf{k}_{\perp}, \quad (4.1)$$

and the reflected field

$$\mathbf{E}_r = \iint R_s(k_\perp) \mathbf{A}(\mathbf{k}_\perp) \exp[i\mathbf{k}_\perp \mathbf{R} - ik_{z1}(z - z_0)] d^2\mathbf{k}_\perp, \quad (4.2)$$

where $R_s = B_1/A_1$ stands for the s -polarized reflection coefficient at the object plane (see Fig. 4.2 and Appendix A for clarity). The propagation constant k_{zi} is given by

$$k_{zi} = \pm \sqrt{k_0^2 \mu_i \varepsilon_i - k_\perp^2}, \quad (4.3)$$

where the (+) sign goes for the dielectrics and the (-) goes for the NIM. The plane-wave representation of the wave field, the spatial spectrum

$$\mathbf{A}(\mathbf{k}_\perp) = \frac{1}{(2\pi)^2} \iint \mathbf{E}_{\text{in}}(\mathbf{R}_0, z_0) \exp(-i\mathbf{k}_\perp \mathbf{R}_0) d^2\mathbf{R}_0, \quad (4.4)$$

represents the 2D Fourier transform of the field propagating toward the superlens at the object plane z_0 , being $\mathbf{R}_0 = (x_0, y_0)$.

Inside the NIM slab ($z_1 < z < z_3$), the wave field is again a superposition of the propagating field

$$\mathbf{E}_{t13} = \iint T_{s13}(k_\perp) \mathbf{A}(\mathbf{k}_\perp) \exp[i\mathbf{k}_\perp \mathbf{R} + ik_{z2}(z - z_2)] d^2\mathbf{k}_\perp, \quad (4.5)$$

and the counterpropagating field

$$\mathbf{E}_{r13} = \iint R_{s13}(k_\perp) \mathbf{A}(\mathbf{k}_\perp) \exp[i\mathbf{k}_\perp \mathbf{R} - ik_{z2}(z - z_2)] d^2\mathbf{k}_\perp. \quad (4.6)$$

The ratios $R_{s13} = B_3/A_1$ and $T_{s13} = A_3/A_1$ represent the contributions of propagating and counterpropagating waves inside the NIM layer, and $z = z_2$ is the location

of the intermediate image plane. They can be deduced through the transfer matrix method shown in Appendix A. To evaluate A_3 and B_3 we solve the equations system

$$\begin{pmatrix} A_3 \\ B_3 \end{pmatrix} = \bar{\bar{M}}_{s34} \begin{pmatrix} C_4 \\ 0 \end{pmatrix}, \quad (4.7)$$

where the transfer matrix $\bar{\bar{M}}_{s34} = \bar{\bar{P}}_3 \bar{\bar{D}}_{s3}^{-1} \bar{\bar{D}}_{s4} \bar{\bar{P}}_4$ connects the amplitudes of the electric field at $z = z_2$ and with the image plane. The amplitude C_4 can be easily derived from the transmission coefficient, $T_s = C_4/A_1$, between the object plane z_0 and the image plane z_4 . It is also possible to derive the reflectance and transmittance by means of the Airy's formulae while in this Thesis we follow the transfer matrix formulation. In addition, is straightforward to deduce p -polarized waves reflection coefficient that applies directly to the transverse magnetic field as given from the duality theorem (A.1).

Finally, the field emerging from the imaging system at $z > z_3$ is determined by means of the equation

$$\mathbf{E}_{\text{out}} = \iint T_s(k_{\perp}) \mathbf{A}(\mathbf{k}_{\perp}) \exp[i\mathbf{k}_{\perp} \mathbf{R} + ik_{z3}(z - z_4)] d^2 \mathbf{k}_{\perp}. \quad (4.8)$$

The analysis given above is fully consistent with Maxwell's equations. It is straightforward to verify that inserting Eq. (4.4) into Eq. (4.8) leads to the 2D convolution,

$$\mathbf{E}_{\text{out}}(\mathbf{R}, z) = \iint \mathbf{E}_{\text{in}}(\mathbf{R}_0, z_0) h_3(\mathbf{R} - \mathbf{R}_0, z - z_4) d^2 \mathbf{R}_0. \quad (4.9)$$

We recognize the 3D function

$$h_3(\mathbf{R}, z) = \frac{1}{(2\pi)^2} \iint T_s(k_\perp) \exp(i\mathbf{k}_\perp \mathbf{R} + ik_{z3}z) d^2\mathbf{k}_\perp, \quad (4.10)$$

as the 3D PSF of the optical system. It is noteworthy to mention that a planar perfect lens is a linear and 3D shift-invariant system as we can derive from Eq. (4.9). We can use the duality theorem (A.1) to deduce equivalent equations for the TM-modes magnetic field.

4.3 3D Point Spread Function

In this Section we will review the 3D PSF and the generalized amplitude transfer function (ATF). The results of this Section can be found in Refs. [139, 140]. Provided that the NIM is characterized by $\epsilon_2 = \mu_2 = -1$, that is disregarding material losses, and the superlens is immersed in vacuum, $T = 1$ yielding $h_3(\mathbf{R}, 0) = \delta_2(\mathbf{R})$. In this limit case [3], the presence of the 2D Dirac delta function δ_2 leads to a perfect image

$$\mathbf{E}_{\text{out}}(\mathbf{R}, z_4) = \mathbf{E}_{\text{in}}(\mathbf{R}, z_0). \quad (4.11)$$

However, $h_3(\mathbf{R}, z)$ would exhibit a singular behavior in $z < 0$. From the Weyl's representation of the scalar Green's function, one may derive that [141]

$$h_3(\mathbf{R}, z < 0) = \frac{1}{2\pi} \frac{\partial}{\partial z} \left[\frac{\exp(-ik_0 r)}{r} \right], \quad (4.12a)$$

$$h_3(\mathbf{R}, z > 0) = -\frac{1}{2\pi} \frac{\partial}{\partial z} \left[\frac{\exp(ik_0 r)}{r} \right], \quad (4.12b)$$

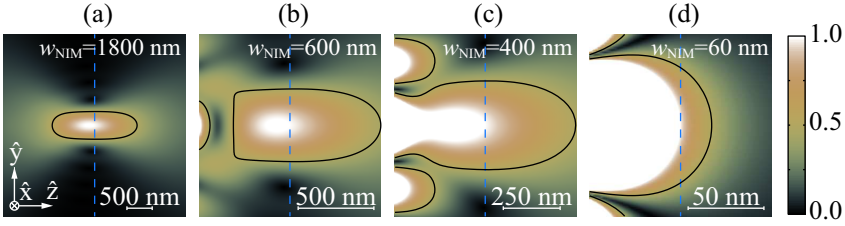


FIGURE 4.3: Absolute value of the 3D PSF for a NIM slab surrounded by air. At $\lambda_0 = 600$ nm the NIM optical parameters are $\epsilon_2 = \mu_2 = 1 + 0.1i$. The size of the NIM slab is 1800 nm in (a), 600 nm in (b), 400 nm in (c), and 60 nm in (d). Plots are normalized to unity at $r = 0$, and contour lines for a value 1/2 (solid line) are drawn in black. The image plane is displayed with a vertical dashed line.

where the distance from the observation point, $\mathbf{r} = (R, z)$, to the focal point located at the origin is $r = |\mathbf{r}|$. We will see that the imaginary part of the refractive index regularizes the out-of-focus field distribution given in Eq. (4.12a).

Let us illustrate the image formation process in the superlens depicted in Fig. 4.2 considering losses. We further assume a slab of NIM surrounded by air and set $\lambda_0 = 600$ nm. The optical constants $\epsilon_2 = \mu_2 = -1 + i\delta$, being $\delta = 0.1$. Under these circumstances, a perfect imaging cannot be achieved, however a good replica may be found at the plane z_4 since $\delta \ll 1$.

The amplitude of the 3D PSF $|h_3|$ is depicted in Fig. 4.3 for slabs of different widths, w_{NIM} . There is an unique PSF for both polarizations provided that $\epsilon_2 = \mu_2$. Since T is radially symmetric, the 3D PSF varies upon the axial coordinate, z , and the modulus of the transverse vector, R , as

$$h_3(R, z) = \frac{1}{2\pi} \int_0^\infty T(k_\perp) J_0(k_\perp R) \exp(ik_{z3}z) k_\perp dk_\perp, \quad (4.13)$$

where J_0 is a Bessel function of the first kind.

Shifting the image plane at $z = 0$, the exit surface of the layered lens would be found at $z = z_3 - z_4 = w_1 - w_{\text{NIM}}$. Bearing in mind that $w_1 \geq 0$, the meaningful part of the PSF lies within the range $z \geq -w_{\text{NIM}}$ as considered in the graphical representation. The 3D amplitude distribution of the PSF for a subwavelength width w_{NIM} shows a distinct behavior in comparison with those impulse responses for $w_{\text{NIM}} \gg \lambda_0$. For instance, the FWHM of the PSF at the image plane $\Delta_{\perp} = 73.5$ nm is clearly subwavelength if $w_{\text{NIM}} = 60$ nm; in fact, Δ_{\perp} would vanish if w_{NIM} were identically zero. Moreover, the amplitude reaches a maximum value at the center point $R = 0$ on the output plane, $z = z_3 - z_4$. The response of the optical system points to that for near-field imaging. On the contrary, $\Delta_{\perp} = 552$ nm comes near the wavelength at $w_{\text{NIM}} = 1.8 \mu\text{m}$. Here, the maximum amplitude is found approaching the image plane far from the output plane, existing in a small longitudinal shift of 104 nm. Furthermore, one may determine a FWHM along the z axis, and in our case we found $\Delta_z = 1.70 \mu\text{m}$.

4.3.1 Far-Field Term and Near-Field Term

The 3D PSF given in Eqs. (4.10) and (4.13) can be splitted in its near field term h_N and the far field term h_F ,

$$h_3(\mathbf{R}, z) = h_N(\mathbf{R}, z) + h_F(\mathbf{R}, z). \quad (4.14)$$

The far field term may be represented as follows [142]:

$$h_F(\mathbf{R}, z) = \frac{-ik_0}{2\pi} \iint a(\hat{\mathbf{s}}) \exp(ik_0 \hat{\mathbf{s}} \cdot \mathbf{r}) d\Omega. \quad (4.15)$$

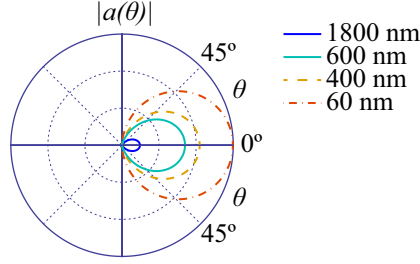


FIGURE 4.4: Absolute value of the angular spectrum in the semispace $z > 0$ associated with the 3D PSF for the superlenses analyzed in Fig. 4.3.

Thus, h_F is evaluated from Eq. (4.10) within the far field spectral domain, $0 \leq \theta \leq \pi/2$, being $d\Omega = \sin\theta d\theta d\phi$ the element of solid angle in spherical coordinates. In Eq. (4.15) the 3D unitary vector $\hat{\mathbf{s}} = \mathbf{s}_\perp + s_z \hat{z}$ is deduced from the dispersion equation

$$k_0 \hat{\mathbf{s}} = \mathbf{k}_\perp + k_{z1} \hat{z}. \quad (4.16)$$

Finally, the angular spectrum is

$$a(\hat{\mathbf{s}}) = \frac{i}{\lambda_0} T(\mathbf{k}_\perp) s_z, \quad (4.17)$$

where $s_z = \cos\theta$. Since $k_\perp = k_0 \sin\theta$, the transmittance, T , depends exclusively upon the azimuthal coordinate, θ , and so does the angular spectrum $a(s)$.

The radiation intensity of a point source is in direct proportion with the squared absolute value of $|a(\theta)|^2$. The magnitude of the angular spectrum $|a|$ in the semispace $z > 0$ ($\theta < \pi/2$) is plotted in Fig. 4.4 for the NIM lenses from Fig. 4.3. The material absorption attenuates the radiation intensity. Thus, higher values of w_{NIM} implies smaller $|a(\theta)|$. However, the normalized radiation pattern is quite similar in all cases.

To gain a deep insight into the term h_F of the 3D PSF, let us consider the limit

case $\delta \rightarrow 0$. In this case, $T = 1$ and the transverse distribution of the PSF is an Airy disk,

$$h_F(\mathbf{R}, 0) = \frac{J_1(k_0 R)}{\lambda_0 R}, \quad (4.18)$$

where J_1 is a Bessel function of the first kind. Along the axis $R = 0$, the far-field 3D PSF may be expressed analytically as

$$h_F(0, z) = \frac{(1 - ik_0 z) \exp(ik_0 z) - 1}{2\pi z^2}. \quad (4.19)$$

This function is well-behaved in $z < 0$ so that, as expected, we encounter a singular response in the near-field term of the PSF. It is important to remark that $|h_F|$ in Eqs. (4.18) and (4.19) is maximum at the origin, whose central lobe has the FWHMs $\Delta_\perp = 0.705\lambda_0$ and $\Delta_z = 1.55\lambda_0$, respectively. At $\lambda_0 = 600$ nm, we have $\Delta_\perp = 423$ nm and $\Delta_z = 929$ nm. These numbers are roughly in agreement with the numerical simulation performed in Fig. 4.3(a) for $w_{\text{NIM}} = 1.8 \mu\text{m}$ revealing that h_F is the dominant part of the 3D PSF in this case. This is also true for higher values of w_{NIM} . Otherwise, the near-field component becomes significant (see Figs. 4.3(b)-(c) for $w_{\text{NIM}} = 600$ and 400 nm), and even takes the control of the amplitude distribution in the image volume for slabs of a subwavelength width, as shown in Fig. 4.3(d).

We point out that h_F given in Eq. (4.15) represents a focused wave with focus at the origin $r = 0$ and, as a consequence, it may follow the standard mathematical treatment of apertured spherical beams. In the limiting case $\delta = 0$, it yields an aberration-free focal wave, since $a(\hat{\mathbf{s}})$ is a real function excepting a constant complex factor; otherwise, monochromatic aberrations arise [141, 143].

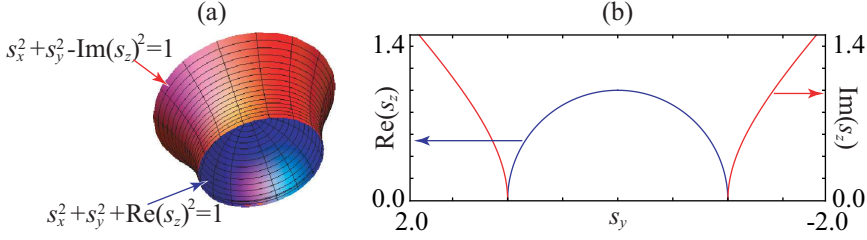


FIGURE 4.5: Spherical and hyperboloidal sheets constituting the generalized ATF are shown (a) in 3D and (b) on the meridional plane $s_x = 0$.

4.3.2 Generalized Amplitude Transfer Function

From Eq. (4.15), we infer that h_F may be written in terms of a 3D Fourier transform of the function $a(\hat{\mathbf{s}})$, which has extent in three dimensions and is wrapped around the unit hemisphere

$$\hat{\mathbf{s}} \cdot \hat{\mathbf{s}} = 1, \quad (4.20)$$

and $s_z \geq 0$ (see Fig. 4.5). In McCutchen's original paper [144], the function a is coined the *generalized aperture*, describing the patch of solid angle occupied by the Huygenian source at the aperture plane of the converging wave. In our case, however, the field amplitude is determined by the function T rather than the opacity on the exit pupil plane. Therefore, $a(\hat{\mathbf{s}})$ is simply recalled as the generalized ATF of the NIM planar lens.

The near-field component of the wave field, h_N might be expressed in the form of Eq. (4.15) if the angular coordinate θ is represented in the complex plane. Setting

$$\theta = \pi/2 - i\alpha \quad (4.21)$$

and running the real parameter α from 0 to ∞ allows us to consider the normalized wave vector $\hat{\mathbf{s}}$ with real transverse component of modulus $s_\perp = \cosh \alpha > 1$ and

the purely imaginary axial component $s_z = i \sinh \alpha$. The dispersion equation is conveniently rewritten as $s_{\perp}^2 - \text{Im}(s_z)^2 = 1$, representing a unit hyperboloid shown in Fig. 4.5. It is immediately derived that the angular spectrum $a(\hat{\mathbf{s}})$ wrapped around the hyperboloid surface constitutes the second sheet of the generalized ATF associated with evanescent components of the wave field.

Following the reasoning given above, it is concluded that the 3D PSF h_3 is fully computed by means of the 3D Fourier transform

$$h_F(\mathbf{r}) = \frac{-ik_0}{2\pi} \iint a(\hat{\mathbf{s}}) \exp(ik_0 \hat{\mathbf{s}} \cdot \mathbf{r}) d^3 \hat{\mathbf{s}}, \quad (4.22)$$

provided that the generalized ATF $a(\hat{\mathbf{s}}) \equiv a(\hat{\mathbf{s}}) \delta_1(s - 1)$, and provided the real part and the imaginary part of $\hat{\mathbf{s}}$ are nonnegative. Here, δ_1 is the Dirac delta function.

Previously, we mentioned that the 3D PSF h_3 is a singular function if the meta-material lens is lossless, assuming that the absolute value of its negative refractive index perfectly matched with that of the environment media. Such a singular behavior might be inferred now by considering the near-field term of the 3D ATF. The function $a(\hat{\mathbf{s}})$ modulates the ATF over the hyperbolic sheet. If $\delta \neq 0$, then $a(\hat{\mathbf{s}})$ is effectively bounded, which leads to a 3D ATF representing an open surface of a finite area. Neglecting dissipation, however, a becomes unbounded, thus providing in the spectral domain a hyperboloid of infinite extent.

As shown in Fig. 4.6, the modulus $|a|$ is maximum at $\theta = 0$ for the far field term, approaching $\lambda_0^{-1} \exp(-k_0 \delta w_{\text{NIM}})$, and it decreases to zero at $\theta = \pi/2$. Within the near-field regime, $|a|$ grows exponentially at increasing values of α , however, attaining a local maximum $|a|_{\text{max}}$ before it decreases for $\alpha \rightarrow \infty$. For $w_{\text{NIM}} = 60$ nm, the maximum $|a|_{\text{max}} = 4.77 \mu\text{m}^{-1}$ at $\alpha_{\text{max}} = 2.02$ rad, which corresponds to a normalized spatial frequency $s_{\perp} = 3.82$ (and $s_z = 3.69i$). On the far field sheet, the

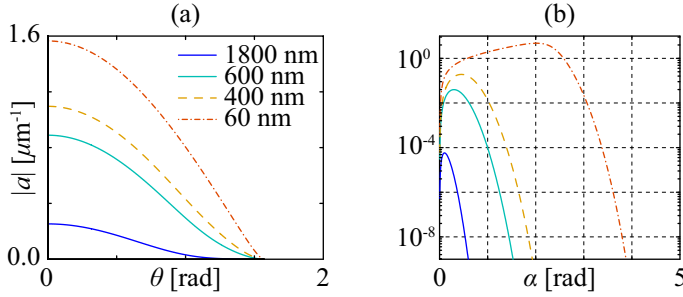


FIGURE 4.6: Absolute value of the angular spectrum $|a|$ for the numerical simulations of Fig. 4.3. The component of the far field is represented in the subfigure (a) and the near-field term of the ATF is shown in (b).

generalized ATF remains comparatively low, since $|a| \leq 1.57 \mu\text{m}^{-1} = |a(\theta = 0)|$. The effective area of the hyperbolical surface, where $a(\hat{\mathbf{s}})$ takes significant values, also surpasses in several units that from the unit hemisphere. On the other hand, for $w_{\text{NIM}} = 1.8 \mu\text{m}$, $|a|_{\text{max}} = 5.7610^{-5} \mu\text{m}^{-1}$ at $\alpha_{\text{max}} = 0.104$ rad, associated with a unit vector of $s_{\perp} = 1.005$ (and $s_z = 0.104i$). This is several orders of magnitude lower than the maximum $|a| = 0.253 \mu\text{m}^{-1}$ given at $\theta = 0$. Clearly, the effective area of $a(\hat{\mathbf{s}})$ on the hyperboloid is here a fraction of that from the hemisphere.

We conclude that the generalized ATF provides geometric and analytic arguments in order to derive critically whether h_N represents the dominant contribution to the 3D PSF. This is of relevance, since the subwavelength resolution is achieved exclusively in such a case.

4.3.3 Out-of-Focus Response

For microscopy applications, an extended object should be confined in the vicinities of the NIM slab in order to give rise to real images. A quasi-planar source with grooves and small surface defects contains some depth information that might be

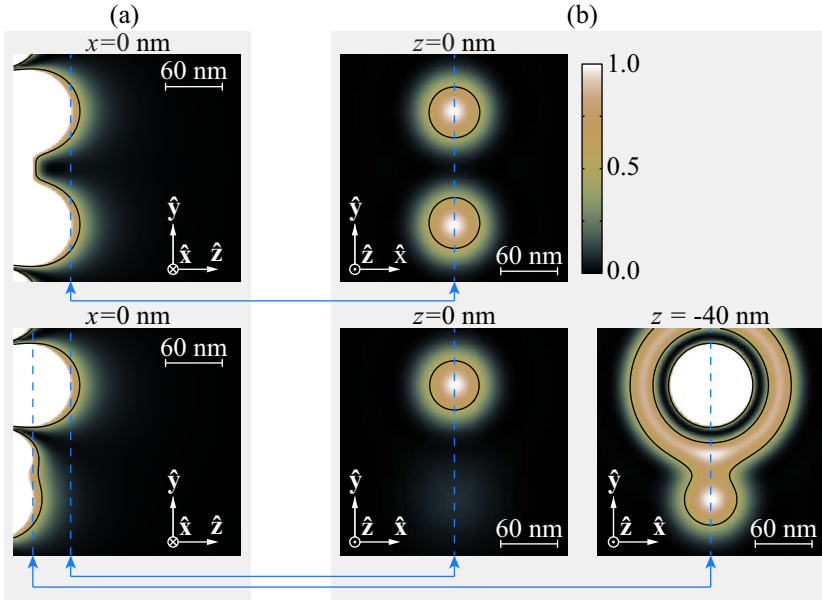


FIGURE 4.7: Intensity of the wave field in the image volume of two point sources centered at $\mathbf{R}_1 = -\mathbf{R}_2 = 60 \hat{y}$ nm provided under different conditions of depth: (a) both sources are located in the same transverse plane and (b) one source is 40 nm closer to the lens. The layer width is $w_{\text{NIM}} = 60$ nm and material absorption is $\delta = 0.1$.

transmitted through the lens. This issue is not evident, however, since the decay of the wave field from the output plane of the lens leads to inability for producing 3D focusing of energy in spots smaller than λ_0 [145].

Let us analyze the situation with multiple localized emitters when they are not found necessarily in the same transverse plane. Therefore, they should be placed in planes very close among themselves. In order to determine the limit of resolution with multiple localized emitters making use of the PSF we may find diverse criteria. Perhaps the most known criterion was introduced by Lord Rayleigh [146], which establishes that two point objects are resolved if the maximum in the diffraction pattern excited by one source lies at least on the first dark ring of the diffraction pattern generated by the second source.

Note that for a diffraction pattern in the form of an Airy disk, the limit of resolution coincides with 1.18 times the FWHM of the central peak in intensity. We consider a similar criterion. Specifically we simply consider the FWHM of the PSF as the limit of resolution of the image-forming system.

As illustration, we show in Fig. 4.7 the contour plot of the field intensity in the image space of the near-field superlens analyzed in Fig. 4.3(d) as it is produced by two equienergetic point sources. An incoherent superposition is assumed to get rid of interference phenomena. Therefore, the intensity distribution is proportional to

$$\sum_{j=1,2} |h_3(\mathbf{R} - \mathbf{R}'_j, z - z'_j)|^2. \quad (4.23)$$

This is consistent, for instance, with fluorescence microscopy under the first Born approximation [147]. Nevertheless, the output intensity of any point-like source as an electric dipole antenna might be computed straightforwardly by inserting the appropriate field \mathbf{E}_{in} rather than the Dirac delta function into Eq. (4.9). Both points are separated $|R'_1 - R'_2| = 120$ nm along the transverse direction. We analyze the case that one of these objects O_1 stays closer to the lens than O_2 , and therefore its image O'_1 remains in a plane (here $z'_1 = 0$) farther from the lens back face. In this plane, the presence of the second image O'_2 is imperceptible in virtue of the evanescent nature of its wave field. Moving to the geometric image plane of O'_2 ($z'_2 = -40$ nm), it is clearly detected, however, superposed to the strong back tail produced by O'_1 .

In the case analyzed previously, out-of-focus side-lobes of the PSF attain a considerable strength leading to a fast image blurring and loss in resolution power. Following the half-maximum dashed line of the image intensity of O'_2 at its geometric image plane $z = z'_2$ shown in Fig. 4.7, it also embodies the diffraction spot

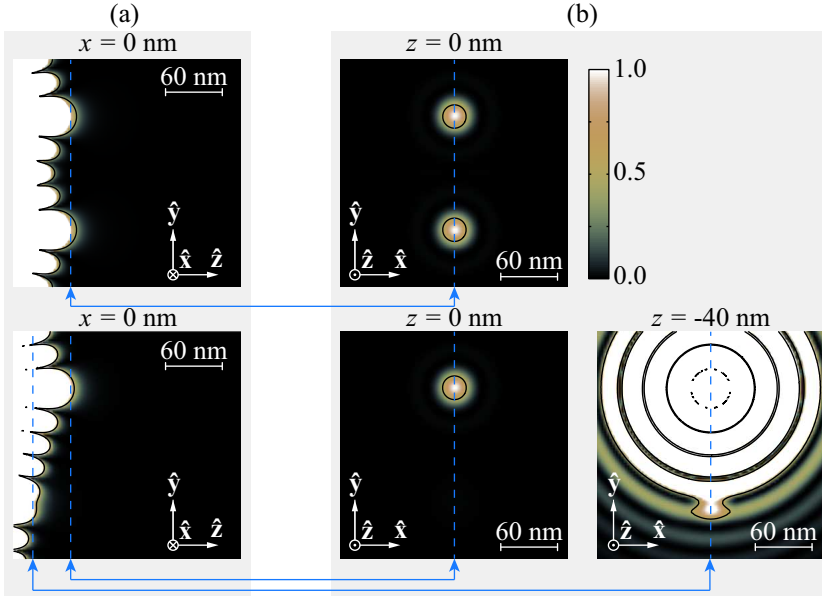


FIGURE 4.8: Same as in Fig. 4.7 for $\delta = 0.001$.

of O'_1 and, as a consequence, one may consider that both image points are not resolved. In order to increase the transverse resolution of the system, we consider its response for a more favorable value of the absorption parameter, $\delta = 10^{-2}$. Here, the half-maximum closed lines are separately associated with each impulse response of the two point sources. This superresolution mechanism relies exclusively on a decrement of the FWHM of the in-focus PSF of O'_2 . In fact, the out-of-focus PSF of O'_1 has a larger FWHM.

From the discussion given above, one may infer that improving the resolution power of near-field NIM lenses is achieved at the cost of a fast image degradation in out-of-focus planes. Let us deeply examine this assessment with the help of Fig. 4.8. For an extremely low absorbing layer with parameter $\delta = 10^{-3}$, the lowest limit of resolution along the transverse direction (in-focus FWHM) is achieved in comparison with Fig. 4.7. Nevertheless, its back tail at $z < 0$ spreads much

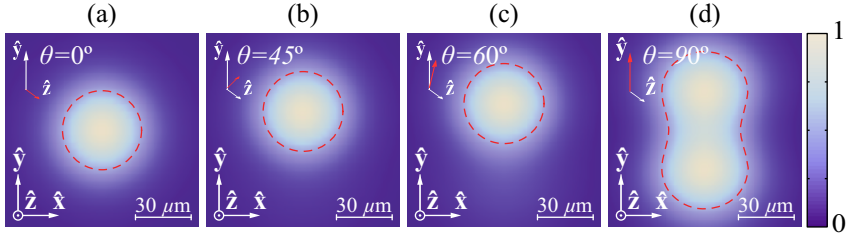


FIGURE 4.9: Point dipole source field at the other side of a NIM layer $w_2 = 40$ nm wider. The dipole source is placed in the xz plane. The dipole is tilted and angle (a) 0 deg, (b) 45 deg, (c) 60 deg and (d) 90 deg with the z axis. The field is evaluated in the image plane, located 80 nm from the object plane. The dipole source radiates at the wavelength of $\lambda_0 = 632.8$ nm. The optical constants of the NIM are $\epsilon_2 = \mu_2 = -1 + 0.1i$.

faster, hindering the observation of other images (O'_2) geometrically reproduced at the rear. Specifically, at z'_2 , the radius of the out-of-focus diffraction spot associated with O'_1 goes beyond the gap $|\mathbf{R}'_1 - \mathbf{R}'_2|$ between this image and O'_2 . This behavior becomes more evident as δ decreases and, more generally, if any physical mechanism improves the capability of the flat lens in resolving closer images placed in the same transverse plane.

4.3.4 Imaging Electric Point Dipoles

For completeness, let us evaluate numerically the scattered wave fields generated by an electric point dipole with arbitrary orientations. For the sake of clarity we assume that the electric dipole is placed in the vacuum. Except for the sign the refractive index of the NIM, n_2 , must be the same as the refractive index in the vacuum, $n_1 = 1$. Nevertheless, realistic losses naturally presented in the imaginary part of the refraction index in the NIM are included being $n_2 = -1 + \delta i$, where $\delta = 0.1$. A good reproduction in the plane $z = z_4$ can be done if the effect of losses is weak. In Fig. 4.9 we plot the intensity in the conjugate of the plane z_0 . Any

value of $w_1 < w_2$ yields the same result as there is a shift invariance. Red dashed lines indicate the points in which the intensity falls to a half of its maximum value. The FWHM Δ_y measured at the $x = 0$ line is the distance between the two points of the dashed line at crossed by the $x = 0$ line. We can see that Δ_y depends on the dipole direction, especially when \mathbf{d} it is contained in the plane xy . For instance, $\Delta_y = 42.4$ nm when \mathbf{d} points in the z -direction; for $\theta = 60^\circ$ the FWHM grows to 43.5 nm, and if \mathbf{d} points in the y -direction the value of the FWHM boosted to 84.6 nm. We should underline the lateral shift at the intensity maximum for the different polar angles. As Fig. 4.9 shows the intensity maximum is placed a distance of (a) 0 nm, (b) 9.5 nm, (c) 13.2 nm, and (d) 19.7 nm from the origin. To sum up, the anisotropy in the amplitude distribution produced in the image plane by a electric dipole challenges the unique description of the resolution in the flat superlens.

4.4 Asymmetric Arrangements and Aberration Correction

An asymmetric flat superlens is a film made of a NIM that is deposited on a smooth, transparent body such as glass with positive dielectric constant. Therefore, the object space has an index of refraction different from that in the image space, leading to an asymmetric arrangement. Originally, this idea was conceived because when using a solid substrate, these imaging devices are mechanically much more stable than a layer sustained in free space [8].

In the case that the lensing flat slab shows effectively a negative permeability, negative refraction allows imaging mainly using homogeneous waves. Moreover, if the index of refraction of the output medium is higher than that index of refraction corresponding to the medium surrounding the object, some evanescent waves

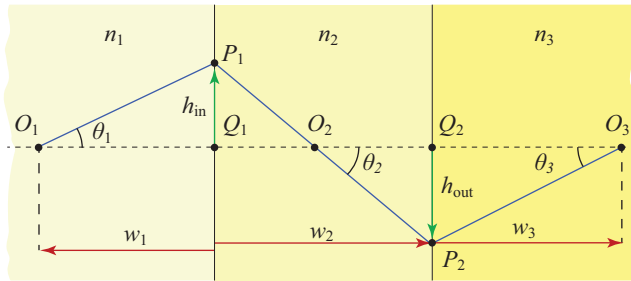


FIGURE 4.10: Schematic representation of an asymmetric flat lens of negative refractive index n_2 and width w_2 .

emitted by the source become homogeneous after passing through the lens. This fact allows the formation of far field images with subwavelength resolution.

Unfortunately there is no perfect image plane in the asymmetric arrangement and the image suffers from aberrations. Note that the root of aberrations in symmetric superlenses is diverse and may be caused by materials having an impedance (and index of refraction) not matched to free space [148, 149], material losses [6, 150], because the equifrequency curve is slightly deformed from an ideal spherical shape particularly for large angular components [151, 152], and caused by the anisotropic effect from nonmagnetic anisotropic media [153, 154]. Here we focus on the index of refraction mismatching that comes naturally in the asymmetric configuration. Moreover, Seidel aberrations have been discussed in different kinds of imaging nanostructures like metallodielectric photonic crystals [155, 156], negative-refractive lenses fabricated out of a silicon-on-insulator photonic crystals slab [155], graded photonic crystals lenses [157], and spherical lenses composed of NIMs [158, 159]. In the previous examples, nonapertured superlenses are usually considered and oblique aberrations may be disregarded.

Let us consider the asymmetric flat lens shown in Fig. 4.10. A point object O_1 is suspended at a distance w_1 from the front face of the superlens made of a material

exhibiting negative index of refraction, $n_2 < 0$. Assuming that the object space is characterized an index of refraction $n_1 > 0$, and that the width w_2 of the lens is sufficiently large, a real Gaussian image O_2 is formed inside the NIM [2]. Traveling through the lens exit surface we reproduce the secondary, outlying image at O_3 in a semi-infinite dielectric of index of refraction n_3 . Provided the index of refraction in the image space turns out to be positive, $n_3 > 0$, the image point O_3 is also real, which is located at a distance w_3 . Here we employ oriented axial distances, i.e. $w_1 < 0$ and $w_3 > 0$ for a real object and a real image, respectively. Also the lens width $w_2 > 0$.

For a nonapertured set up, the chief ray joins the points O_1 , O_2 and the Gaussian image O_3 by means of the same straight line. Let us evaluate the aberration of a ray passing through the point P_2 , which is placed on the exit surface at a height h_{out} , with respect to the chief ray. This aberration is estimated by the optical-path difference of both light rays, i.e., $W = n_1(\overline{O_1P_1} - \overline{O_1Q_1}) + n_2(\overline{P_1P_2} - \overline{Q_1Q_2}) + n_3(\overline{P_2O_3} - \overline{Q_2O_3})$. Note that $\overline{O_1Q_1} = -w_1$, $\overline{Q_1Q_2} = w_2$, and $\overline{Q_2O_3} = w_3$. Finally, this ray aberration reads approximately [160]

$$W(h_{\text{out}}) \approx {}_0a_{20}h_{\text{out}}^2 + {}_0a_{40}h_{\text{out}}^4 + {}_0a_{60}h_{\text{out}}^6. \quad (4.24)$$

The aberration terms ${}_0a_{20}$, ${}_0a_{40}$, and ${}_0a_{60}$ are attributed to defocus, primary spherical aberration (SA), and fifth-order SA, respectively. These aberration coefficients are evaluated by using the geometric relations $\tan \theta_1 = h_{\text{in}}/w_1$ and $\tan \theta_2 = (h_{\text{in}} - h_{\text{out}})/w_2$, and the Snell law. In particular, the Gaussian image plane is given under the condition ${}_0a_{20} = 0$, which yields

$$w_3 = n_3 \left(\frac{w_1}{n_1} - \frac{w_2}{n_2} \right). \quad (4.25)$$

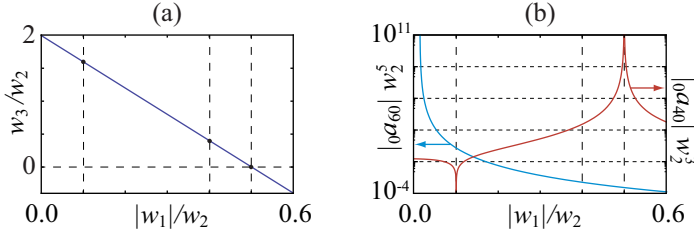


FIGURE 4.11: Geometric imaging for a flat lens of $n_2 = -2$ sandwiched between dielectric media of indices of refraction $n_1 = 1$ and $n_3 = 4$. (a) Gaussian imaging based on Eq. (4.25). (b) Red line represents primary SA given by Eq. (4.26) and blue line represents fifth-order SA.

Therefore an axial displacement of the object point O_1 changing w_1 leads to an image shift following a direct proportion, as shown in Fig. 4.11(a). Note that a real paraxial image O_3 is attained with the condition $w_2 \geq w_1 n_2 / n_1$, that is, if the secondary paraxial image O_2 is also a real image. At the Gaussian image point O_3 , where Eq. (4.25) is satisfied, the aberration coefficient for primary SA gives

$${}_0a_{40} = \frac{n_1 n_2 [n_1^3 (n_2^2 - n_3^2) w_2 + n_2^3 (n_3^2 - n_1^2) w_1]}{8 n_3^2 (n_1 w_2 - n_2 w_1)^4}. \quad (4.26)$$

Note that primary SA cannot be totally corrected for $0 \leq -w_1 < \infty$ when $n_1 = n_3$ except for the perfect lens, where additionally $n_2 = -n_3$. This is a well-known case where high-order aberration coefficients also vanish leading to stigmatic imaging. Also a plane-parallel asymmetric plate may be corrected of primary SA. Provided the equation ${}_0a_{40} = 0$ is satisfied, we obtain a linear relationship between the lens width w_2 and the on-axis object distance

$$w_1 = \frac{n_1^3 (n_3^2 - n_2^2)}{n_2^3 (n_3^2 - n_1^2)} w_2. \quad (4.27)$$

in terms of the index of refraction of the media involved. A given flat lens cannot be corrected of primary SA for more than one object plane, as shown in

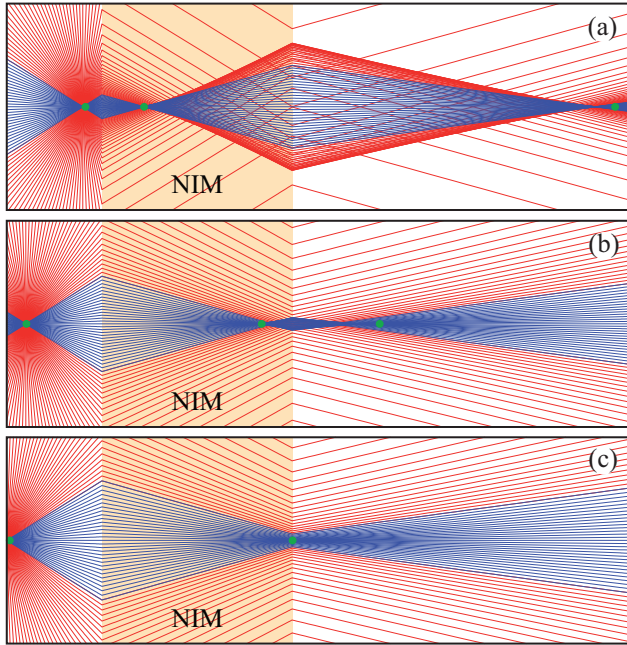


FIGURE 4.12: Ray tracing for an object point located at (a) $w_1 = -0.1 w_2$, which is corrected of primary SA, (b) $w_1 = -0.4 w_2$, and (c) $w_1 = -0.5 w_2$ from the front surface of a flat lens of width w_2 . Refraction index are the same as in Fig. 4.11. Traces corresponding to paraxial (slope lower than 30 deg) and nonparaxial rays are drawn in different colors. Green dots represent conjugated points.

Fig. 4.11(b), and therefore images originated from scatters that fail to keep (4.27) suffer from SA. Furthermore, the primary SA coefficient ${}_0a_{40}$ diverges for the limiting case $w_3 = 0$, excepting when $n_1 = -n_2$, leading to perfect geometric imaging. Therefore quality of the (real) image improves as the (real) object point O_1 come close to the input surface.

In Fig. 4.12, we plot a ray tracing for a flat metamaterial lens of $n_2 = -2$ surrounded by object and image media of index of refraction $n_1 = 1$ and $n_3 = 4$. Fixing the lens width w_2 , Eqs. (4.25) and (4.27) provide the values $w_3 = 1.6 w_2$ and $s_1 = -0.1 w_2$, respectively. The corresponding ray tracing is shown in Fig. 4.12(a).

Stigmatic imaging may produce a convergent focused beam of numerical aperture $n_3 \sin \alpha = n_1$ that leads to an angular semiaperture $\alpha = 14.5$ deg. In our case, the numerical aperture is slightly reduced down to an effective value $\alpha_{\text{eff}} = 10.9$ deg caused by noncorrected high-order aberrations. To inspect the deterioration of the image due to SA effects, we also present in 4.12(b) the ray tracing for a point object placed at $w_1 = -0.4 w_2$ further from the lens entrance surface. We observe a ray distribution that is barely confined around the Gaussian image point O_3 , represented as a green dot in the image space. As a limiting case, we plot in Fig. 4.12(c) the trajectories of rays emerging from a point that is located at $w_1 = -0.5 w_2$ that leads to $0_{a40} \rightarrow \infty$.

We point out that (4.27) gives a negative value of w_1 provided that the index of refraction n_3 in the image plane is either higher or lower than n_1 and $|n_2|$ simultaneously. In order to achieve a subwavelength effect, we aim for transforming evanescent waves emitted by the source O_1 into homogeneous wave modes in the image space. In this case it is preferable for a high-index transparent medium $n_3 > n_1$ to register the image.

To conclude let us make an explanatory remark concerning the index of refraction of the media involved on the analysis of the image formation. The ratio $n_3/n_1 - 1$ provides the relative enlargement of spatial bandwidth corresponding to evanescent waves in the object space that are transformed into homogeneous plane waves in the image space. This is clearly a subwavelength effect, which has been exploited elsewhere [161]. In image formation, this physical phenomenon leads to a superresolving effect. On the other hand, we point out that the value of n_2 is arbitrarily chosen provided it takes a negative value. In fact, this is a degree of freedom that may be profited at the time of imposing an additional constraint of interest.

In order to take a suitable choice for the value of n_2 , we considered the reflection and transmission properties of light that impinges obliquely onto the NIM thin film, which has been deposited on top of the transparent substrate. We set the NIM width by imposing

$$k_{z2}w_2 = -(2m + 1)\pi/2, \quad (4.28)$$

for $m = 0, 1, 2, \dots$. It will eliminate the reflection of light completely, which is intrinsically a dispersive phenomenon depending upon k_0 . This is commonly denominated an anti-reflecting coating. For that purpose we additionally impose that the s-polarized reflection coefficient deduced with the matrix method from Appendix A vanishes, $R_s = 0$. For normally incident light, i.e., $k_{\perp} = 0$, and assuming that $\mu_i = \text{sign}(k_{zi})$, we finally obtain a condition $n_2 = -\sqrt{n_1 n_3}$ involving the index of refraction of all media. Note that the latter equation is held in simulations shown in 4.11, and it is well-known in the theory of antireflecting films when its index of refraction is $|n_2|$. Finally, a quarter-wave layer satisfying (4.28) with $w_2 = \lambda_2/4 (+m\lambda_2/2$ for $m \neq 0$), being $\lambda_2 = \lambda_0/(-n_2)$, is of interest.

In Fig. 4.13(a)-(c), we show the transmission coefficient T_s from the matrix method that has been evaluated for s-polarized waves and superlenses of different widths. Optimum geometric conditions are assumed under all circumstances, where equations (4.25) and (4.27) are satisfied. We observe that $|T_s| \approx 0.5$ for $k_{\perp} = 0$ in all cases and, therefore, reflection is extinguished (Transmittance for s-polarized waves is $|T_s|^2 n_3/n_1$). However, reflection coefficient might have a certain significance in higher spatial frequencies. We also observe a flat variation of the argument of T_s for $k_{\perp} < k_0$, which is a consequence of eliminating primary SA.

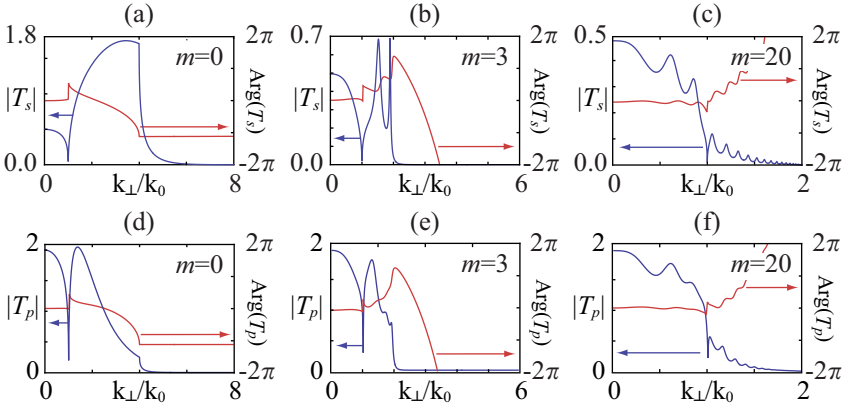


FIGURE 4.13: Transmittance (modulus and argument) for (a)-(c) s -polarized waves and (d)-(f) p -polarized waves in a superlens of $\mu_2 = -1 + 0.001i$ and $\epsilon_2 = -4 + 0.001i$. Surrounding transparent media have again index of refraction $n_1 = 1$ and $n_3 = 4$. We consider different widths for the NIM flat lens: (a) and (d) $w_2 = 0.125\lambda_0$; (b) and (e) $w_2 = 0.875\lambda_0$; (c) and (f) $w_2 = 5.125\lambda_0$. Note that all the horizontal scales are not the same.

For ultrathin slabs, however, $|T_s|$ is of relevance at higher frequencies. By considering a boundless medium of index of refraction $n_1 = 1$, note that there is no time-averaged power flow for $k_\perp > k_0$. The field intensity within this spectral domain, in the presence of the superlens, is by no means zero, and the transmission coefficient might reach values higher than unity, as seen for $m = 0$. In these cases, the time average of the power flow in the object space is supported partially by evanescent waves that, in principle, can contribute to the far field. For them, the phase in the spatial spectrum changes by far and, therefore, aberrated images are expected in the Gaussian image plane. Fig. 4.13(d)-(f), we also present the transmission coefficient T_p in amplitude and phase for p -polarized waves. Finally, from Figs. 4.13(a) and 4.13(d) we observe that these spatial frequencies surpassing $4k_0$ have a small contribution to the image formation; note that the wave field also falls off fast in the transit from the output plane of the lens toward the image plane, thus frustrating a three-dimensional (3D) focusing [145].

For a slab width much higher than the wavelength, the evanescent waves emitted by the source point O_1 cannot reach the entrance face and homogeneous waves satisfying $k_{\perp} \leq k_0$ contribute effectively to the transmitted field in the image space, as shown in Fig. 4.13(c) and 4.13(f) for $w_2 = 5.125\lambda_0$. Decreasing w_2 down to values close to λ_0 leads to the conversion of evanescent waves in the medium 1 to homogeneous waves in the medium 2. In Fig. 4.13(b) and 4.13(e), we observe a critical participation of waves with transverse spatial frequencies $k_0 < k_{\perp} < 2k_0$ for a lens width $w_2 = 0.875 \lambda_0$. In the limit $w_2 = 0.125 \lambda_0$ associated with $m = 0$, we include the spatial bandwidth into the interval $2k_0 < k_{\perp} < 4k_0$ involving evanescent waves in media 1 and 2, which are transformed into homogeneous waves in the image space, as seen in Fig. 4.13(a) and 4.13(d). For that reason such a spectral stretching allows a subwavelength-resolution effect in the formation of far field images.

It is commonly accepted that electric dipole fields, due to their high spatial confinement, are EM sources appropriated for the examination of the limit of resolution in near-field superlenses [55, 120]. For that purpose we use the field distribution generated by an line source reducing 3D calculations to a simpler two-dimensional (2D) problem. The orientation of the line emitter lies along the y axis, which is parallel to the input and output surfaces of the thin NIM coating.

In Fig. 4.14, we present the modulus of the electric field E that is emitted by a line source and that is transmitted through a NIM lens of $\mu_2 = -1 + 0.001i$ and $\varepsilon_2 = -4 + 0.001i$ and different widths. The flat lens is sandwiched between media of index of refraction $n_1 = 1$ and $n_3 = 4$. The object point O_1 is placed at a distance $w_1 = 0.1w_2$ from the superlens, following Eq. (4.27) to minimize primary SA. We compute the scattered field within the interval $z \geq -w_3$ constituting the real image space. The numerical simulations were performed using a finite-element method.

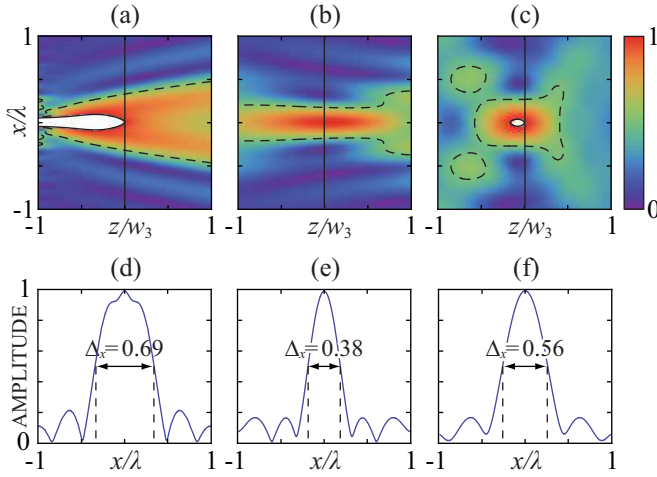


FIGURE 4.14: Modulus of the electric field emitted by a line source and transmitted through a negative-index slab with $\mu_2 = -1 + 0.001i$ and $\epsilon_2 = -4 + 0.001i$ and different widths: (a) $w_2 = 0.125\lambda_0$, (b) $w_2 = 0.875\lambda_0$, and (c) $w_2 = 5.125\lambda_0$. In all cases we present the field within $z \geq -w_3$. The density plots are normalized to unity at the paraxial image point $(x, z) = (0, 0)$. The dashed line indicates points where amplitude falls off $1/2$. The thin vertical line marks the Gaussian image plane. The wave fields corresponding to the Gaussian image plane for (a), (b), and (c) are plotted in (d), (e), and (f), respectively.

If the superlens has a width w_2 below the wavelength, as used in Fig. 4.14(a) and (d), one would expect to achieve superresolution. In this case, however, the FWHM of the modulus of the electric field in the Gaussian image plane yields $\Delta_x = 0.69$ in units of λ_0 , even exceeding the limit of resolution applied to diffraction-limited systems. In order to understand such a behavior, we analyze the transmission coefficients plotted in Fig. 4.12(a). We observe that the phase is stabilized for $|k_x| < k_0$, but it has a fast decreasing variation for higher spatial frequencies. In this sense, the effective bandwidth in the transmission coefficient for frequencies associated with inhomogeneous waves in the medium 1 is, in practical terms, three times larger than the bandwidth for homogeneous waves; therefore

the unbalanced contribution of the different spatial frequencies will make the image recovery difficult. A simple defocus provoked by a shift of the image plane toward the NIM lens serves to diminish the phase variation and aberration effects in the image. Exactly at the exit surface of the superlens, the FWHM of the electric field is $\Delta_x = 0.086$, leading to a subwavelength resolution.

A different behavior is expected for $w_2 \approx \lambda_0$. Figure 4.14(b) illustrates the diffraction behavior of a thin NIM film in the case that $w_2 = 0.875\lambda_0$; that is, $m = 3$ in Eqs. (4.28). The limit of resolution has decreased substantially in the Gaussian image plane, where $\Delta_x = 0.38$. Taking in mind the results shown in Fig. 4.14(b), this superresolving response is attributed to evanescent waves in medium 1 that are converted into homogeneous waves in medium 2, which belong to the spectral range $k_0 < |k_x| < 2k_0$. In this spectral band, however, the coefficient of transmission presents some strong variations in its phase, preventing us from the observation of an aberration-free image. Moreover, the phase of the transmission coefficient increases with k_x so that a defocus is expected to balance high-frequency aberrations. Contrary to the previous case, the on axis shift must be performed moving far from the NIM lens in order to achieve the minimum spot size. In practice, the resolution improvement that is attainable with defocus may be considered negligible.

Finally, if $w_2 = 5.125\lambda_0$, as shown in Fig. 4.14(c), the FWHM of the central lobe in the paraxial image plane yields $\Delta_x = 0.56$ in units of λ_0 , which is close to the diffraction limit, $\lambda_0/2$. In this case, the depth of focus is significantly short, which allows the evaluation of the FWHM along the z axis. This gives $\Delta_z = 9.81$, also in units of λ_0 . We conclude that the focused wave field is localized much stronger in the transverse direction than on axis.

The analysis that we have carried through in previously is essentially for s -polarization. We point out that a similar p -polarization analysis is also possible based on magnetic dipoles aligned along the y axis. For that purpose, now we consider a line source with a uniform distribution of elementary magnetic dipole moment m , which is placed at O_1 . By comparing such a wave field with the scattered field represented in Fig. 4.14, for different widths of the NIM slab, we conclude that discrepancies are appreciable, in general, which are clearly attributed to departures in the coefficient of transmission for both polarizations, namely T_p and T_s . Also we find that the spot size of the wave field is lower for magnetic dipoles.

In order to estimate the limit of resolution unambiguously, we follow an approach that is based on the PSF of the optical system. In fact, it is more appropriate to derive the PSF in 2D; that is,

$$h_2(x, z) = \frac{1}{2\pi} \int_{-\infty}^{\infty} T(k_x) \exp(ik_x x + ik_z z) dk_x. \quad (4.29)$$

In Fig. 4.15, we present the 2D PSF for the same superlens considered, for instance, in Fig. 4.14. One more time, the object plane is placed at a proper distance w_1 to compensate primary SA. We find again that the diffractive behavior of a slab width w_2 below the wavelength differs substantially from that lens with $w_2 \gg \lambda_0$. Additionally, the impulse response is notably different for s -polarized waves and p -polarized waves. Note that the PSF for p -polarized waves is computed by using in Eq. (4.29) the corresponding coefficient of transmission T_p . The FWHM of the PSF central lobe for s -polarized waves takes higher values than those evaluated for p -polarization, especially in ultrathin NIM layers. For instance, if $w_2 = 0.125\lambda_0$, shown in Fig. 4.15, the FWHM of the PSF in the Gaussian image plane yields $\Delta_{x,s} = 0.83$ in units of λ_0 , for s -polarized waves, which is much higher than the

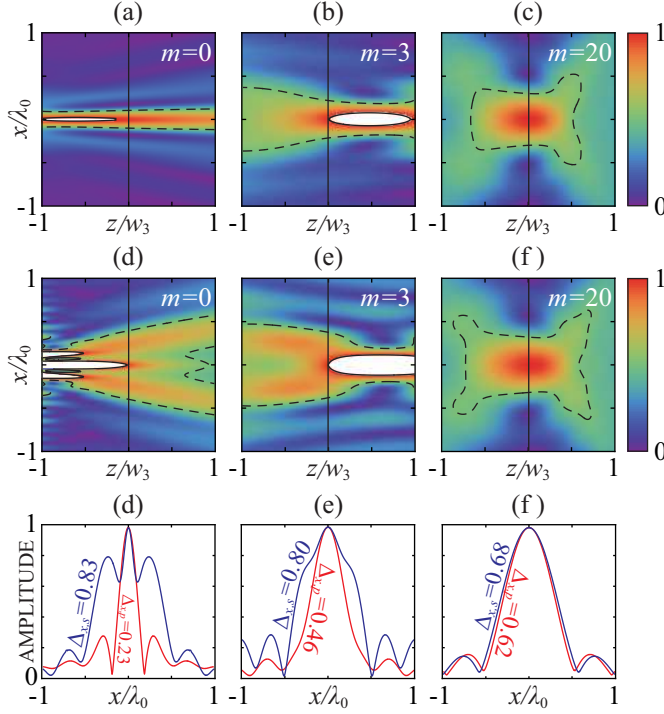


FIGURE 4.15: Modulus of the 2D PSF $|h_2|$ for a NIM flat lens with $\mu_2 = -1 + 0.001i$ and $\varepsilon_2 = -4 + 0.001i$ for different states of polarization: (a)-(c) applies for p -polarized waves and (d)-(f) for s -polarization. In (g)-(i), we chart the data for the Gaussian image plane. The slab width is also varied: $w_2 = 0.125 \lambda_0$ for subfigures placed in the left column, $w_2 = 0.875 \lambda_0$ for subfigures in the central column, and $w_2 = 5.125 \lambda_0$ for plots on the right.

FWHM encountered for p -polarized waves, $\Delta_{x,p} = 0.23$. However, differences derived by the state of polarization are negligible in the case $w_{\text{NIM}} = 5.125 \lambda_0$, as shown in Fig. 4.15(i). From Fig. 4.15(c) and Fig. 4.15(f), we conclude that this is true not only in the Gaussian image plane but also in out-of-focus planes. Note that the FWHM from the PSF is slightly greater than that obtained in Fig. 4.14 from a line dipole. It is worthy to point out that a similar effect has been reported when comparing the PSF and the image of a subwavelength Gaussian beam in metal-dielectric multilayers [162]. In both cases, the explanation is nevertheless

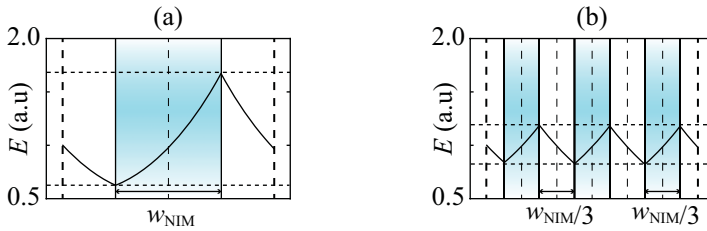


FIGURE 4.16: Evanescent wave field with transverse spatial frequency $k_{\perp} = 2k_0$ traveling from the object plane to the image plane of a flat monolayer and a trilayer superlens. In all cases $\lambda_0 = 600$ nm, $\delta = 0.1$, and $w_{\text{NIM}} = 60$ nm. Thick dashed lines indicate the position of the object plane and the final image plane. Thin dashed lines denotes intermediate image planes.

not difficult. The broader PSF has an irregular phase variation, not shown in Fig. 4.15, which is of critical relevance in the convolution that defines the output field (4.9). In a similar manner, fast changes in the phase of an incident wave field may lead to severe distortions in the image space. Obviously, phases of input fields and phases of PSFs would not play a role if the ondulatory superposition (4.9) are fully incoherent. As a consequence, subwavelength signals transmitted by NIM coatings occasionally yield anomalous localized distributions whose FWHMs surpass the limit of resolution determined by the PSF. We reported the results of this Section in Ref. [163].

4.5 Imaging with Periodic Structures

Originally the flat superlens was conceived as an image-forming system composed of a single NIM slab [2]. Also a silver nanolayer demonstrates the ability of generating an image with sub-wavelength features [3] as will be shown in the next Chapter. Soon it was shown that the limit of resolution of a metallic superlens might be reduced substantially if it is substituted by a set of layers with free-space

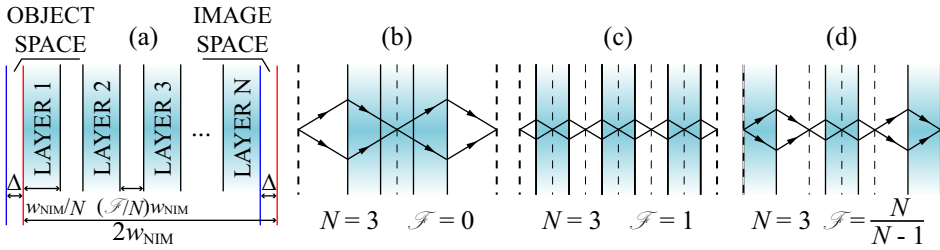


FIGURE 4.17: (a) Scheme of a multilayered superlens containing N uniformly-distributed films. We indicate the zones where we may encounter real conjugated pairs simultaneously. The parameter Δ denotes the width of these two zones. On the right we represent different trilayer superlenses. From (b)-(d), the distance between NIM films increases gradually. Object plane and final image plane are represented by thick dashed lines, and secondary images are denoted by thin dashed lines.

in between [43]. This improvement is based on the lesser amplification of evanescent waves, so that dissipative effects also diminish. In Fig. 4.16 we compute the electric field of an evanescent wave field with transverse spatial frequency $k_{\perp} = 2k_0$ propagating from the object plane toward the image plane for two different NIM superlenses immersed in free space: (a) one lens is composed of a single layer of width w_{NIM} and (b) the second lens is composed of three equidistant films of width (and separation) $w_{\text{NIM}}/3$. The NIM has a width $w_{\text{NIM}} = 60$ nm; also $\epsilon_{\text{NIM}} = \mu_{\text{NIM}} = -1 + \delta i$ being $\delta = 0.1$. In all cases $\lambda_0 = 600$ nm. The amplification of the evanescent wave in the multilayered superlens is significantly lower. The existence of secondary images in the intermediate spaces allows that new evanescent waves with higher spatial frequency contributes effectively in the formation of the final image, thus improving the resolution power [4]. This idea is being upgraded in recent years [39, 55, 162, 164].

A general NIM multilayer flat lens is sketched in Fig. 4.17. Inside the lensing arrangement N NIM layers are distributed uniformly. Every thin film has a width w_{NIM}/N . Therefore w_{NIM} denotes the resultant length after summing up

the widths of all the layers, leading to a distance $2w_{\text{NIM}}$ between the plane of the object and the final geometric image plane. Note that every interface dielectric-NIM generates a stigmatic image that acts as an object for the next interface, giving $2N - 1$ secondary images. The distance between two adjacent layers is $(\mathcal{F}/N)w_{\text{NIM}}$, where \mathcal{F} is a non-dimensional coefficient of proportionality. The width of the multilayer arrangement e results by summing up N NIM films and $N - 1$ interspaces,

$$e = w_{\text{NIM}} \left(1 + \mathcal{F} \frac{N-1}{N} \right). \quad (4.30)$$

In order to generate a real image, the superlens width e should be lower or at least equal to the distance between the object plane and the image plane, $e \leq 2w_{\text{NIM}}$. In this case \mathcal{F} ranges within the interval

$$0 \leq \mathcal{F} \leq \frac{N}{N-1} \leq 2, \quad (4.31)$$

and the natural number $N \geq 2$.

Let us point out three cases of special interest. First, if $\mathcal{F} = 0$ the set of N films are stacked so that the optical system behaves like a monolayer superlens of width w_{NIM} as shown in Fig. 4.17(b). When $\mathcal{F} = 1$ the NIM films and the free space in between coincide in breadth, as illustrated in Fig. 4.17(c). Finally in the limit $\mathcal{F} = N/(N - 1)$, the input and output faces of the arrangement are in contact with the object and image planes, respectively. This is depicted in Fig. 4.17(d).

In order to evaluate the limit of resolution corresponding to multilayer superlenses we estimate the in-focus FWHM of the 3D PSF. In this case the transmission coefficient T used in Eq. (4.10) is computed by using the characteristic matrix formulation for isotropic stratified media [121]. In the numerical simulations we use a NIM of total width $w_{\text{NIM}} = 60$ nm and with an absorption coefficient $\delta = 0.1$; also

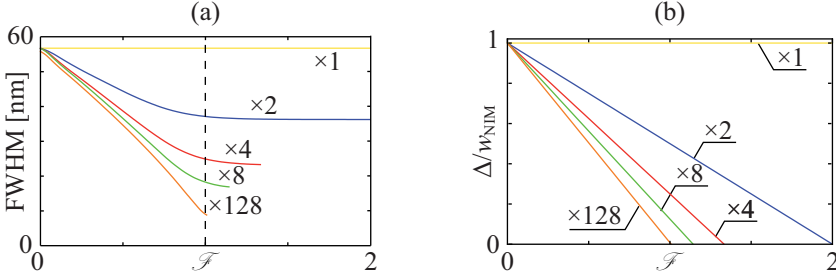


FIGURE 4.18: (a) Limit of resolution for flat superlenses of different number N of layers and separation \mathcal{F} , keeping $w_{\text{NIM}} = 60$ nm fixed. (b) Depth of field normalized to w_{NIM} as a function of \mathcal{F} .

the radiation wavelength is $\lambda_0 = 632.8$ nm. The results are shown in Fig. 4.18(a). Within the interval $0 \leq \mathcal{F} \leq 1$ the FWHM exhibits a linear decreasing behavior. However its value is maintained constant for $\mathcal{F} > 1$. On the other hand, the FWHM decreases if the number N of layers increases up to a saturation limit. In practical terms we may consider that 128 layers represents this limiting case, for which the FWHM is only 8.82 nm.

The multilayer superlens turns up as an alternative of special interest in comparison with the monolayer case since the former reduces the limit of resolution significantly. However this sort of devices withstands a major difficulty in order to generate real images. In the first place, the scattering objects should be located closer to the entrance face of the superlens, and as a consequence the conjugate images are also found nearer the output interface. For convenience we introduce the definition of the depth of field Δ as the width of the two zones where we may encounter real conjugate pairs of objects and images, simultaneously. Such a width is obtained by considering the distance object-image and subtracting the superlens width, $\Delta = 2w_{\text{NIM}} - e$. By employing Eq. (4.30), we finally obtain

$$\Delta = w_{\text{NIM}} \left(1 - \mathcal{F} \frac{N-1}{N} \right), \quad (4.32)$$

that provides a linear relationship between the depth of field and the distance from adjacent layers. Note that Δ is reduced if the interspace width increases.

The depth of field (4.32) as a function of \mathcal{F} is depicted in Fig. 4.18(b) for different number N of layers. It is shown that increasing the interspace between layers reduces the depth of field linearly. The slope of these straight lines, $(1 - N)/N$, quickly drops when the number N of layers increases, reaching the limiting value -1 .

By comparing Fig. 4.18(a) and Fig. 4.18(b) we conclude that an increase in the number N of layers leads to a reduction of the limit of resolution. This effect is achieved in detriment of reducing the depth of field, which results highly harmful in the formation of 3D images. This tendency is repeated if the interspace between layers increases. Optimization of the geometric coefficient \mathcal{F} might consist of reaching a trade-off between the limit of resolution and the depth of field necessary for a specific application.

To further inspect the power of resolution of these stratified superlenses, we have estimated the out-of-focus FWHM in the focal volume. We have computed the 3D PSF for $N = 4$ nanolayers and different values of \mathcal{F} , which are depicted in Fig. 4.19. In the numerical simulation, the wavelength is set $\lambda_0 = 632.8$ nm, and the parameters characterizing the NIM are $w_{\text{NIM}} = 60$ nm and $\delta = 0.1$. In Fig. 4.19 we observe that a higher \mathcal{F} goes with a narrower central peak of the 3D PSF, involving a resolution improvement in transverse planes close to focus, $z = 0$, where sidelobes may be neglected. However evanescent tails grow up with \mathcal{F} , which are plainly seen in planes near the focal plane. These sidelong peaks lead to discontinuities in the limit of resolution, which are derived from our criterion resolution, likewise the case $N = 1$ previously analyzed. In particular, the first

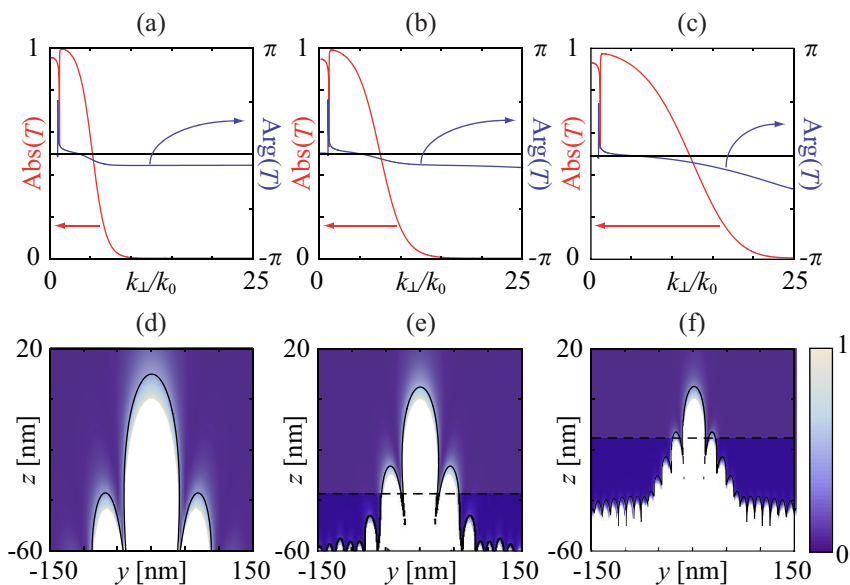


FIGURE 4.19: Subfigures (a), (b), and (c) plot the absolute value (red line) and phase (blue line) of the transmission coefficient T for a superlens of $N = 4$ layers and: $\mathcal{F} = 0$, $\mathcal{F} = 1/2$, and $\mathcal{F} = 1$, respectively. Subfigures (d), (e), and (f) show the intensity of the PSF in the meridional plane yz of the image volume related with the superlenses characterized in (a)-(c). Solid line indicates intensity values which drop to $1/2$, enabling the evaluation of the FWHM for different transverse planes. The dashed line represents the boundary of the real image space

discontinuity is found at $z = -37.7$ nm in Fig. 4.19(a) and it is shifted to $z = -14.5$ nm in Fig. 4.19(c). We remind that a higher interspace between layers, that is an increment of \mathcal{F} , forces a deterioration of the depth of field. In this sense we have included a dashed line in each subfigure to mark the boundary $z = -\Delta$ delimiting the real image space and the virtual image space. It is confirmed that an increase of \mathcal{F} leads to a depth-of-field falloff. The results of this Section can be found in Ref [140].

Chapter 5

Image Formation Using Metals

In the previous Chapter we addressed the image formation with NIMs. This Chapter will partially take advantage of the previous physical analysis to describe the image formation with metals at optical frequencies. Unlike propagation inside NIMs, plane waves inside metals are always inhomogeneous. However, a simple silver slab is capable of imaging in the near-field with resolution beyond the diffraction limit [3]. The evanescent p -polarized field could be transferred through the metal via plasmon-mediated tunneling mechanism. We review the transmission of this electromagnetic signal in a single metal slab and its contribution to the image formation. Both losses and the cutoff wavelength of the SPP mode limit the superlens resolution [7, 165]. This obstacle has been tackled to some degree in several ways. One of them consists in exfoliating the silver slab to be transformed into a PLM [8, 55] with effective anisotropic properties and strong coupling of the SPP modes between neighboring layers. We will study light propagation in metal-dielectric PLMs, and more specifically the mechanism to transfer p -polarized sub-wavelength wave fields without diffraction. In this regard, a connection between

canalization and epsilon-near-zero (ENZ) materials will be introduced.

Additionally, it will be shown a kind of metal-dielectric superlens working in a regimen different from canalization. It is made of two PLM joined together one after another. Rather than light propagation without diffraction negative refraction is induced on the interface separating the PLMs. The width of the second nanostructure is chosen to compensate the antagonist diffraction of the first media. The resulting compound is able to achieve subwavelength resolution.

To conclude, the possibility to fully recover the PSF throughout measures of the intensity at the superlens output interface will be addressed. Specifically, we will use the definition of PSF given in Eq. (4.10) instead of that shown in Ref. [166]. A version of the blind deconvolution algorithm including particular PLM thresholds are considered to this end. While standard blind deconvolution algorithm only recovers the PSF modulus, the version introduced in this chapter is also able to recover the phase.

5.1 Monolayer metallic superlens

The image formation by metallic single-layer superlenses is based on the excitation of SPPs on the entrance and exit interfaces of the slab [167]. As a consequence wave amplification inside the metallic slab compensates the attenuation produced in the surrounding dielectric. The simple model for a metallic superlens it is a layer of low-loss metal. Most of the designs in this kind of lenses use silver due to its lower losses in the optical range of frequencies. To better understand metallic superlens we proceed to analyze superlenses made of an Ag slab sandwiched by air. In Fig. 5.1(a) we plot a single-layer superlens and the field

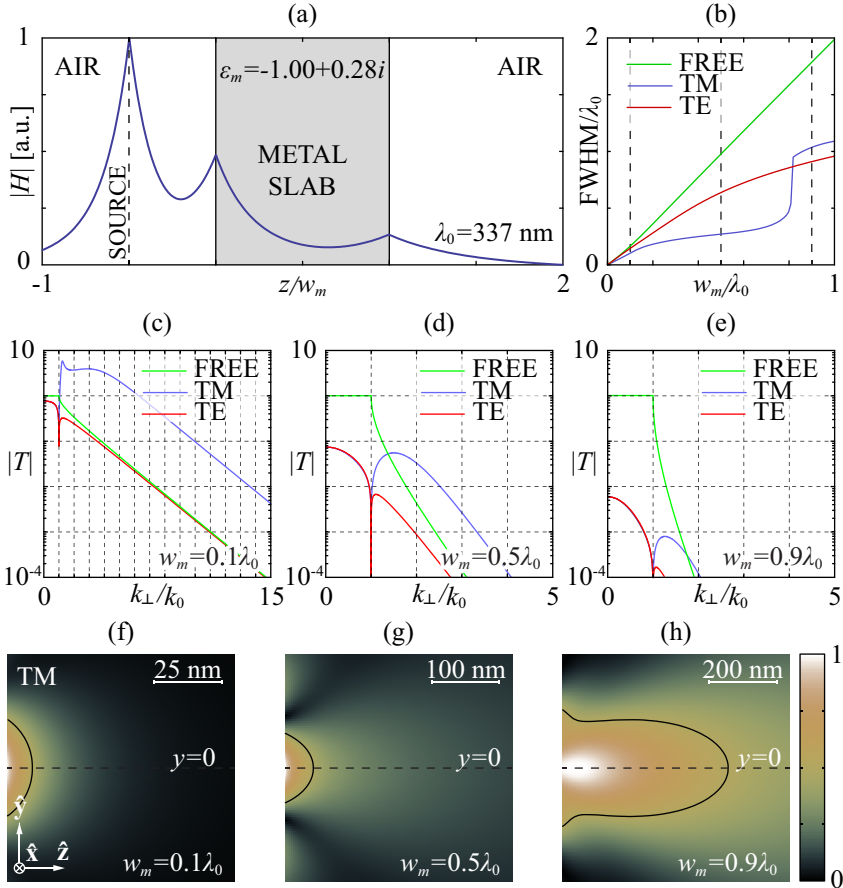


FIGURE 5.1: (a) Schematic representation of a metallic flat lens. In the sketch the magnetic field of a TM-polarized point-like source is superimposed. The field of the point distribution propagates at $\lambda_0 = 337$ nm and is located $w_m/2$ far from the entrance interface of the lens. The lens is a slab of Ag with permittivity $\epsilon_m = -1.00 + 0.28i$ immerse in air. It has a thickness $w_m = \lambda_0/10$. For the same slab with different thickness (b) plots the PSF FWHM at the outside interface in TM (blue) and TE polarization (red) and substituting the slab by air (green). The transmission coefficient of the slab are plotted for $w_m = 0.1\lambda_0$ in (c), $w_m = 0.5\lambda_0$ in (d), and $w_m = 0.9\lambda_0$ in (e). Figs. (f)-(h) show the PSF in the output space corresponding to the transmissions (c)-(e) of the TM polarization. The PSF is normalized to its value at the output surface where $\mathbf{R} = (0,0)$. The black contours correspond to the values of the PSF equal to 0.5.

excited with a TM-polarized point source placed $w_m/2$ far from the entrance of the lens. In the absence of the metal slab the source produces a field distribution $H(y) = \delta(y)$ in the object plane. Consequently, the field in the image space of the metal slab matches the 1D PSF. The lens has a width $w_m = 0.1\lambda_0$. The dipole radiates at a wavelength $\lambda_0 = 337$ nm. At this wavelength the Ag permittivity is $\epsilon_m = -1.00 + 0.28i$ [103]. The slab width is slightly longer than the Ag evanescent decay length at this wavelength (about 20 nm) however, we can see values of $|H|$ at the outside interface smaller but negligible. In fact, there are two relative maxima at both slab interfaces. The reason for these maxima relies on the SPPs intensifying the evanescent waves with spatial frequencies closed to the SPP resonance.

In order to understand how SPPs affect the resolution in these superlenses let us pay attention now to the FWHM values at the output interface plotted in Fig. 5.1(b). A large transmission band is necessary to produce a small FWHM in the PSF at the output interface, consequently plasmon resonances make TM-polarized wave fields candidates to achieve it. In Fig. 5.1(c)-(e) we observe that these resonances make always TM polarization transmission broader than TE. However the TM FWHM rapidly grows at $w_m \sim 0.8\lambda_0$. The contribution of the evanescent frequencies to the image produces sidelobes that affects the FWHM as we can see in the PSF from Fig. 5.1(h). Contrary, in Fig. 5.1(f) and (g) field is mostly localized centered in the vicinity of the output interface. A flat transmission in modulus and phase is the key to avoid the sidelobes effect. Also, higher cutoff frequencies would be desirable to improve the resolution. With this in view, we need to add new elements to the design of the superlens.

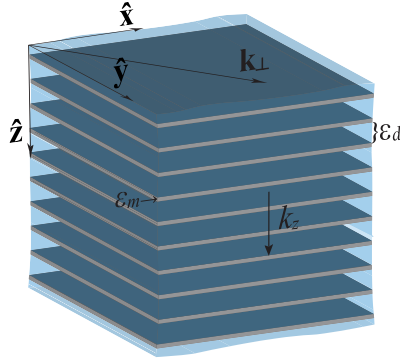


FIGURE 5.2: Geometry of the bilayer periodic structure; ϵ_m stands for permittivity in the metal and ϵ_d for the dielectric.

5.2 Image-Forming Multilayered Stacks

By coupling a few of these elementary thin lenses we may compose a PLM capable of transmitting high-frequency electromagnetic waves by resonant tunneling [43, 168]. Assuming a perfect periodic process, a set of evanescent waves is effectively converted into propagating Bloch waves with characteristic pseudo-moment and consequently carrying EM energy. Additionally, transmission and reflection coefficients depend on Fabry-Perot resonances due to the finite size of the PLM. These resonances distort features at certain spatial frequencies.

5.2.1 Canalization

We can preclude dephasing of different spectral components in a PLM by tuning the filling factors of the materials involved. As a result the wave fields propagate inside the multilayered projecting the optical wavefront in between its external boundaries almost without diffraction including sub-wavelength details. We will refer to this effect as canalization (also known as self-collimation).

A simplified description of PLM in the self collimation regime may be achieved by using the EMA [126, 169] in the special case when one of the elements in the permittivity tensor approaches zero and thus, the uniaxial metamaterial becomes extremely anisotropic. We will refer to the materials in this case as ENZ materials. The ENZ metamaterials have been widely analyzed, which may have other simple forms like a metallic mesh of thin wires and embedded metallic nanoparticles in a dielectric medium [170–172]. These metallic composite materials strongly modify the emission of a nearby source, canalizing the radiated energy along its effective optical axis [4, 43, 162, 173, 174]. However, even in the long-wavelength regime, the dispersion of ENZ multilayers may change drastically caused by non-local effects in the structured media [175–177].

A periodic nanostructure of bilayered unit cell is depicted in Fig. 5.2 representing an ENZ material. The relative permittivity of the dielectric ϵ_d is positive and dispersionless. This one-dimensional metamaterial is formed by alternating layers of dielectric and metallic materials oriented perpendicular to the z -axis. In particular, w_m stands for the thickness of a metallic film, and the dielectric-layer thickness is w_d . If the multilayered periodic structure is ideally unbounded, one may describe dispersion by means of the Bloch equation (3.9).

The subwavelength character of a PLM relies on the fact that its period $\Lambda = w_m + w_d$ is much smaller than the operating wavelength and therefore $k_0 w_{m,d} \ll 1$. Under these conditions EMA becomes reliable and sets the framework for the uniaxial ENZ. Interestingly, designed ENZ metamaterials are also obtained below the plasma frequency. In this spectral range of frequencies $\epsilon_m < 0$ and $\epsilon_d > 0$, enabling ϵ_{\perp} to change its sign depending on the layer thickness w_m and w_d . Specifically, this occurs at the frequency ω_{\perp} introduced in Eq. (3.17), which is depicted

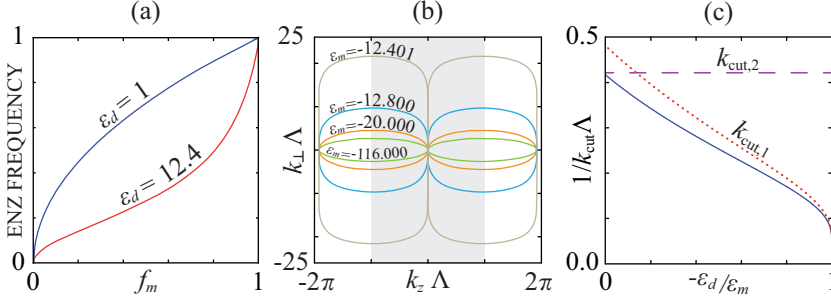


FIGURE 5.3: (a) Dependence of the ENZ frequency ω_\perp (in units of ω_p) upon the metal filling factor, f_m . (b) Dispersion of Ag-GaAs nanomembrane multilayer with extremely thin layers ($\Lambda \ll k_p^{-1}$) at different frequencies, that is for some values of $\epsilon_m(\omega)$. In all cases $\epsilon_\perp = 0$. (c) Cutoff frequency k_{cut} derived from the plots shown in (b) in terms of the ratio $-\epsilon_d/\epsilon_m$. We included the approximations given in Eqs. (5.2) and (5.3) set in dotted and dashed lines, respectively.

in Fig. 5.3(a), in terms of the metal filling factor, $f_m = w_m/\Lambda$, for different dielectric materials. In the spectral domain, the EMA dispersion relation previously introduced in Eq. (3.20) represents an ellipse provided that both ϵ_\perp and ϵ_\parallel are positive when $\omega > \omega_\perp$. On the contrary, if $\epsilon_\parallel/\epsilon_\perp$ is negative, occurring in the low-frequency regime, $\omega < \omega_\perp$, Eq. (3.20) gives a hyperbola. Exactly at ω_\perp the dispersion curve reduces to $k_z = 0$ for all k . In principle, this enables a given subwavelength scattered field at the input plane of the PLM to be reproduced exactly at the exit plane by means of a perfect phase matching of the signals [43]. This self-collimation regime will govern wave propagation under the more general condition $\epsilon_\perp/\epsilon_\parallel \rightarrow 0$, and thus we alternatively might impose ϵ_\parallel to be infinitely large [56]. As shown in Fig. 5.3(a) ω_\perp decreases at lower filling factors and for dielectrics of higher refractive index.

We performed exact calculations of the dispersion Eq. (3.9) for ϵ_\perp -zero PLMs composed of Ag-GaAs. For sufficiently thin layers, the curves conserve their shape; this occurs when the period Λ is lower than the decay length (23 nm for

Ag). Figure 5.3(b) shows the dispersion at different frequencies. In the numerical simulations, silver is set to have a plasma frequency $\omega_p = 12.9 \text{ fs}^{-1}$, which allows us to estimate $\text{Re}(\varepsilon_m)$ in good agreement with experimental data, especially in the near infrared [104]; for illustration, we also consider a dispersionless isotropic medium with $\varepsilon_d = 12.4$, which for instance would correspond to GaAs around $\lambda_0 = 1 \mu\text{m}$ [178]. The metal filling factor at every frequency was chosen provided that $\varepsilon_{\perp} = 0$,

$$f_m(\omega) = \frac{\varepsilon_d}{\varepsilon_d - \varepsilon_m(\omega)}. \quad (5.1)$$

Note that $f_m \approx \varepsilon_d \omega^2 / \omega_p^2$ if $\omega \ll \omega_p$, and $f_m \approx 1$ near the plasma frequency.

In Fig. 5.3(b), we observe a bounded interval for k -frequencies that is limited by the cutoff frequency k_{cut} ; this occurs under the condition $k_z = \pm\pi/\Lambda$. The width of such spectral band, $2k_{\text{cut}}$, increases for higher ω , as soon as ε_m approaches $-\varepsilon_d$. In principle, this bandwidth only depends on retardation effects in the limit $\varepsilon_m = -\varepsilon_d$, as was early proved in the context of superlensing [179]. The highest frequency k_{cut} can be estimated by applying the quasi-static approximation ($k_{m,d} = ik_{\perp}$) in Eq. (3.9) at $\cos(k_z\Lambda) = -1$, leading to the following approach,

$$k_{\text{cut},1} = \frac{1}{\Lambda} \ln \frac{8}{(1 + \varepsilon_d/\varepsilon_m)^2}. \quad (5.2)$$

In Fig. 5.3(c), we represent the approximated cutoff $k_{\text{cut},1}$ from Eq. (5.2) to be compared with the exact value of the cutoff frequency k_{cut} . Validity of Eq. (5.2) is restricted to values of ε_m near $-\varepsilon_d$. Figure 5.3(c) allows us to analyze dispersion at low and moderate frequencies, specifically for cases satisfying $|\varepsilon_m| > \varepsilon_d$. However, it is not difficult to demonstrate that, in the quasi-static regime, Eq. (3.9) gives approximately the same dispersion curve in the $k_z k_{\perp}$ plane, previously normalizing the frequencies by Λ^{-1} , for $\varepsilon_m = -\gamma\varepsilon_d$ and also for $\varepsilon_m = -\gamma^{-1}\varepsilon_d$, on

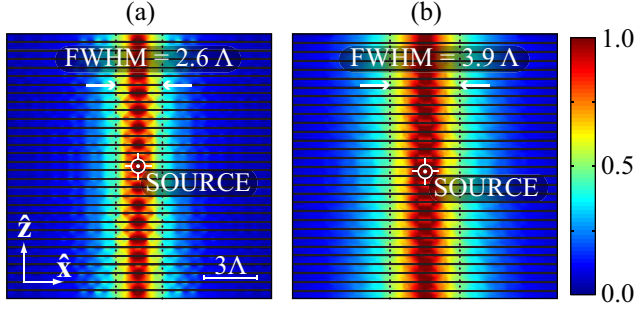


FIGURE 5.4: Radiated intensity $|B|^2$ by a line source immersed in the centre of Ag-GaAs PLM. FEM simulations were performed at: (a) $\lambda_0 = 534.9$ nm ($\epsilon_m = -12.401$) with $f_m = 0.49998$ and (b) $\lambda_0 = 542.8$ nm ($\epsilon_m = -12.800$) with $f_m = 0.49206$.

the condition that $\epsilon_{\perp} = 0$. Therefore, we may infer the diffraction behavior for $-\epsilon_d/\epsilon_m > 1$ straightforwardly, provided we have that behavior for $0 < -\epsilon_d/\epsilon_m < 1$ as shown in Figs 5.3(b) and 5.3(c). This is based on the fact that the changes $\gamma \rightarrow \gamma^{-1}$ and $f_m \rightarrow 1 - f_m$ do not modify Eq. (3.9) in the limit $k_{m,d} = ik_{\perp}$.

In Fig. 5.4, we depict the spatial distribution of the TM field \mathbf{B} emitted by a line source that is embedded in the center of some uniaxial ϵ_{\perp} -zero PLMs. The \mathbf{B} field contained in the xy plane represent the EM fields as a linear combination of space–time harmonic waves. The 2D simulations were performed by using the RF module in the COMSOL Multiphysics modeling environment (TM-mode analysis), which is based on the finite element method. In all cases, the period Λ is three orders of magnitude shorter than the wavelength λ_0 , which is chosen such that $\epsilon_m = -12.401$ in Fig. 5.4(a) and $\epsilon_m = -12.800$ in Fig. 5.4(b). Note that our Λ surpasses the nanoscale limit resulting in a less-realistic picture, however, the physical illustration involving superlensing is clearly improved. The contour plots of $|B|^2$ demonstrate the self-guiding of the radiated field along the z axis. The FWHM of the canalized fields is $\Delta = 2.6\Lambda$ and $\Delta = 3.9\Lambda$, respectively. Bearing in

mind that $k_{\text{cut}}\Lambda = 21.6$ in the first case, and $k_{\text{cut}}\Lambda = 9.68$ in the second case, we infer that the product $k_{\text{cut}}\Delta$ is barely conserved. As a result, deep-subwavelength lensing is clearly enhanced in the limit $\epsilon_m \rightarrow -\epsilon_d$, a fact that on the other hand is reported elsewhere [43].

Note that absorption in the metal also plays a relevant role in the self-guiding effect of subwavelength optical signals. A simple inspection of Eq. (3.9), as shown in Fig. 5.3(b) but including a non-negligible imaginary part for ϵ_m , provides a more realistic insight of our problem. In our numerical simulations, we included $\text{Im}(\epsilon_m) = 0.84$ following [104] for silver in the spectral band under consideration. At $\lambda_0 = 534.9$ nm, we found an extremely low value of $k_z = 0.0054(1 + i)\text{m}^{-1}$ at $k_{\perp} = 0$, independently of Λ and provided that it remains much lower than the evanescent decay length. In fact, k_z is maintained practically unaltered up to $k_{\perp} = k_0$ and changes smoothly (specially $\text{Re}(k_z)$) at higher spatial frequencies. Therefore, the PLM retains the main feature of ENZ metamaterials. However, evanescent decay length inside the PLM is significantly short, $l_{\text{PML}} = 93$ nm.

In practical terms, these numbers also apply by changing the wavelength at $\lambda_0 = 542.8$ nm. We point out that optimization of the PLMs might lead to propagation lengths surpassing a wavelength, as reported in [180]. Alternatively, this situation can improve by incorporating active gain materials in the layered medium as pointed out in [11].

In Fig. 5.3(b), we showed that dispersion in uniaxial ENZ PLMs deviates from the self-collimation regime at low frequencies. Specifically, if $-\epsilon_d/\epsilon_m \ll 1$, occurring in practical terms in the infrared and at lower frequencies, the bandwidth $2k_{\text{cut}}$ of k_{\perp} -frequencies is severely reduced. In fact, these spatial frequencies are

roughly limited by the period Λ of the PLM, exclusively. In this case, we estimate k_{cut} by means of simplifications of Eq. (3.9), again, based on the quasi-static approximation. After a simple but full-length calculation, we finally obtain the following approximated value of the cutoff frequency,

$$k_{\text{cut},2} = \frac{2 + W(4/e^2)}{\Lambda}, \quad (5.3)$$

that is $k_{\text{cut},2} \approx 2.37/\Lambda$, where $W(\cdot)$ is the product log function. Note that $k_{\text{cut},2}$ is included in Fig. 5.3(c), demonstrating that it is accurate in the limit $\omega \rightarrow 0$. We reported the results given above in Ref [181].

5.2.2 Diffraction-Management

Now we will follow a different approach that leads to control dephasing of sub-wavelength outputs. This is based on counterbalancing the phase response of high-transparent metallic superlenses in order to flatten the overall phase mismatch at the image plane. In geometrical terms, negative refraction of high-frequency Bloch waves excited by a nanosized object contributes to achieve nearly-stigmatic subwavelength imaging. This study is elicited by a recent direct observation of light focusing through a PLM flat lens designed and fabricated using a III-V semiconductor slab to operate at optical frequencies [182]. More sophisticated devices following the above primitive idea have been presented [183]. However the spot size of a reproduced localized field would be clearly diffraction limited. A recent tentative to overcome this limit by using uniform arrays of plasmonic waveguides has been proposed elsewhere [184–186]. Here we do not take into consideration hybrid metal/dielectric media with axial symmetry; on the contrary,

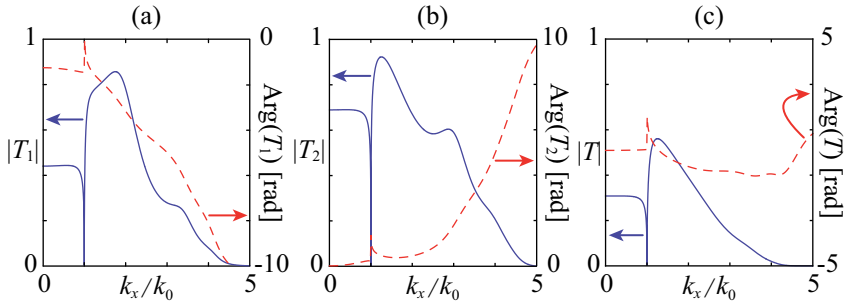


FIGURE 5.5: Transmission coefficients in modulus and phase for finite periodic structures made of silver and a dielectric: (a) SrTiO₃; (b) GaP. In (a) we have $N_1 = 19$ silver layers with a filling factor of $f_{m,1} = 0.35$ within a period of $\Lambda_1 = 30$ nm. In (b) we consider $N_2 = 7$ periods of $\Lambda_2 = 50$ nm for a silver filling factor $f_{m,2} = 0.50$. In both stacked devices the surrounding medium is the vacuum. (c) The transmission coefficient of the coupled structure.

we consider PLM devices superlens where the wave field is partially transmitted with a complex amplitude.

In our discussion we shall consider that two flat superlenses SL_1 and SL_2 are firmly attached. The transmitted field, $H_y = TH_0$ is written as the combination of $T_{1,2}$ and $R_{1,2}$, the transmission and reflection coefficients of the superlenses SL_1 and SL_2 that can be deduced from the transfer matrix procedure introduced in Appendix A. The phase increment of the transmitted wave H_y with respect to the incident field H_0 is the result of a summation of two terms, corresponding to the arguments of the phasors T_1, T_2 respectively. We call it the phase addition rule. In this sense, the dependence of $\arg(T_1)$ upon k_x might be compensated with a prescribed superlens SL_2 leading to an ultraflattened curve at least within a given spectral band. Next we consider a procedure to play on the phase addition rule in order to achieve subwavelength aberration-free images.

In Fig. 5.5 we represent the spectral dependence of the transmission coefficient

$T_{1,2}$ both in modulus and phase for a couple of metallodielectric multilayered devices at $\lambda_0 = 485$ nm. Figure 5.5(a) shows the transmission coefficient T_1 for a periodic structure consisting of $N_1 = 19$ silver layers ($A_g = -7.754 + 0.727i$) hosted in SrTiO_3 ($\text{SrTiO}_3 = 6.596 + 0.070i$). A thin metallic slab is symmetrically displaced in the center of the unit cell, which has a period of $\Lambda_1 = 30$ nm, in such a way that the filling factor of silver is $f_{m,1} = 0.35$. Also the surrounding medium of the stack is considered to be the vacuum. Finally, the evaluation of T_1 is carried out by using a standard transfer matrix formalism given in Appendix A. From Fig. 5.5(a) we observe that, in practical terms, our finite lattice cannot transmit spatial frequencies beyond $k_x = \kappa_{\text{SrTiO}_3} k_0$, where the effective index of refraction is $\kappa_{\text{SrTiO}_3} = 4.35$ in our numerical example. Since the refractive index of SrTiO_3 , that is $n_{\text{SrTiO}_3} = \text{Re}\sqrt{\epsilon_{\text{SrTiO}_3}} = 2.57$, is considerably lower than κ_{SrTiO_3} , a resonant tunnelling effect driven by SPPs is evident. Moreover, a decreasing variation of the phase of T_1 in terms of k_x is clearly revealed. In Fig. 5.5(b) we depict the transmission coefficient T_2 for a second lattice made of $N_2 = 7$ silver slabs placed on GaP ($\epsilon_{\text{GaP}} = 13.287$). In this case the period is $\Lambda_2 = 50$ nm and the filling factor of silver is $f_2 = 0.50$. While the effective index of refraction κ_{GaP} is comparable with that obtained in the previous case, the phase shows a completely different behavior. Now the complex argument of the transmittance increases for higher spatial frequencies k_x . Note also that the phase increment observed in the GaP lattice goes around 3π rads, which approximately corresponds to the phase decrement attributed to the SrTiO_3 multilayer. Then a coupled device including both types of periodic nano-structures would yield a compensated-phase response. This finding is confirmed in Fig. 5.5(c) where the net phase deviation of the transmission coefficient T is always lower than π rads within the effective bandwidth $|k_x| < \kappa k_0$, where $\kappa = 4.5$ once again.

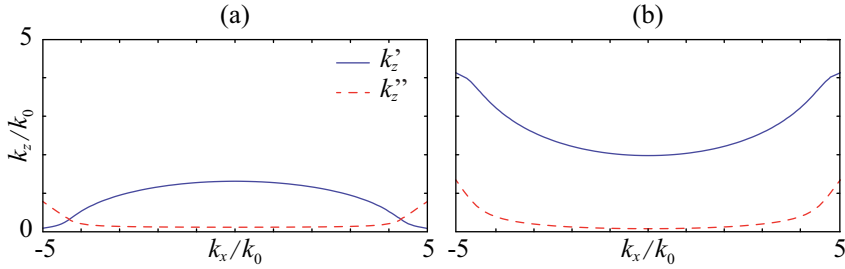


FIGURE 5.6: Isofrequency curves given from Eq. (3.9) for hybrid silver-dielectric periodic media containing (a) SrTiO₃ and (b) GaP. Note that k'_z and k''_z are the real part and the imaginary part of k_z , respectively.

The different behavior observed in the phase dependence of transmittances $T_{1,2}$ upon transverse spatial frequencies k_x may be explained from the isofrequency curves of the periodic lattices. In Fig. 5.6 we represent the Bloch dispersion equation (3.9) corresponding to p -polarized waves propagating within an infinite periodic multilayered structure, where the metal-dielectric interfaces are parallel to the xy plane. Furthermore the component $k_z = k'_z + ik''_z$ of the wave vector represents a Bloch pseudo-moment. From Fig. 5.6 we infer that the superlattice made of SrTiO₃ has an isofrequency curve with normal negative curvature. The propagator $\exp(ik'_z z)$ indicates that the dephase accumulated by a wave field is directly proportional to k'_z . Neglecting impedance mismatch at the input and output planes of the multilayered device, we expect that the dependence of k'_z upon k_x follows the same variation observed in the argument of the transmission coefficient T_1 upon k_x . Figure 5.5(a) and Fig. 5.6(a) indicate that this is in good agreement up to the normalized cutoff frequency κ given by the solution of the equation $k'_z(\kappa k_0) = k''_z(\kappa k_0)$ that is $\kappa = 4.3$. Note that κ represents essentially the effective index of refraction κ_{SrTiO_3} described above. Next we may follow a similar procedure to relate the isofrequency curve given in Fig. 5.6(b), which corresponds to the periodic medium containing GaP, with the phase spectral dependence of

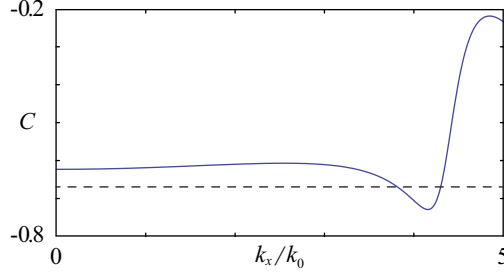


FIGURE 5.7: Dependence of the parameter C , defined in Eq. (5.4), on the spatial frequency k_x . Note that C is practically invariant within the spectral domain $|k_x| < 3.5k_0$.

the transmission coefficient T_2 given in Fig. 5.5(b). In this case we conclude that the positive curvature of the dispersion equation explains the phase increment observed at higher spatial frequencies k_x .

Phase compensation attributed to coupling of two MD superlattices with isofrequencies of opposite curvature also renders a geometrical interpretation of our results. A wave packet that passes through the interface joining both MD superlattices experiences negative refraction. When the fields propagate within the lattice composed of SrTiO_3 , the angles corresponding with each unit vector \mathbf{N} pointing along the group velocity, assuming first that $k_{x0} = k_0$ and second that $k_{x0} = 3k_0$, as measured with respect to the z axis are numerically estimated from Fig. 5.6(a) and (b) giving $\theta_1 = +0.07$ rad and $\theta_1 = +0.28$ rad, respectively. Note that these angles are significantly small. If these two wave packets travel through the multilayered medium containing GaP, now these angles yield $\theta_2 = -0.12$ rad and $\theta_2 = -0.44$ rad, respectively. Let us point out that the parameter

$$C = \frac{\tan \theta_1}{\tan \theta_2}, \quad (5.4)$$

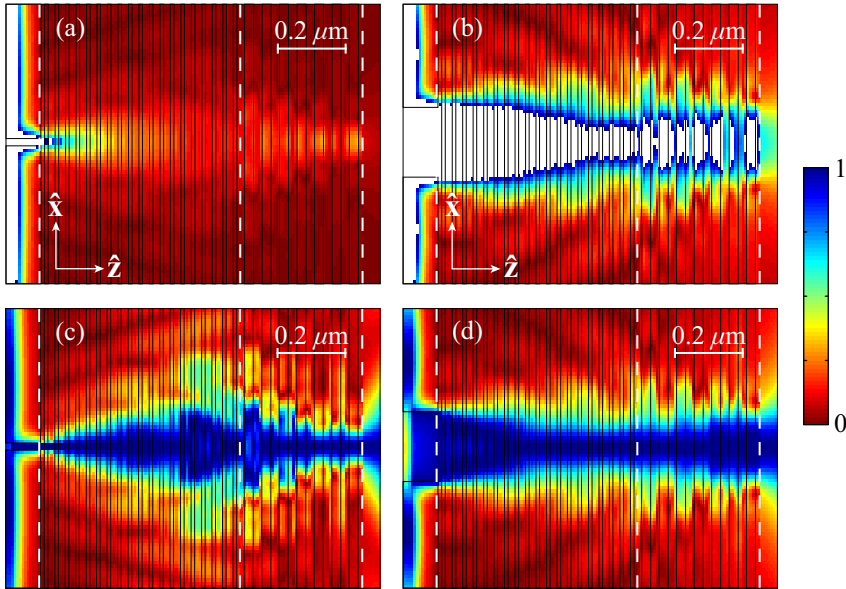


FIGURE 5.8: FEM simulations shown superlensing of the device composing the MD superlattice including SrTiO_3 , set on the left, and that containing GaP. In (a) the slit width is 20 nm and in (b) the slit width is 200 nm. For the sake of clarity, again we show the modulus of the magnetic field in (c) and (d) as it is normalized plane by plane.

takes a value approaching -0.62 in both cases. Moreover C is a quantity approximately conserved for $|k_x| < 3.5k_0$, as shown in Fig. 5.7. This result provides a significant contribution to our geometrical interpretation of the proposed diffraction-managed imaging. A light ray emerging from a point on axis that propagates from a plane $z = 0$ to $z = L_1$ in the first medium and, immediately after, travels in the second medium up to $z = L_1 + L_2$, such that $C = -L_2/L_1$ holds, gets its way back to the z axis. Note that $L_{1,2} = N_{1,2}\Lambda_{1,2}$ in our numerical case, and that we have $-L_2/L_1 = -0.614$.

As mentioned above, invariance of C holds for a wide spectral range. This is important if we consider a localized source in the input interface of the first MD

finite lattice. The light rays emerging from this point object are conveniently deviated, by means of negative refraction, at the surface that joins the periodic media involved. As a consequence all these rays are focused precisely at the exit plane $z = L_1 + L_2$. In other words, the condition of stigmatism is approximately satisfied so that nearly aberration-free images may be formed by our device. We point out that spherical aberration is not completely removed in this study, which is clearly seen in the spectral band $3.5 < |k_x| < 4.5$. As a result it shall finely decrease the resolving power of the imaging system. This is illustrated in Fig. 5.8 by using FEM simulations in COMSOL Multiphysics 3.5. In front of our device we insert a Cr layer whose width is 100 nm. Also the Cr film has a centered slit aperture whose width takes a value of 20 nm in Fig. 5.8(a). A p -polarized plane wave collides with the Cr film that collects part of the light, which subsequently is guided toward the entrance surface of the diffraction-managed superlens. Thus the deep-subwavelength wave field in the input is diffracted inside the first multilayered medium; immediately after reaching the GaP superlattice it is continuously compressed along the transverse direction. The output magnetic field consists of a strong central lobe whose FWHM is $\Delta = 130$ nm, that represents only $0.27\lambda_0$. This confirms the subwavelength character of the image-formation process in spite of the fact that the object plane and the image plane are separated by a distance of 950 nm that supposes barely twice the wavelength λ_0 . We have repeated the FEM simulations for other slit widths, and we have observed that the response of the superlensing device is practically the same whether the slit width is substantially smaller than Δ . Therefore Δ stands for the limit resolution of the superlensing coupled device. For wider slits, on the contrary, the magnetic field at the output plane resembles that at the input plane. In Fig. 5.8(b) we show the wave field for a slit aperture of 200 nm. In this case, the beam width that is excited by the

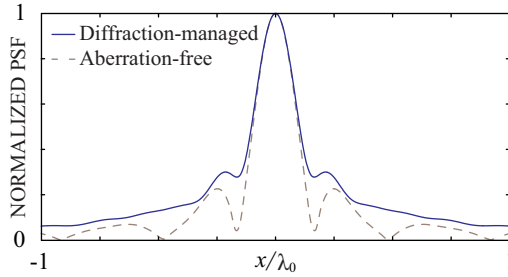


FIGURE 5.9: Modulus of the 1D PSF at the image plane of our diffraction-managed superlens. The 1D PSF of an aberration-free system maintaining the same $|T|$ is also represented graphically.

plasmonic slit is conserved not only at the exit but also all along the periodic media. This self-collimation regime is the result of the strong anisotropy of the two superlattices involved, as shown in Fig. 5.6. Thus, the low frequency of the spatial spectrum associated with the scattered EM waves at the input plane leads to the dominant self-collimation of the EM flow.

To estimate the limit of resolution we alternatively employ the 1D PSF, which is simply the Fourier transform of the amplitude transfer function as shown in Section 4.2. Figure 5.9 depicts $|h(x)|$ that represents the modulus of the 1D PSF at the image plane of our diffraction-managed device. The FWHM of the central peak yields $0.214\lambda_0$, which is very close to limit of resolution Δ obtained from FEM-based numerical simulations. For the sake of completeness we also have represented the 1D PSF for a purely aberration-free setup with the same transmission strength $|T|$ as shown in Fig. 5.5(c). Therefore the argument of the transmission coefficient is set arbitrarily constant. After performing the corresponding 1D Fourier transform of $|T(k_x)|$ we estimate that the FWHM of the diffraction-free 1D PSF decreases up to a value of $0.195\lambda_0$. We conclude that the 1D impulse response is not broadened significantly due to residual phase offset. In general terms we find that the 1D PSF is weakly blurred, which is confirmed by simply

inspection of the small strength associated with its closest sidelobes. This fact is of relevance in coherent imaging of either localized scatterers or extended objects. We reported the results given above in Ref. [187].

5.3 PSF Recovery Assisted by the Blind Deconvolution Algorithm

Major results presented in this Thesis are sustained in the PSF analysis, particularly the imaging process in multilayered structures. From an experimental point of view the PSF must be recovered from the image intensity measures of a detector. However, an accurate measurement of the PSF is a challenging task in practice, specially if we are working with superresolving images in the optical range. In this last Section we propose a realistic experimental set-up to measure the PSF in a multilayer structure. Moreover, we introduce a method to recover the PSF (intensity and phase) from the output intensity measures of a given PLM superlens. This approach can be seen as a modification of the blind deconvolution algorithm [188, 189] that includes a phase retrieval. We also reported the results of this Section in Ref. [190].

The experimental setup shown in Fig 5.10 will be used to explain the method. We consider a one-dimensional TM-polarized wavefront incident on a PLM through a mask consisting of a good conductor, such as Cr, which is thin and has a binary transmittance. Assuming that the layers within the PLM are optically linear and are infinite, the PLM defines a scalar linear shift-invariant optical system. In

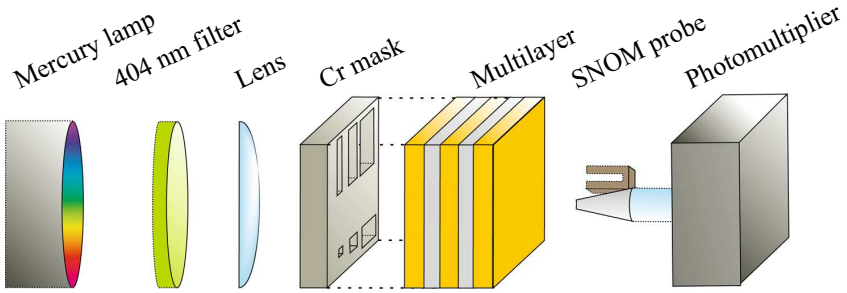


FIGURE 5.10: Experimental setup. A layered metamaterial deposited on a mask with nonperiodic apertures is scanned with a SNOM microscope

spite of the short coherence length of various sources used with SNOM, the sub-micrometer thickness of the MD media and layer thickness of the order of $\lambda/10$ make it necessary to consider a coherent model for the measurement.

Before describing the algorithm it is well worth remembering that the PLM output magnetic field, $H_{\text{out}}(x)$, can be expressed as a convolution of the 1D PSF, $h(x)$ and the input signal, $H_{\text{in}}(x)$, in the real space, $H_{\text{out}}(x) = h(x) * H_{\text{in}}(x)$, or as a product of these functions in the Fourier space,

$$\hat{H}_{\text{out}}(k_x) = \hat{h}(k_x) \cdot \hat{H}_{\text{in}}(k_x), \quad (5.5)$$

where the Fourier transform is indicated with a circumflex accent. With this in mind we consider a set of j discrete intensity measurements, $I_j(x_i)$, at the Fig 5.10 multilayer output interface, being $I_j(x_i) = |H_{\text{out},j}|^2(x_i)$. We consider $j = 1 \dots 20$, and every measurement includes an image measured through a mask with two apertures. The output wavefronts $H_{\text{out},j}$ are initially assigned with a random phase distributions as a seed for the algorithm. Their amplitudes are fixed to $\sqrt{I_j(x_i)}$. The shape of each mask, $H_{\text{in},j}$, is estimated from the intensity $I_j(x_i)$.

We will iterative apply the recovering algorithm presented in Fig. 5.11. In our

simulations the number of iterations is limited to $p_{\max} = 50$ and p numbers the iterations, $p = 1 \dots p_{\max}$. In subsequent iterations, the transfer function \hat{h}_p is being estimated as the median of the estimates $\hat{h}_{p,j}$ for all the apertures. The purpose of using the median is to eliminate the values of $\hat{h}_{p,j}(k_{xi}) = \hat{H}_{\text{out},p,j}(k_{xi})/\hat{H}_{\text{in},j}(k_{xi})$ for the spatial frequencies k_x at which $\hat{H}_{\text{in},j}(k_{xi})$ has a small magnitude and may introduce noise. The median of set of complex values is understood as if these values were ordered by their absolute values. Calculation of the median makes sense only after normalization of the phase taking into account that the functions $\hat{h}_{p,j}(k_{xi})$ are assumed to be real and positive at $k_x = 0$. Then we apodize \hat{h}_p in every iteration by multiplying it by a Hamming window function of the width w_H . The Hamming window is defined as $\text{rect}(x/w_H) \cdot (a + b \cdot \cos(2\pi u/w_H))$ where $a = 0.5435$, $b = 1 - a$, and $\text{rect}(\cdot)$ is the rectangular function. In this way, the high spatial frequencies are slightly suppressed with respect to the low frequencies in every iteration. Subsequently, the complex PSF $h_{p,j}(x_i)$ is calculated. The PSF is apodized in a similar way as \hat{h}_p . In the simulations, the Hamming windows are rather broad ($w_H = 20\lambda_0$ and $w_H = 20k_0$ in the reciprocal space). Moreover h_p is forced to preserve an even symmetry in every iteration. The algorithm stops after iteration p_{\max} .

The algorithm has been tested for apertures separations always larger than λ_0 . In the simulations we use a PSF obtained with the transfer matrix method for a layered metamaterial consisting of silver and TiO_2 . The operating wavelength is equal to $\lambda_0 = 404.7$ nm, which is the line of mercury lamp. The permittivities of both materials are equal to $\epsilon_{\text{Ag}} = -3.998 + 0.692i$ [104] and $\epsilon_{\text{TiO}_2} = 6.392$ [191]. The layered metamaterial consists of $N = 7$ elementary cells, each containing three layers: two external TiO_2 layers with the thickness of $w_{\text{TiO}_2} = 22.5$ nm, and a middle silver layer with $w_{\text{Ag}} = 11$ nm. We have designed this metamaterial

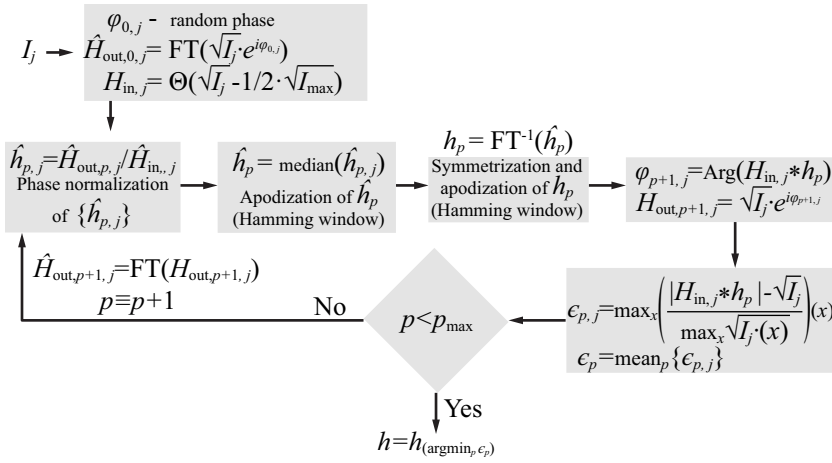


FIGURE 5.11: Modified blind deconvolution algorithm for the recovery of complex PSF

for superresolving imaging: the FWHM of $|h(x)|^2$ is subwavelength and equal to $0.2\lambda_0$.

The results of the algorithm are presented in Fig. 5.12. The figure includes one of the 20 aperture pairs with the corresponding intensity measurement, the original and reconstructed PSF and ATF, and the absolute reconstruction error of the measurement. As we can see, the algorithm is capable of retrieving an estimate for the PSF, although the result is not exact, and due to the problems with the uniqueness of the decomposition it should not be used in an automatic way. The recovered PSF visually differs from the original one, but the reconstruction error is not large. We are able to estimate the size of the PSF, and its phase near the origin. The convergence of the algorithm is characterized in Fig. 5.13.

Altogether, the proposed algorithm allows the requirements for the fabrication of the mask to be relaxed significantly. In particular the mask may be produced with

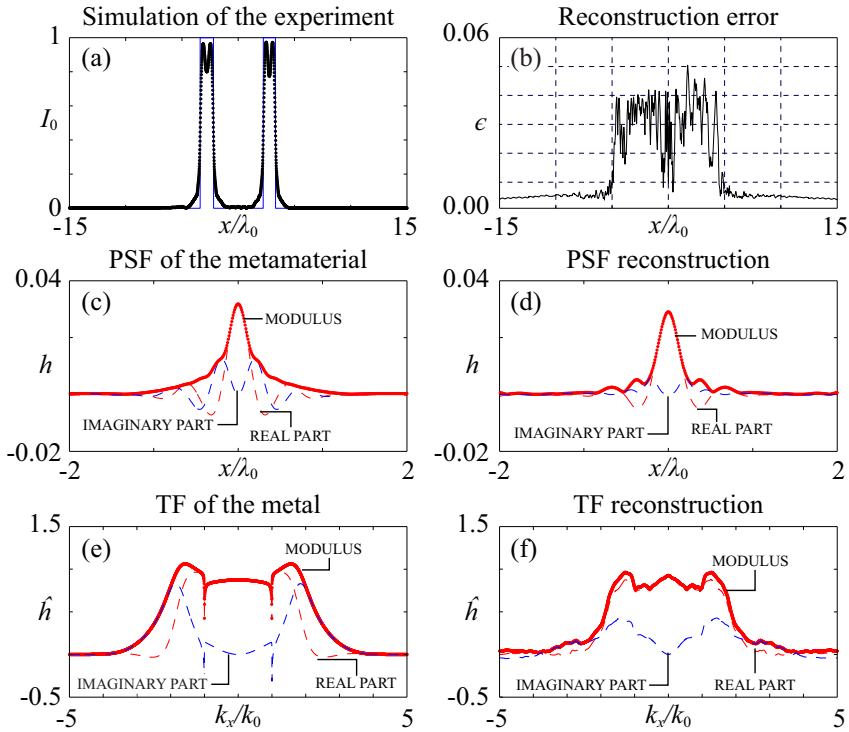


FIGURE 5.12: Modified blind deconvolution used to determine coherent PSF; (a) Intensity profile $I(x)$ superimposed on a pair of two apertures and (b) the corresponding reconstruction error obtained with the PSF recovered from the algorithm (an example chosen from 20 pairs of apertures used to determine the PSF). (c) Original and (d) recovered PSF of the metamaterial; (e) Original and (f) recovered transfer function of the metamaterial. Bold red lines stand for the absolute value of the PSF and transfer function. Dashed lines correspond to the real and imaginary parts of the same functions.

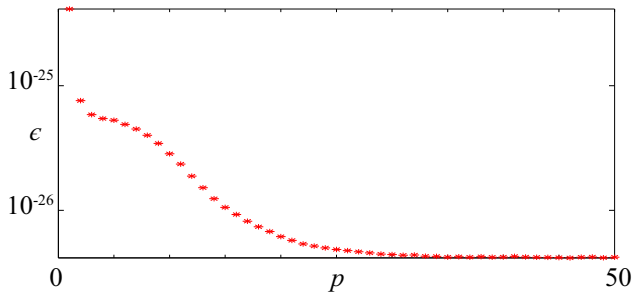


FIGURE 5.13: Convergence of the modified blind deconvolution algorithm: ϵ_p versus iteration p obtained for a set of 20 pairs of apertures

laser lithographic techniques, and still can be used to measure the PSF with a sub-wavelength resolution.

Chapter 6

Diffraction-Free Localized Wave fields

Previously the possibility of wave field propagation in metamaterials under the canalization regime has been addressed. In this Chapter we examine the Bessel beams (BBs) and the Airy beams (AiBs). They are particular solutions to the wave equation in a diffraction-free way without the support of a given structured medium.

We start by reviewing the historical background of the diffraction-free wave fields. The description of the Bessel field distribution is outlined below. More specifically, the BBs formulation is reviewed. The possibility to propagate BBs in stratified and wire media are also discussed. When including metallic nanoelements, the plasmon resonances will sustain high-frequency field contribution inside the

medium allowing BBs with sizes under the diffraction limit. The intensity patterns produced in the nanostructures are also analyzed with a view to the imaging formation.

Finally we will consider AiBs as candidates to transport subwavelength information through nanostructures under widely general conditions. Contrary to the BBs, it is straightforward to excite it in a planar metal-dielectric interface. We will pay special attention to the relevance of the Gouy phase in the AiBs. For the sake of completeness, AiBs propagating inside plasmonic nanostructures will be finally reviewed, focusing in the experimental achievements on this topic.

6.1 Introduction to Bessel Beams

Common beams suffer from diffraction, which spoils the transverse shape of their field, widening it gradually during propagation. It was generally believed that the only adiffractive wave was the plane wave, which does not undergo any transverse change. As early as 1941 Stratton discovered “limited diffraction” solutions to the wave equations and, in particular, to Maxwell’s equations under weak hypotheses [192], experimentally confirmed later by Durnin in 1987 [193, 194]. They have been constructed mathematically in more recent times [195] and soon after produced experimentally [196], as illustrated in Fig. 6.1. These beams have an infinite depth of field, i.e., they can propagate to an infinite distance without changing their wave shape. Durnin termed these beams “nondiffracting beams” or “diffraction-free beams”. They are also called Bessel beams because their transverse beam profile is a Bessel function [193].

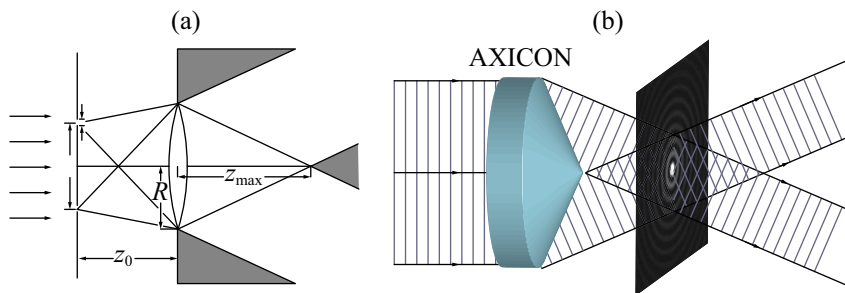


FIGURE 6.1: (a) First set up on generating BBs reprinted from [194]. (b) Schematic for the generation of a BB with an axicon.

An interesting topic is what would happen to the ideal BB solution when truncated by a finite transverse aperture. Not until 1987 an heuristic answer came from an actual experiment, when Durnin et al. [194] shown experimentally that the transverse intensity peak as well as the field surrounding it do not undergo any appreciable change in shape for much longer than its *Rayleigh range*. Further than this distance the intensity decays abruptly [193, 197, 198].

Bessel beams have many potential applications due to its limited diffraction. They have been studied extensively both in optics [193, 194, 199] and acoustics. Applications include medical imaging [200], tissue characterization [201], Doppler velocity estimation [202], and non-destructive evaluation of materials [203]. Restricting ourselves to electromagnetism, there are studies on EM tweezers [204–207], optical scalpels, optical guiding of atoms or corpuscles (charged or neutral) [208–210], optical lithography [204, 211], optical imaging [197], communications in free space [212, 213], remote optical alignment [198] among others.

The self-healing property that is the self-reconstruction of the wave form after interacting with an obstacle plays a relevant role in numerous applications, such as the optical manipulation of micro-sized particles [204], the fabrication of long polymer fibers induced by the photopolymerization [214] and microchanneling by

structural modification in glass materials [215], the enhancement of energy gain in inverse free electron lasers and inverse Cerenkov accelerators [216], and the generation of Bessel photonic lattices imprinted in photorefractive crystals [217].

The possibility of independently tuning the phase and group velocities of a BB opens the possibility of a number of applications in nonlinear optics. In particular, a number of phenomena was observed: frequency-doubling [218] and high-order harmonics in the extreme ultraviolet [219] using BBs, resonant self-trapping of BBs in plasmas [209], the spontaneous formation of unbalanced BBs during ultrashort laser pulse filamentation in Kerr media [220], and high Raman conversion efficiency in the formation of group velocity-matched X-wave pulses [221].

Fast development of plasmonics has propelled the irruption of BBs on the stage, with the excitation of SPPs in several applications. Kano et al. reported the first experimental result concerning an efficient excitation of local SPPs, by using the zeroth-order BB [222]. Specifically, radially-polarized BBs provide the p -polarized waves required for the effective coupling to the SPPs [223–225]. This type of BB can not be considered as a nondiffracting beam, i.e., the inherent anisotropy of the strati-formed media prevents the BB maintaining its intensity all along the direction of propagation. Evanescent BBs can be used as a virtual probe for the two-photon fluorescence microscopy [226]. Evanescent BBs have been observed also in all-dielectric stratified structures [227–233].

6.1.1 Basic Bessel-Beam Formulation in Free Space

Bessel beams traveling in free space are characterized by a prescribed propagation constant along a given direction and concurrently their transverse patterns are

clearly localized. As shown by Durnin [193], the free space wave equation

$$\left(\nabla^2 - \frac{1}{c^2} \frac{\partial^2}{\partial t^2}\right) \psi(\mathbf{r}, t) = 0, \quad (6.1)$$

has in polar coordinates the exact solution

$$\psi(\mathbf{R}, z \geq 0, t) = \int_0^{2\pi} \mathcal{A}(\varphi) e^{i\mathbf{k}(\varphi)\mathbf{r}} d\varphi = e^{i(k_z z - \omega t)} \int_0^{2\pi} \mathcal{A}(\varphi) e^{i\mathbf{k}_\perp(\varphi)\mathbf{R}} d\varphi, \quad (6.2)$$

for a scalar field ψ propagating with velocity c into a source-free region $z \geq 0$. Due to the cylindrical symmetry in Eq (6.2) we consider that the wave vector is explicitly $\mathbf{k} = \mathbf{k}_\perp + k_z \hat{z}$ and $\mathbf{r} = \mathbf{R} + z\hat{z}$. The axial z dependence on the wave field is thus separated from the transverse coordinates, \mathbf{R} . When k_z is real, the solution represents a nondiffracting field in the sense that the time-averaged intensity $|\psi(\mathbf{r}, t)|^2$ is independent of z . Since in the domain of spatial frequencies the wave vectors of the constitutive plane waves were wrapped around a conical surface, similar to the Cerenkov radiation, this lead to a new appellation of conical waves, employed a few times by some authors.

The spectral distribution $\mathcal{A}(\varphi)$ in Eq. (6.2) represents an arbitrary complex function of the angular coordinate φ . For solutions with complete axial symmetry, $\mathcal{A}(\varphi) = \mathcal{A}_0$, and the nondiffracting scalar field solution may be written:

$$\psi(\mathbf{r}, t) = 2\pi \mathcal{A}_0 e^{i(k_z z - \omega t)} J_0(k_\perp R), \quad (6.3)$$

where J_0 , is the zero-order Bessel function of the first kind. If $k_\perp = 0$, the solution of Eq. (6.3) reduces to a plane wave travelling in the positive z direction. For $0 \leq k_\perp \leq \omega/c$, the solution represents a nondiffracting beam like the one from Fig. 6.2 whose intensity profile radially decreases with increasing R .

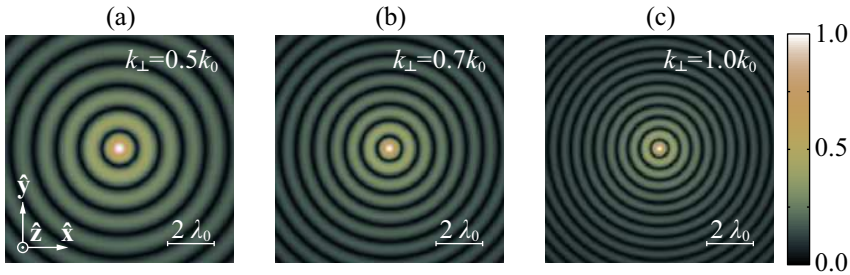


FIGURE 6.2: Bessel beams intensity profile at an arbitrary z plane and (a) $k_{\perp} = 0.5k_0$, (b) $k_{\perp} = 0.7k_0$, (c) $k_{\perp} = k_0$

The amount of energy contained in each lobe of the zero-order Bessel distribution is roughly equal to the amount of energy contained in the central peak [193, 234], and it would require an infinite amount of energy to create a nondiffracting J_0 Bessel beam over an infinite plane. Use of an aperture to restrict the radial extent of the beam eliminates the infinite energy concern, but introduces edge diffraction effects which cause the beam to spread.

6.2 Plasmonic Bessel Beams

Bessel beam size is unambiguously limited by diffraction inasmuch as its FWHM is greater than half the wavelength. Transferring the idea of a BB to diffraction-free optically structured media is strikingly easy to do [235]. The assistance of surface plasmons polaritons in these media leads to subwavelength beamsizes. Since a host medium cannot route a wave field by definition, confined nondiffracting beams may be interpreted as a tight focusing within bulk inhomogeneous media.

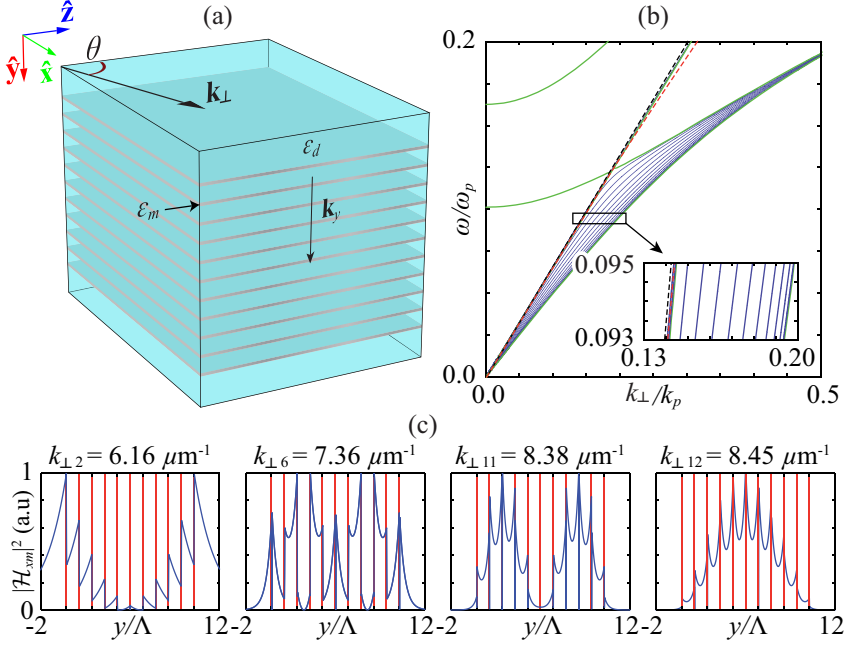


FIGURE 6.3: (a) Geometry of the multilayered nanostructure; thin silver nanomembranes of $w_m = 10$ nm are impressed into fused silica $\epsilon_d = 2.25$ at a rate of $3.33 \mu\text{m}^{-1}$. (b) Blue dispersion curves of guided modes for $N = 11$. Dashed red line is the dispersion of ordinary SPP; dashed black line is the light line of the dielectric material; green lines represent bandgap edges of unbounded periodic medium. The inset shows the multi-modal dispersion in detail. (c) Intensity distribution $|\mathcal{H}_{xm}|^2$ for several modal solutions at $\lambda_0 = 1.55 \mu\text{m}$.

6.2.1 Plasmonic Bessel Beams in Stratified Media

Let us first consider a monochromatic surface wave propagating with a wave vector \mathbf{k} in a MD multilayered structure consisting of a finite number of metallic layers, N , and $N - 1$ slabs of a dielectric material. The layers are alternatively placed and stacked around a solid cladding, as shown in Fig. 6.3(a). The widths of the metallic slabs and the dielectric slabs are denoted by w_m and w_d . The y axis is set

perpendicular to the MD interfaces. A discrete function $\varepsilon(y)$ characterizes the relative dielectric constant of the stratified medium. Particularly, it takes a real value ε_d in the dielectric films and a complex ε_m in the metallic layers. Material properties of metals can be appropriately described by the Drude-Lorentz model, from which the frequency-dependent permittivity follows the formula (2.15). We consider the plasma frequency $\omega_p = 12.9 \text{ fs}^{-1}$ and the damping factor $\gamma = 0.08 \text{ fs}^{-1}$ for silver. Without loss of generality we assume that ε_d also denotes the dielectric constant of the cladding.

A MD stratified medium commonly provides a number of EM field modes, which we identify by an index $m = \{1, 2, \dots, M\}$. For convenience, we cast the magnetic field of each plasmonic mode as

$$\mathbf{H}_m(x, y, z) = \mathcal{H}_m(y) \exp[ik_{\perp m}(z \cos \theta_m + x \sin \theta_m)], \quad (6.4)$$

where $k_{\perp m}$ is the wavenumber of the m th-order surface mode and θ_m determines its in-plane direction of propagation. Furthermore, in order to excite surface resonances in the interfaces of our device, p -polarized waves should be employed. Finally, the problem may be fully described in terms of the scalar wave field \mathcal{H}_{xm} , from which other EM components may be derived.

Using the standard matrix formulation for isotropic layered media, we can describe unambiguously the amplitude $\mathcal{H}_{xm}(y)$ distributed inside our device. For a large number, N , of metallic strata the periodic medium operates just as a photonic lattice whose unit cell p -polarization translation matrix is here denoted by $\overline{\overline{M}}_{p,\text{cell}}$. For an ideally unbounded photonic crystal with lattice period $\Lambda = w_d + w_m$ the Bloch wavenumber of the m th surface plasmon, K_m , is characterized by the dual of Eq. (3.9). It should be stressed that in this equation the Bloch wavenumber,

K_m , stands for the component of the wave vector of the periodic media in the direction of the periodicity, y , by contrast with definitions given in the previous chapters. Due to the periodicity, the values of $k_{\perp m}$ are restricted to allowed bands, as depicted in Fig. 6.3(b). In the case presented we neglected material losses, thus $\overline{M}_{p,\text{cell}}$ became unimodular. Since the periodic structure is finite, solutions are derived from the equation $[(\overline{M}_{p,\text{cell}})^N]_{11} = 0$.

We have considered an structure with $N = 11$ periods like the one displayed in Fig. 6.3(a). A discrete set of $M = 12$ surface modes where obtained. The modal field decays exponentially in the limit $|y| \rightarrow \infty$ and it may vary substantially within the stratified medium, as shown in Figure 6.3(c). However, these surface waves are homogeneous in the xz plane, as shown in Eq. (6.4). In general, the larger the number N of layers, the higher the number $M = \max(m)$ plasmonic modes sustainable in such a MD nanostructure.

Strictly speaking, the homogeneous surface wave disclosed in Eq. (6.4) represents a nondiffracting beam whose propagation constant $k_{\perp m}$ is governed by the MD multilayer. However, we may freely modify the spatial frequency $k_z \geq 0$ along the beam axis of a nondiffracting SPP (here taken to be the z axis) provided $k_z \leq k_{\perp m}$. For that purpose we consider the superposition of two homogeneous surface plasmons of the same wavenumber $k_{\perp m}$, but different directions of propagation, given by the angles $+\theta_m$ and $-\theta_m$ respectively, as shown in Fig. 6.4(a). The projections of the wave vectors onto the z axis coincide with $k_z = k_{\perp m} \cos \theta_m$. Assuming additionally that both plasmonic modes become equal in strength $|\mathcal{H}_{xm}|$, the net flux power along the x axis is zero. The resultant field $\mathcal{H}_{xm} = \mathcal{H}_{xm}(y) \exp(ik_z z) \cos(k_{xm}x + \phi_m)$ yields Young fringes whose maxima are controlled by the spatial frequency $k_{xm} = k_{\perp m} \sin \theta_m$ and the dephasing ϕ_m of the surface plasmons (see Fig.6.4(b)).

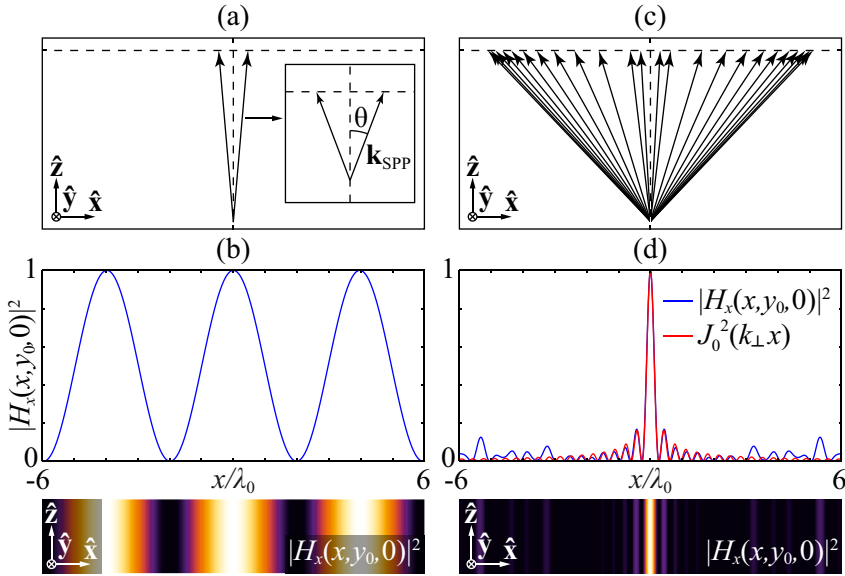


FIGURE 6.4: Formation of a nondiffracting cosinusoidal beam mediated by SPPs on a silver-fused silica interface: (a) Sketch of the wave vectors distribution and (b) contours of intensity $|H_x|^2$ in the xz plane at $\lambda_0 = 1.55 \mu\text{m}$. Excitation of multiple high-order SPPs is schematically represented in (c) using here every high-order SPP involved. (d) Intensity distribution in the xz plane running with $M = 12$ modes. The quadrature from Eq. (6.5) on the surface $y = y_0$ is performed for a Bessel function of $k_\perp = 5.90 \mu\text{m}^{-1}$ shown in red. The propagation constant is $k_z = 6.12 \mu\text{m}^{-1}$ in (b) and (d).

The nondiffracting sinusoidal beam driven by monomode SPPs is clearly unconfined [236]. Note that such a wave interference is practicable for any order m of the mode. Therefore, we may conceive a coherent superposition of plasmonic cosine waves exhibiting the same propagation constant k_z along the z axis, provided that $k_z \leq k_m$ for all m involved. This condition fixes the values of θ_m , as outlined in Fig.6.4(c) for the twelve distinct SPPs. Moreover, localization around the beam axis, set on a given MD interface $y = y_0$ at $x = 0$, is achieved by adapting the

individual dephases in such a way that $\phi_m = 0$, giving

$$H_x = \exp(ik_z z) \sum_{m=1}^M \mathcal{H}_{xm}(y) \cos(k_{xm} x). \quad (6.5)$$

The superposition proposed in Eq. (6.5) is not enough by itself to generate a localized wave field inside the MD device. For that purpose we manipulate the amplitudes $\mathcal{H}_{xm}(y_0)$ in order to match their phases at the beam axis. Furthermore, we seek for values of $\mathcal{H}_{xm}(y_0)$ leading to a field $H_x(x, y_0, 0)$ to trace a Bessel profile. We may express the zeroth-order Bessel function as

$$J_0(k_{\text{cut}} x) = \frac{2}{\pi} \int_0^{k_{\text{cut}}} \frac{1}{\sqrt{k_{\text{cut}}^2 - k_x^2}} \cos(k_x x) dk_x. \quad (6.6)$$

For convenience we assume that the arbitrary frequency k_{cut} is higher than any k_{xm} involved. Our procedure is based on the fact that the integral (6.6) approaches the series expansion (6.5) given at $(x, y_0, 0)$ by means of a numerical quadrature with preassigned nodes k_{xm} [237]. The solutions $\mathcal{H}_{xm}(y_0) = 2/(\pi \sqrt{k_{\text{cut}}^2 - k_x^2}) \int L_m(k_x) dk_x$ of the quadrature, expressed in terms of the Lagrange polynomials L_m , provide a wave field through Eq.(6.5) whose intensity on the MD interface is approximately $J_0^2(k_{\text{cut}} x)$. The resulting field is here called the nondiffracting Bessel plasmon, which is depicted in Fig. 6.4(d) using all $M = 12$ modes involved at $\lambda_0 = 1.55 \mu\text{m}$. The central part of the waveform is accurately represented by the Bessel function, whose highest main peak has an intensity FWHM $\Delta_x = 0.38 \mu\text{m}$. The error visible in the wings comes from difference between the finite series expansion and the integral involving Bessel function.

After following the procedure given above, the oscillatory superposition (6.5) yields the highest intensity achievable at $x = 0$ on the MD surface $y = y_0$. Under ordinary conditions it will not be found at a point out of the beam axis, where

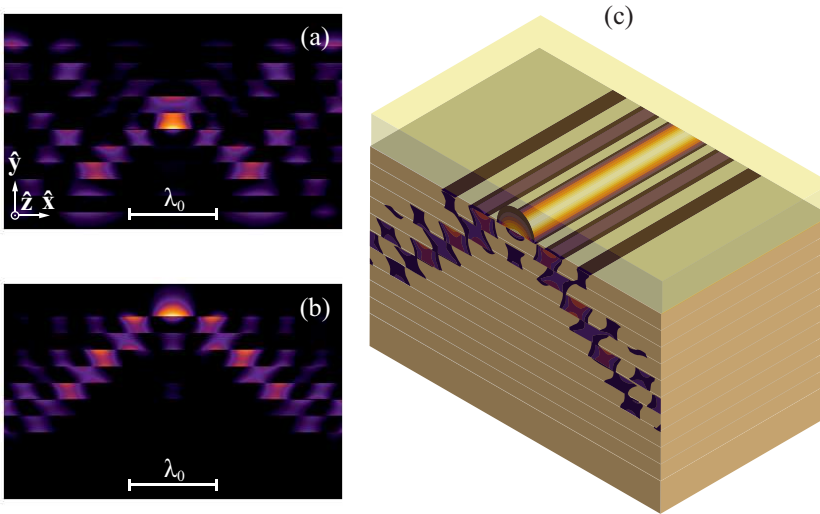


FIGURE 6.5: (a) Intensity pattern of the nondiffracting Bessel plasmon in the xy plane for a phase matching at the top surface of the central layer. (b) The same as in (a) for a phase matching at the uppermost MD interface. (c) 3D view of the multilayered device and the surface BB generated in (b).

such a phase matching holds. As a consequence, a strong confinement of the plasmonic BB is expected to occur around $(x, y) = (0, y_0)$.

In Fig. 6.5 we represent $|H_x|^2$ derived from Eq. (6.5) when the phase matching is boosted at different surfaces of the metal-dielectric nanostructure. In Fig. 6.5(a) the phase matching is accomplished on the interface that belongs to the central silver film. For convenience we discarded 5 plasmonic modes with index $m = \{1, 2, 7, 9, 11\}$, which induced a field localization out of the beam axis. The numerical quadrature was set for the BB that has a transverse frequency $k_{\text{cut}} = 5.90 \mu\text{m}^{-1}$. The anisotropic spot displays a subwavelength FWHM $\Delta_y = 160 \text{ nm}$ along the y axis, and an in-plane FWHM $\Delta_x = 416 \text{ nm}$. In Fig. 6.5(b) the beam axis is relocated on the boundary of the MD device and the cladding. In this case we employed 8 different surface modes (from $m = 1$ to $m = 8$) for the Bessel quadrature, with $k_{\text{cut}} = 5.20 \mu\text{m}^{-1}$. As a consequence, the FWHM $\Delta_x = 430 \text{ nm}$

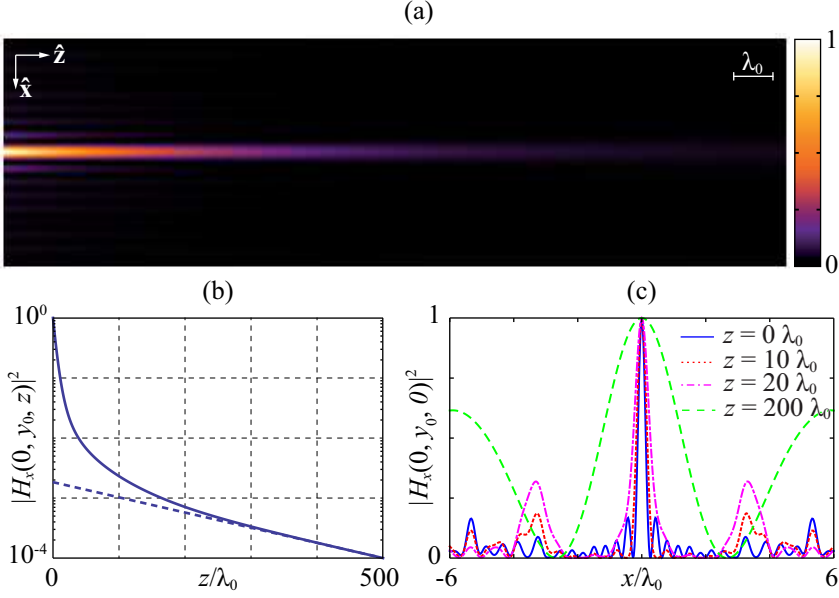


FIGURE 6.6: Numerical experiment with $\gamma = 0.08 \text{ fs}^{-1}$ for silver. (a) Surface distribution of the initiated BB in the xz plane. (b) Evolution of the intensity along beam axis. The dashed line represents the asymptotic behavior of the on-axis intensity that is valid when a single long-range SPP contributes effectively in Eq. (6.5). (c) Transverse intensity distribution normalized at the beam axis for different propagation distances.

results in a slightly higher value than that obtained above, otherwise $\Delta_y = 113 \text{ nm}$. This is also illustrated in Fig. 6.5(c) by means of the full 3D arrangement. Note that the transverse wave field in (a) is essentially different from (b), in spite of using roughly the same in-plane Bessel distribution.

The control of the field is initially established in the xz plane, however, out-of-plane intensity is determined by the geometry and materials composing the multi-layered waveguide. The Bessel-like distribution along the x axis cannot be maintained in other directions, due to the intrinsic anisotropy of the stratified medium. Moreover, the field of the Bessel plasmon is enhanced along distinctive paths in the transverse xy plane.

Purely diffraction-free Bessel plasmons described above exist assuming an ideal conductor with $\gamma = 0$. Therefore, we consider now the case when γ in Eq. (2.15) is no longer zero and with it the SPP propagation constant $k_{\perp m}$ becomes complex. The traveling SPPs are damped with an evanescent decay length l_m . As a consequence, the nondiffracting nature plasmonic BBs is preserved, but each m th-order SPP contributing in the summation of Eq.(6.5) runs a distance shorter than its propagation length l_m . This effect is illustrated in Fig. 6.6(a). The phase fronts of the field H_x advance with a constant velocity, provided $k_z = \text{Re}(k_{\perp m}) \cos \theta_m$ is conserved. The modal angle θ_m brings to effect that each causal plasmonic signal travels its own distance l_m , to reach the beam axis at the z axis coordinate $l_m / \cos \theta_m$. In our numerical simulation $l_1 = 267 \mu\text{m}$, $l_2 = 45.0 \mu\text{m}$, and l_m decreases fast at higher m , up to $l_{11} = 3.09 \mu\text{m}$ and $l_{12} = 3.06 \mu\text{m}$; however $\theta_m \ll 1$ leading to an incessant drop of higher m th-order terms taking part in the summation in Eq.(6.5). Consequently, the on-axis intensity is reduced by a factor $1/e$ at $z = 6.8 \mu\text{m}$, as shown in Fig. 6.6(b), which is primarily determined by the evanescent decay length of the highest-order SPPs. Fig. 6.6(c) elucidates how the Bessel profile of the nondiffracting plasmon evolves toward a cosine amplitude distribution. This evidences that the 1st-order sinusoidal SPP contributes exclusively to the wave superposition (6.5) at sufficiently long distances. We reported the results of this Section in Refs. [238, 239].

6.2.2 Plasmonic Bessel Beams in Wire Media

Diffraction-free localized solutions of Maxwell's equations can also be found in a wire media. Let us first consider metallic wires of radius r_0 , made of a bulk metal with permittivity ϵ_m . We assume a periodic squared distribution of this sort of wires in a way that stands for the lattice period, as shown in Fig. 6.7.

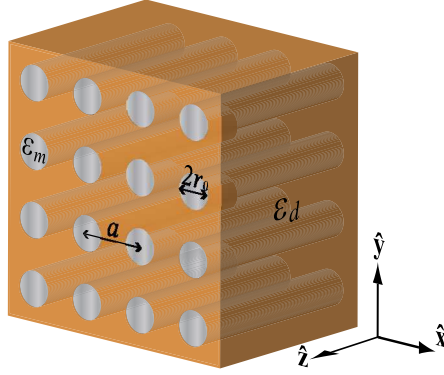


FIGURE 6.7: Periodic array of nanowires made of a metal with dielectric constant ϵ_m , distributed in a squared lattice, and hosted in a dielectric medium with permittivity ϵ_d . The radius of the wires is r_0 and the lattice period is a . Beam propagation is driven along the wires axes, that is the z axis.

Note that $a \geq 2r_0$. Finally, the host medium has a dielectric constant ϵ . Also we assume that monochromatic beam propagation is driven along the wires, that is the z axis. If, additionally, the transverse waveform does not change at different xy planes, except maybe by a phase-only term depending on z , we may impose simultaneously that $\partial_z \mathbf{H} = ik_z \mathbf{H}$ and $\partial_t \mathbf{H} = -i\omega \mathbf{H}$, where k_z is the on-axis spatial frequency of the wave field. For convenience, the 3D magnetic field is written as $\mathbf{H} = \mathbf{H}_\perp + H_z \hat{\mathbf{z}}$, where \mathbf{H}_\perp includes both transverse components and H_z consider the on-axis component. Under these conditions, H_z satisfies the following wave equation,

$$(\epsilon k_0^2 - k_z^2 + \nabla_\perp^2) H_z = \epsilon (\nabla_\perp \epsilon^{-1}) \cdot (ik_z \mathbf{H}_\perp - \nabla_\perp H_z). \quad (6.7)$$

Here $\nabla_\perp = \partial_x \hat{\mathbf{x}} + \partial_y \hat{\mathbf{y}}$ and $\nabla_\perp^2 = \partial_x^2 + \partial_y^2$. In our system, a given wire axis is parallel to the unit vector $\hat{\mathbf{z}}$; therefore we set $\epsilon(x, y) = \epsilon_d$ in the metallic rods and $\epsilon(x, y) = \epsilon_m$ in the host medium.

We may simplify our problem by considering the EMA. Under this approach, the

structured medium is modeled as an anisotropic material. The EMA gives accurate results provided that the wavelength is significantly greater than the lattice period, $\lambda_0 \gg a$. As a consequence, $\varepsilon(x, y)$ in Eq. (6.7) is transformed into an average constant parameter, ε_\perp , which is given by

$$\varepsilon_\perp = \varepsilon_d \left[\frac{(1+f)\varepsilon_m + (1-f_m)\varepsilon_d}{(1-f_m)\varepsilon_m + (1+f_m)\varepsilon_d} \right], \quad (6.8)$$

where the filling factor $f_m = \pi r_0^2/a^2$. Here we use the expression for ε_\perp from the Maxwell-Garnett theory [240]. Moreover, Eq. (6.7) is reduced to a 2D Helmholtz equation, $(k_\perp^2 + \nabla_\perp^2)H_z = 0$, where $k_\perp = \sqrt{k_0^2\varepsilon_\perp - k_z^2}$ provided that $\varepsilon_\perp > 0$ and $k_z < \sqrt{\varepsilon_\perp}k_0$. This is a wave equation corresponding to nondiffracting ordinary waves propagating in a uniaxial crystal of permittivity $\bar{\varepsilon} = \varepsilon_\perp(\hat{\mathbf{x}}\hat{\mathbf{x}} + \hat{\mathbf{y}}\hat{\mathbf{y}}) + \varepsilon_\parallel\hat{\mathbf{z}}\hat{\mathbf{z}}$. Solutions using Bessel functions come out naturally by setting ∇_\perp^2 in a cylindrical coordinate system, that is, $\nabla_\perp^2 = R^2\partial_R^2 + R\partial_R + \partial_\varphi$. Solving the Helmholtz wave equation yields

$$H_z^o = \exp(ik_z z - i\omega t) \frac{k_\perp}{k_z} \sum_{m=-\infty}^{\infty} \mathcal{H}_m^o \psi_m(R, \varphi), \quad (6.9)$$

where \mathcal{H}_m^o denotes a complex-valued constant, $\psi_m = \exp(im\varphi)J_m(k_\perp R)$ and J_m is a Bessel function of the first kind. Equation (6.9) gives a complete solution provided that H_z^o does not diverge at $R = 0$. In this case, the transverse components of the magnetic field are written as

$$\mathbf{H}_\perp^o = \exp(ik_z z - i\omega t) \sum_{m=-\infty}^{\infty} \mathcal{H}_m^o [(i\psi_{m+1} - i\psi_{m-1})\hat{\mathbf{x}} + (\psi_{m+1} + \psi_{m-1})\hat{\mathbf{y}}]. \quad (6.10)$$

Let us point out that non-trivial solutions of Maxwell's equations exist involving $H_z^e = 0$. These solutions are associated with extraordinary waves, whose magnetic

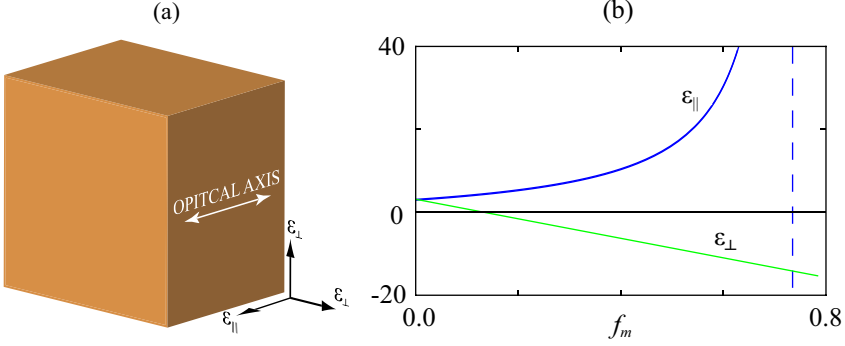


FIGURE 6.8: (a) Schematic illustration of the anisotropic medium that substitutes the wire plasmonic crystal of Fig. 6.7 by using the Maxwell-Garnett model. (b) Variation of ϵ_{\perp} and ϵ_{\parallel} in terms of the filling factor, for silver wires hosted by alumina at $\lambda_0 = 700$ nm

field may be written as

$$\mathbf{H}_{\perp}^e = \exp(ik_z z - i\omega t) \sum_{m=-\infty}^{\infty} \mathcal{H}_m^e [(i\psi_{m+1} + i\psi_{m-1})\hat{\mathbf{x}} + (\psi_{m+1} - \psi_{m-1})\hat{\mathbf{y}}], \quad (6.11)$$

where \mathcal{H}_m^e stands for a complex-valued constant. Now the transverse spatial frequency satisfies $k_{\perp}^2 = \epsilon_{\parallel} k_0^2 - k_z^2 \epsilon_{\parallel} / \epsilon_{\perp}$, where [240]

$$\epsilon_{\parallel} = f_m \epsilon_m + (1 - f_m) \epsilon_d. \quad (6.12)$$

Some general conclusions may be inferred assuming that $\epsilon_d < |\epsilon_m|$ for visible and infrared frequencies. For numerical purposes we will consider silver and alumina; the permittivities of silver and alumina at the wavelength in vacuum $\lambda_0 = 700$ nm are $\epsilon_{\text{Ag}} = -20.4$ (neglecting losses) and $\epsilon_{\text{Al}_2\text{O}_3} = 3.1$, respectively, taken from experimental data [241]. First of all, note that $0 \leq f_m \leq f_{\text{max}}$ provided that $a \geq 2r_0$, where $f_{\text{max}} = \pi/4 \approx 0.78$. On the other hand, $\epsilon_{\parallel} > 0$ for relatively low values of

the filling factor,

$$0 \leq f_m < \frac{\varepsilon_d}{\varepsilon_d - \varepsilon_m}. \quad (6.13)$$

With the considered, Eq. (6.13) yields $0 \leq f_m < 0.132$. On the contrary, ε_{\perp} is maintained positive for higher filling factors,

$$0 \leq f_m < \frac{\varepsilon_m + \varepsilon_d}{\varepsilon_m - \varepsilon_d}, \quad (6.14)$$

which results $0 \leq f_m < 0.737$ for our metal-dielectric composite. Figure 6.8 shows that ε_{\perp} may take extremely-high positive values in the interval $0.132 \leq f_m < 0.737$, where ε_{\parallel} is negative. Note that BBs driven by ordinary waves, which are formulated in Eq. (6.10), cannot exist if $k_z > \sqrt{\varepsilon_{\perp}}k_0$. At the same time, the hyperbolic dispersion of extraordinary waves leads to BBs that may have a propagation constant of ideally any positive value, $0 \leq k_z < \infty$. However, it depends strongly on the sign of ε_{\perp} . For instance, if $\varepsilon_{\parallel} > 0$ then $k_z < \sqrt{\varepsilon_{\perp}}k_0$ for the existence of extraordinary waves. On the contrary, solutions involving $k_z > \sqrt{\varepsilon_{\perp}}k_0$ are consistent with EMA provided $\varepsilon_{\parallel} < 0$ (and obviously $\varepsilon_{\perp} > 0$). Furthermore, for sufficiently high values of k_z we find that $k_{\perp} \gg k_0$, since $k_{\perp} \approx k_z \sqrt{|\varepsilon_{\parallel}|/\varepsilon_{\perp}}$. Therefore the spot size of the BB clearly surpasses the limit imposed by diffraction, leading to subwavelength nondiffracting beams.

In Fig. 6.9(a) we plot H_x^e taken from Eq. (6.11) and in Fig. 6.9(b) and (c) we represent H_x^o from Eq. (6.10) for BBs propagating with $k_z = 0.8k_0$, that is $k_z = 7.18 \mu\text{m}^{-1}$. For Figs. (a) and (b) we consider a silver-alumina composite with a filling factor $f_m = 0.1$; in this case the Maxwell-Garnett model provides the permittivities $\varepsilon_{\perp} = 4.07$ and $\varepsilon_{\parallel} = 0.75$. Since both permittivities are positive, dispersion associated with extraordinary waves is ellipsoidal. To evaluate H_x^e we use $\mathcal{H}_1^e = -i/2 = \mathcal{H}_{-1}^e$, leading to BBs with transverse spatial frequency

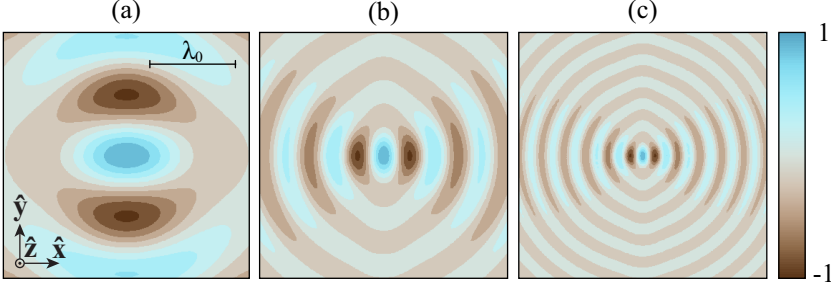


FIGURE 6.9: x -component of the magnetic field \mathbf{H} for BBs associated with (a) extraordinary and (b) ordinary waves propagating in a silver-wire medium hosted by alumina ($f = 0.1$) for $k_z = 0.8k_0$. We represent the instantaneous fields H_x^e for $\mathcal{H}_1^e = -i/2 = \mathcal{H}_{-1}^e$ and H_x^o for $\mathcal{H}_1^o = i/2 = -\mathcal{H}_{-1}^o$ at $(x, y, z) = (0, 0, 0)$. In (c) we plot H_x^o for $f = 0.5$. Boxes dimensions of the contour plots are $2 \mu\text{m} \times 2 \mu\text{m}$.

$k_{\perp} = 7.12 \mu\text{m}^{-1}$. This fact results in a central hot spot whose FWHM is 622 nm along the x axis. On the other hand, the amplitudes $\mathcal{H}_1^o = i/2 = -\mathcal{H}_{-1}^o$ are set for H_x^o . In this case $k_{\perp} = 16.6 \mu\text{m}^{-1}$ leading to superresolving hot spots of 146 nm-FWHM on the x direction. However, this effect is slightly weaker along the y axis, as shown in Fig. 6.9(b). If now we increase the filling factor up to $f = 0.5$, but maintaining the propagation constant k_z fixed, we observe that no extraordinary waves may be found. It is caused by the negative value of $\varepsilon_{\parallel} = -8.67$. In contrast, ordinary waves with extremely-high spatial frequency $k_{\perp} = 35.4 \mu\text{m}^{-1}$ are obtained in virtue of the giant (and positive) value of $\varepsilon_{\perp} = 16.2$. Figure 6.9(c) depicts H_x^o in this case, providing a central peak whose FWHM is 69 nm along the x axis. This fact demonstrates that our BB clearly features a subwavelength hot spot.

Now we will compare the above analytical approach obtained from the EMA for the periodic squared array of nanowires with the results of solving numerically the Maxwell's equations. According to the Floquet-Bloch theorem, the magnetic field of a wave mode in a 2D periodic medium with invariant spatial frequency k_z

along the z axis may be written in the form

$$\mathbf{H} = \mathcal{H}_m^{\text{Bloch}}(x, y) \exp(ik_z z - i\omega t) \exp(i\mathbf{k}_{\perp m} \cdot \mathbf{R}), \quad (6.15)$$

where $\mathcal{H}_m^{\text{Bloch}}(x, y)$ is a field with the same periodicity of the medium associate to a plane wave with $\mathbf{k}_{\perp m}$. Nondiffracting beams propagating in wire media may be expressed as a linear combination of the wave modes given in Eq (6.15). Therefore we focus on solving the Maxwell's equations to find all $\mathbf{k}_{\perp m}$ and $\mathcal{H}_m^{\text{Bloch}}$ provided that the propagation constant k_z is a parameter in our problem. For that purpose we used a commercial finite-element package (COMSOL Multiphysics). In particular, a routine was programmed in the COMSOL RF module that allows to obtain every Bloch mode for a fixed value of k_z . In other words, we found the complete set of pairs (k_x, k_y) , and the corresponding functions $\mathcal{H}_m^{\text{Bloch}}$, which satisfies Maxwell's equations for the prefixed k_z . This procedure let us to depict the spatial spectrum in the $k_x k_y$ -plane, which is also known as the isofrequency curve, provided a given on-axis frequency k_z .

In order to verify the validity of our previous analytical results, we start by considering a silver-alumina wire medium with $f_m = 0.1$ and metallic wires of diameter $2r_0 = 5$ nm. In this case, the lattice period is $a = 14.01$ nm. With these values, $\lambda_0 \gg a$, thus we have a configuration where the EMA is expected to give accurate results. Using our routine based on the FEM for $k_z = 0.8k_0$ we obtained the isofrequency curve shown in Fig. 6.10(a). In this case, the isofrequency curve has two branches approaching circles of radius $k_{\perp m} = 7.16 \mu\text{m}^{-1}$ and $k_{\perp m} = 16.6 \mu\text{m}^{-1}$. The variations of the radius are very small within its corresponding branch. Furthermore, these values of the modulus of \mathbf{k}_{\perp} are very near the values of $k_{\perp m}$ predicted by the EMA for the ordinary wave and the extraordinary wave. In view of

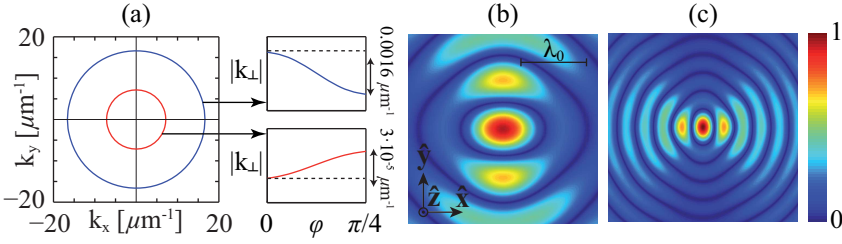


FIGURE 6.10: (a) Isofrequency curve for the silver wire medium hosted by alumina ($f_m = 0.1$) for $k_z = 0.8k_0$. Absolute value of the x -component of the magnetic field for nondiffracting beams associated with (b) extraordinary waves and (c) ordinary waves.

these results we expected to obtain nondiffracting beams with waveforms similar to those shown in Figs. 6.9(a) and (b).

In the periodic wire medium, Bloch modes will play, in some sense, the role of the plane waves in the anisotropic effective medium. Taking the results shown in Fig. 6.9(a), we would obtain an equivalent waveform by superposing properly the set of Bloch modes with in-plane k -vectors lying on the quasi-circular branch of radius $k_\perp = 7.16 \mu\text{m}^{-1}$. Note that this set contains an infinite number of modes. For numerical purposes, we have selected a finite subset of modes that are evenly spaced in the angular coordinate φ . Finally, in order to have a localized wave field around a predetermined point (x_0, y_0) , which is simply the focus of the non-diffracting beam, we set in-phase the x -component of every function $\mathcal{H}_m^{\text{Bloch}}$ at such point. In our numerical simulations we have set $(x_0, y_0) = (0, 0)$.

In Fig. 6.10(b) and (c) we plot $|H_x|$ that results from the corresponding superposition of Bloch modes. The aspect of the fields is in a good agreement with that from our analytical approach shown in Fig. 6.9(a) and (b). From Fig. 6.10(b) we estimate the FWHM along the x axis as 536 nm that is near 622 nm [from

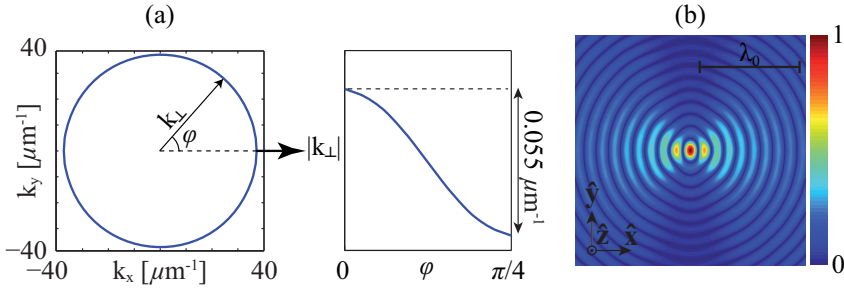


FIGURE 6.11: Isofrequency curve for a metallic compound of $f_m = 0.5$. (b) Wave field $|H_x|$ corresponding to a nondiffracting beam of $k_z = 0.8k_0$ associated with ordinary waves of the effective medium.

Fig. 6.9(a)]. Also, the FWHM is 156 nm evaluated from Fig. 6.10(c), comparable with 146 nm [from Fig. 6.9(b)].

Finally, we considered an increase of the filling factor up to $f_m = 0.5$, maintaining the propagation constant $k_z = 0.8k_0$ and the diameter $2r_0 = 5$ nm. Now, the lattice period is $a = 6.27$ nm. From our numerical FEM simulations, shown in Fig. 6.11(a), we observe that only a single ring of radius $k_\perp = 37.2 \mu\text{m}^{-1}$ remains, which is in good agreement with estimations given by the EMA ($k_\perp = 35.4 \mu\text{m}^{-1}$). Again the variation of the radius is small, however, it is one order of magnitude greater than that observed for $f_m = 0.1$. The FWHM of the central hot spot measured along the x axis is 70 nm [see Fig. 6.11(b)] that is close to 69 nm measured from Fig. 6.11(c).

6.3 Introduction to Airy Beams

In 1979 Berry and Balazs theoretically demonstrated within the context of quantum mechanics that the Schrödinger equation describing a free particle can exhibit a nonspreading Airy wave packet solution [242]. The envelope of these

wavepackets is described by the one-coordinate Airy functions, centered around a parabolic trajectory in space. This Airy packet happens to be unique, e.g., it is the only nontrivial solution (apart from a plane wave) that remains invariant with time [242, 243].

Optical Airy beams were introduced in [244], followed soon by their first experimental observation [245]. Thus, the Airy beam is essentially flat. In contrast, other types of non-diffracting solutions such as the BBs [194], Mathieu beams [246], Weber beams, are essentially functions of two coordinates, and they cannot be projected to the planar geometry. The study of Airy beams is interesting from the viewpoint of fundamental science since its intensity maxima propagate along a curved (parabolic) trajectory in a homogeneous medium, not being guided by any refractive-index gradient. The ballistic dynamics of the Airy beams, together with their facility to bypass obstacles, had been also examined [247]. Their special self-healing properties, that is, self-restoration of their canonical form after passing small obstacles, have been theoretically and experimentally demonstrated [248, 249]. It has also been shown that the linear and angular momentum of these beams change during propagation, and the total momentum and energy are conserved [250]. All these properties lead to a variety of applications for Airy beams including trapping, guiding, sorting of micro-objects [248, 251, 252], and even signal processing [253].

6.3.1 Plasmonic Airy Beams

One of the most prominent examples of a planar physical system is the evolution of waves at a metal–dielectric interface. SPPs supported by metal–dielectric interfaces can be employed to generate two-dimensional Airy beams. The plasmonic

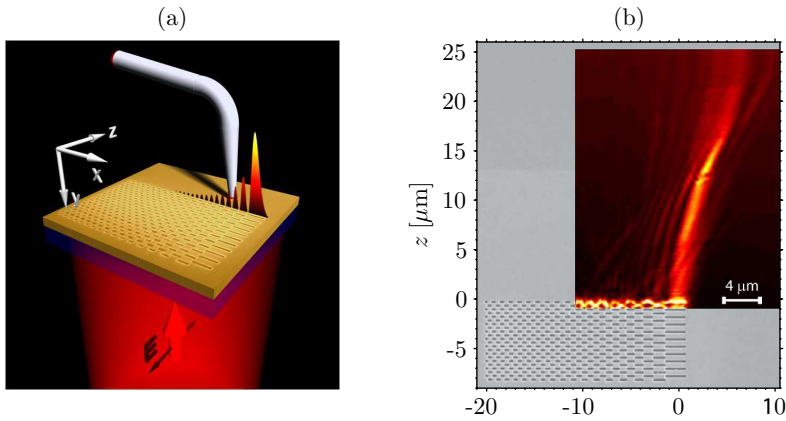


FIGURE 6.12: (a) Scanning near-field optical microscope detection of an Airy plasmon excited by a diffraction pattern at a gold–air interface ($\lambda = 0.784 \mu\text{m}$, $x_0 = 0.7 \mu\text{m}$). (b) SNOM image of the Airy plasmon superimposed with a micrograph of the diffraction pattern. Reprinted from [258].

field is tightly confined to the interface, and it decays exponentially away from it. That forms an effectively planar system with a strong subwavelength confinement [254, 255], which is very attractive for flat-land photonic applications. We note that other examples of low-dimensional systems where Airy beams can be realized include graphene [256] and thin magnetic films [257].

However, even for the near-infrared-frequency range, the propagation length of Airy plasmons at a gold–air interface is only a few tens of microns, due to the strong losses in metal. The short propagation of the SPPs presents a significant challenge for the observation and the implementation of Airy SPP beams. Nevertheless, experimental demonstrations of Airy plasmons utilizing different excitation methods were presented almost simultaneously by three different research groups [258–260]. One such experimental setups is reprinted from [258] in Fig. 6.12. Since then the research has moved into the observation of other phenomena incorporating multiple Airy beams. In this regard bottle-beams have been produced [261]. The interference of two Airy waves was also studied [262] pointing

to practical application for hot-spot creation. A hot-spot dynamically controlled by the illumination beam have been produced with the suggested set up. Dynamic control of the plasmonic Airy beams has also been explored [263–265] creating non straight propagating SPP.

For Airy plasmons a two-dimensional analogue of autofocusing was studied through the interference of two Airy waves [262], and we discuss this effect below in more detail. Further, the control of Airy plasmon trajectories was also proposed [266] and demonstrated [267] by using a linear plasmonic potential, similar to proposals for surface plasmon control using graded index elements (Luneburg and Eaton lenses) [268] as well as for free-space Airy beam manipulation [269].

In some cases it should be desirable to push the Airy plasmons to the non-paraxial regime in order to achieve a highly bent trajectory. However, the main features of non-paraxial Airy beams in free space, studied in detail in Ref. [270], are identical to what can be observed with SPPs [258].

To couple radiation to the surface waves several special techniques have been developed. One of them is prism coupling where evanescent waves are transformed to SPPs at the metal film due to a frustrated total internal reflection process. Another technique is grating coupling where the grating vector corrects the k -vector mismatch between radiation in free space and SPPs.

6.3.2 Finite-Energy Airy Beams in the Paraxial Approximation

Let us consider a $(1 + 1)$ D wave field $u \cdot \exp(ik_0z)$ which evolves along the z axis with a carrier spatial frequency k_0 . In the case that we consider plasmonic Airy

beams, k_0 should be substituted by k_{SPP} given in Eq. (2.14). Thus the wave function u satisfies the paraxial wave equation $2i\partial_\zeta u + \partial_{ss}u = 0$ expressed in terms of the normalized spatial coordinates $s = x/w_0$ and $\zeta = z/z_R$. Here w_0 is the beam width and $z_R = k_0 w_0^2$ denotes the propagation distance. Specifically, an AiB may be written as [244]

$$u(s, \zeta) = \text{Ai}(s - \zeta^2/4 + ia\zeta) \exp(as - a\zeta^2/2) \times \exp(is\zeta/2 + ia^2\zeta/2 - i\zeta^3/12), \quad (6.16)$$

where Ai denotes the Airy function. Note that

$$|u(s, \zeta)|^2 = \text{Ai}^2(s - \zeta^2/4), \quad (6.17)$$

provided that $a = 0$, and therefore the transverse intensity profile is conserved along the propagation ζ -axis. The parameter $0 < a \leq 1$ is introduced in the wave function in order to provide $\int |u|^2 ds < \infty$ allowing the paraxial beam to carry a finite energy, and concurrently conserving a central lobe with parabolic shape.

Topologic attributes of AiBs may be drawn without difficulty from its transverse spatial frequency

$$\tilde{u}(k) = \exp(-ak^2 + a^3/3 - ia^2k + ik^3/3). \quad (6.18)$$

Equation (6.16) is directly derived from the Fresnel-Kirchhoff (FK) diffraction integral $u = (2\pi)^{-1} \int \tilde{u}(k) \exp(i\psi) dk$, being $\psi = ks - k^2\zeta/2$ the phase distribution of a plane-wave spectral component with transverse spatial frequency k . The phase $\tilde{\phi} + \psi$ of the integrand is highly oscillating, where $\tilde{\phi} = \arg(\tilde{u})$. However it

reaches a stationary point, that is $\partial_k[\tilde{\phi} + \psi] = 0$, for two frequencies k_{\pm} satisfying

$$k^2 - k\zeta + s - a^2 = 0. \quad (6.19)$$

The principle of stationary phase [146] establishes that the FK diffraction integral has a predominant contribution of frequencies in the vicinities of k_{\pm} . Inside the geometrical shadow $s > a^2 + \zeta^2/4$ no stationary points may be found. In the light area, constructive interference is attained if the phase $\tilde{\phi} + \psi$ at frequencies k_+ and k_- differs by an amount $2\pi m$, where m is an integer. This condition provides the locus of points with peaks in intensity, which leads to

$$s = a^2 - (3\pi m/2)^{2/3} + (\zeta/2)^2, \quad \text{for } m \geq 0. \quad (6.20)$$

These curves describe perfect parabolas.

From geometrical grounds, the parameter k represents a particular light “ray” with linear trajectory (6.19) in the $s\zeta$ -plane. The envelope (caustic) of this family of rays results from the solution given in Eq. (6.20) for $m = 0$, providing the ballistic signature of an AiB.

In Fig. 6.13 we show the spatial distribution of the magnitude $|u|$ and the phase $\phi = \arg(u)$ of the wave function given in Eq. (6.16) corresponding to an AiB of $a = 0.1$. The accelerating behavior of the AiB is limited, and out of the near field the interference-driven parabolic peaks fade away. To establish the boundaries of the near field, we point out that $|\tilde{u}|$ falls off less than a half of its maximum in the interval $k^2 < k_{\max}^2 = \ln(2)/a$, which represents the effective bandwidth of the AiB. Moreover, k_{\max} is no more than the far field beam angle in the normalized coordinates, and $k_{\max} = 2.6$ in Fig. 6.13. As a consequence, the length of the

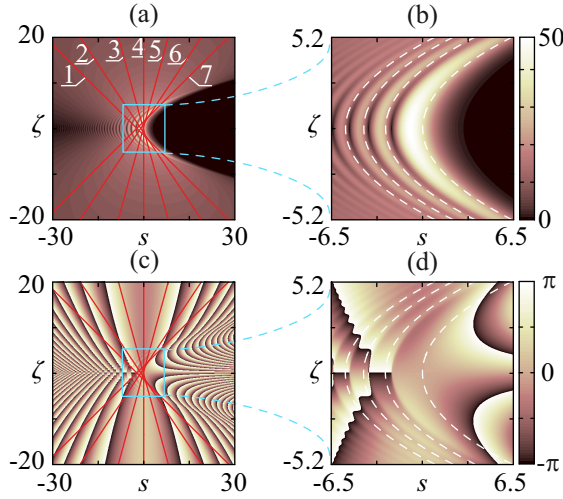


FIGURE 6.13: (a) $|u|$ and (c) ϕ for an AiB with $a = 0.1$. The parabolic curves Eq. (6.20) are drawn in the near field (b) and (d) in dashed lines. In the far field, the numbered straight trajectories of light rays satisfy Eq. (6.19)

caustic is finite and it is observed in $|\zeta| < 2k_{\max}$. Along the beam waist $\zeta = 0$ the energy is mostly localized in the region $a^2 - k_{\max}^2 \leq s \leq a^2$. In Fig. 6.13 the near field is bounded within the region $|\zeta| < 5.2$ and $|s| < 6.9$, where 4 interference peaks are clearly formed.

We point out that the maximum of intensity is not placed exactly at points that belong to the curves (6.20) but they are slightly shifted to lower values of the transverse spatial coordinate s . This effect is not caused by the finite energy of the beam since it is observed for $a = 0$, but it occurs by a non-even symmetry of its spatial spectrum (6.18).

In the far field, however, the behavior of the AiB is completely different. Applying the principle of stationary phase, no more than one spatial frequency k is of relevance. The resultant Fraunhofer pattern is $u \rightarrow (2\pi i \zeta)^{-1/2} \tilde{u}(k) u_{PW}(s, \zeta)$, valid in the limit $|\zeta| \gg k_{\max}$ for points of the contour $C \equiv s = k\zeta + a^2 - k^2$ taken from

Eq. (6.19). Note that the paraxial wave field $u_{PW} = \exp(iks - ik^2\zeta/2)$ corresponds to a non-truncated plane wave.

6.4 The Gouy Phase in Airy Beams

It is well-known that finite-energy 2D wave fields propagating in free space undergo an overall phase shift of $\pi/2$ rads (π rads for 3D waves) if they are compared with the transit of untruncated plane waves. For aberration-free focused waves, Gouy first realized that the phase is delayed within its focal region [271]. The origin of the Gouy phase (GP) shift is ascribed to the spatial confinement of the optical beam [272, 273], which leads to deviations in the wave front and, therefore, local alterations of the wavenumber in the near field [274, 275]. The interest in the analysis this effect persists nowadays because of its implication in many ultrafast phenomena that are dependent directly on the electric field rather than the pulse envelope such as electron emission from ionized atoms [276] and metal surfaces [277].

Recently Pang *et al.* studied the phase behavior of Airy beams (AiBs) [278]. Because of its curved trajectory [244, 279], they defined the GP of an AiB as the difference between its phase and that of a diverging cylindrical wave, the latter considered a suitable reference field. A physical interpretation of the GP can be given in terms of the local phase velocity and the Poynting vector streamlines of AiBs.

Let us evaluate the GP in AiBs. The GP $\varphi_G(\zeta)$ is commonly estimated as the cumulative phase difference between a given paraxial field and a plane wave also traveling in the $+z$ direction [274]. Considering a centrosymmetric distribution of

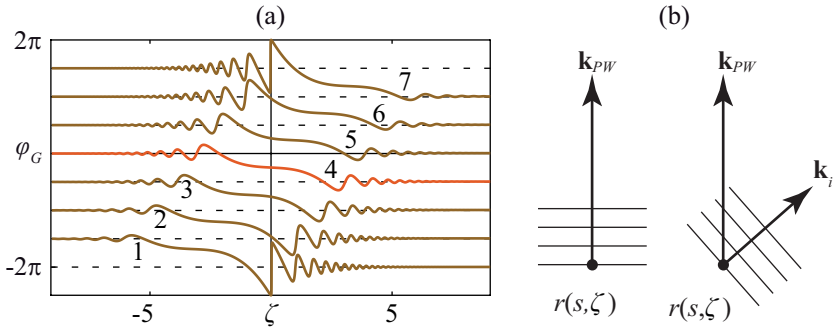


FIGURE 6.14: (a) GP for $k = \{0, \pm 0.41 \pm 1.00, \pm 1.52\}$. The curves are displaced by $\pi/2$ from one to another, with increasing k down upward. The numbers code agrees with that applied in Fig. 6.13. (b) Geometrical interpretation of the GP in terms of the local wave vector \mathbf{k}_{PW} of a plane wave and that \mathbf{k}_i of a paraxial beam.

u around $s = 0$, the dephase $\varphi_G(\zeta)$ may be derived analytically as the difference $\phi(\zeta) - \lim_{\zeta \rightarrow -\infty} \phi$ evaluated along the beam axis. Due to the particular acceleration of the AiB, however, one cannot encounter a beam axis in this case.

In a more general approach, the GP might account for dephasing between the wave field u given in (6.16) and a plane wave $u_{PW} = \exp(i\psi)$ with a given tilt $k \neq 0$. Following the discussion given above, the phase fronts of u and u_{PW} become parallel in the far field around the light ray (6.19). In order to obtain $\varphi_G(\zeta)$ for the normalized angle k we employ $\phi - ks + k^2\zeta/2$ instead of ϕ , which is now evaluated at points of the contour C . In Fig. 6.14(a) we plot $\varphi_G(\zeta)$ for different values of the zenith angle k . As expected, the value of the GP varies rapidly in the near field. Well beyond the near field, in the limit $\zeta \rightarrow +\infty$, the GP shift approaches $-\pi/2$.

Let us give a physical interpretation of our approach, which in principle may be applied to any finite-energy wave field that lacks a beam axis. For that purpose, it

is illustrative to rewrite the GP as the line integral

$$\varphi_G(\zeta) = \int_C \Delta \mathbf{k} \cdot d\mathbf{r}, \quad (6.21)$$

where $\Delta \mathbf{k} = \nabla \phi - \nabla \psi$ and C represents a contour of integration (6.19) with start point at $\zeta \rightarrow -\infty$. The form is exactly the same as that encountered when we calculate the work done by a resultant force $\Delta \mathbf{k}$ that varies along the path C . Here $\Delta \mathbf{k}$ is understood as the difference of the local wave vector $\mathbf{k}_i = k_0 \hat{z} + \nabla \phi$ of the AiB and that corresponding to the reference plane wave, $\mathbf{k}_{PW} = k_0 \hat{z} + \nabla \psi$. Note that \mathbf{k}_{PW} approaches $k_0 \hat{z} + (k/w_0) \hat{x}$ to order k , and that \mathbf{k}_{PW} is parallel to $d\mathbf{r}$ over the contour C . This is relevant since many physical processes, like the generation of curved plasma channels [280] and the optical manipulation of microparticles [281], depends openly on k_j , which is in direct proportion to the EM momentum and the time-averaged flux of energy [250].

Going from \mathbf{r} to $\mathbf{r} + d\mathbf{r}$ over C leads to a nonnegative contribution of the line integral (6.21) if (a) the wave vectors \mathbf{k}_{PW} and \mathbf{k}_i are nonparallel, and if (b) the wavenumber k_0 of the reference plane wave and that $k_j = |\mathbf{k}_i|$ of the field u are different. This is illustrated in Fig. 6.14(b). For a Gaussian beam $\varphi_G = -\pi/4 - \arctan(\zeta)/2$ at $k = 0$, where \mathbf{k}_i is parallel to \mathbf{k}_{PW} but $k_j < k_0$. In AiBs, however, both angular and modular detuning of \mathbf{k}_i are produced.

To examine the angular detuning, it is illustrative to represent \mathbf{k}_i graphically by means of the Poynting vector streamlines (PSLs). Commonly employed with vector fields, the PSLs are tangent to the vector \mathbf{k}_i and consequently they satisfy the differential equation $\mathbf{k}_i \times d\mathbf{r} = 0$, that is $dx/dz = (\mathbf{k}_i \cdot \hat{x})/(\mathbf{k}_i \cdot \hat{z})$. The PSLs indicate the direction of wave propagation since they are perpendicular to the phase fronts. Under the paraxial approximation the equation for the PSLs reduces to

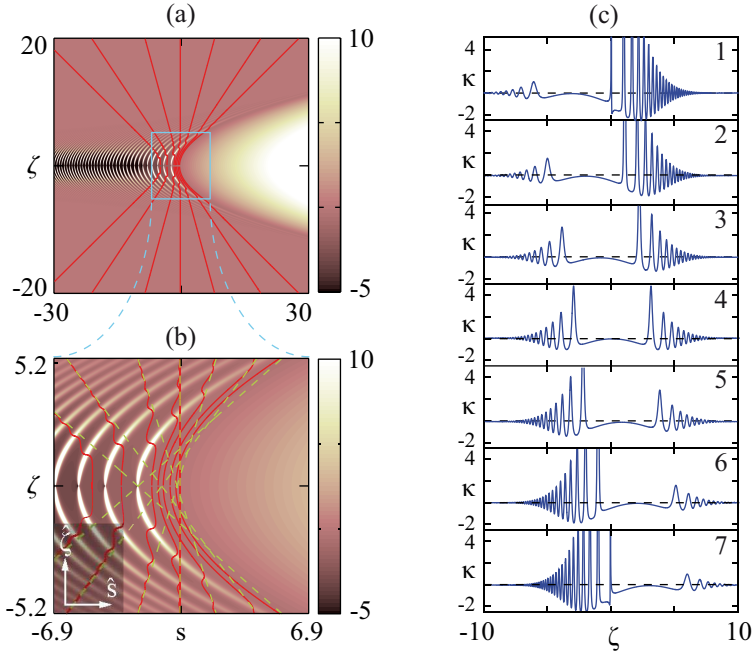


FIGURE 6.15: Spatial distribution of κ and several PSLs for the AiB of Fig. 6.13(c). Plots of κ over the numbered contours also representing asymptotes of the PSLs.

$ds/d\zeta = \partial_s \phi$ in normalized coordinates. For an AiB we finally have

$$\frac{ds}{d\zeta} = \frac{\zeta}{2} + \text{Im} \left[\frac{Ai'(s - \zeta^2/4 + ia\zeta)}{Ai(s - \zeta^2/4 + ia\zeta)} \right], \quad (6.22)$$

where $Ai'(\alpha) = \partial_\alpha Ai(\alpha)$. The exact solution $s = s_0 + \zeta^2/4$ is obtained for $a = 0$.

Some PSLs of our AiB are drawn in solid lines in Fig. 6.15(a) and Fig. 6.15(b). In contrast with the trajectories C of light rays (dashed lines), the PSLs hold $ds/d\zeta = 0$ at $\zeta = 0$. Therefore, PSLs approach a parabola $s = s_0 + s_0''\zeta^2/2$ in the neighborhood of the beam waist, where $s_0'' = as_0 - aAi'(s_0)^2/Ai(s_0)^2 + 1/2$. If $a \ll 1$ and $s_0 \geq 0$ then $s_0'' \approx 1/2$ featuring a regular parabolic trajectory. However

for sufficiently large values of $-s_0 \gg 1$ then $s_0'' < 0$ revealing a concavity inversion along the semi-axis. Moreover, in the far field $ds/d\zeta \rightarrow k$ leading to exact solutions in the form of Eq. (6.19) as $|\zeta| \rightarrow \infty$. These straight lines represent the asymptotes of the PSLs.

Finally we analyze the modular detuning of the local wavenumber with respect to k_0 . In fact, modular detuning of \mathbf{k}_i implies a local deviation of the phase velocity, v_p with respect to c [146]. Taking into account the paraxial regime, the local wavenumber is given by $k_j = k_0 + \kappa/z_R$, where

$$\kappa = \partial_\zeta \phi + (\partial_s \phi)^2/2. \quad (6.23)$$

Moreover we may obtain a simple expression for v_p by using $\Delta v/c \approx -\Delta k/k_0 = -\kappa/k_0 z_R$, where $\Delta v = v_p - c$ and $\Delta k = k_i - k_0$. In Fig. 6.15 we plot the parameter κ operating as a trend indicator of the spatial variation of the phase velocity of the AiB depicted in Fig. 6.15. In the far field κ vanishes leading to a wave field with wavenumber $k_i = k_0$ and phase velocity $v_p = c$.

However κ presents a more complex behavior in the near field. Out of the geometrical shadow, $\kappa < 0$ and it drops near the peaks of intensity. This effect is associated with superluminality, which is well known in Gaussian beams and other kind of focused beams [282, 283]. Over the caustic of the AiB, however, $\kappa \approx 0$ and it strictly vanishes if $a = 0$. On the contrary, κ grows sharply around the valleys of intensity, and for $a = 0$ it diverges due to the presence of phase singularities. We reported the results of this Section in Ref. [284].

Chapter 7

Conclusions

In this Thesis, the image formation with plasmonic nanostructures and NIMs is studied. First, we analyze the 3D diffraction pattern resulting when a NIM planar lens produces an image of a point source. This pattern is the 3D Fourier transform of a function that we called here the generalized ATF. The generalized ATF includes two different sheets: one, having a spherical shape, contains information of the far field, whereas the evanescent components of the wave are associated with the hyperboloidal sheet of the ATF. Particularly, subwavelength resolution is mostly determined by the modulation of the generalized ATF on the hyperboloidal sheet. In connection with this result, we have understood that increasing transverse resolution within the near-field regime may be produced at the cost of loss in depth discrimination.

The image formation with asymmetric NIM superlenses is also evaluated focusing on primary aberrations and backscattering effects. Both are unwanted effects derived from impedance mismatch at boundaries. We propose an antireflection

coating condition that minimizes backscattered light. To avoid primary spherical aberration, we show that the object plane will be placed at an appropriate distance from the front interface of the superlens. Nevertheless residual aberrations come out in the Gaussian conjugate plane, especially for slabs with a subwavelength width. Balancing residual aberrations may lead to achieve an impulse response of least spot size.

Considering again symmetric superlenses, it is well known that its resolution can be improved by exfoliating the NIM into layers. However, we show that the depth of field and the ability to observe images out of the geometrical image plane is reduced in exchange. A trade-off between the required resolution power and its limitations in the process of recording an image in volume should be considered during the design of a NIM multilayer.

The metal superlens is also revised in this Thesis. Surface plasmons can be excited on these superlenses providing access to an enormous phase space of refractive index and propagation constants that can be readily tuned through variation of material, dimension, or geometry. Specifically, we can tune a MD medium to match a permittivity close to zero. Regarding this subject, we highlight that uniaxial ENZ PLM have a plain dispersion curve that sustains high- k modes, i.e., works in the canalization regimen. The coupling of this structure with the evanescent modes of the source give rise to superlensing along the optical axis of the homogenized metamaterial that is clearly enhanced in the limit $\text{Re}(\epsilon_m) \rightarrow -\epsilon_d$. When $\epsilon_d \ll -\text{Re}(\epsilon_m)$, we have developed a simple curve-fitting method that helps to recover the high- k plasmonic modes that are lost in the standard EMA model.

We also present the generalized refraction law that describes double refraction of TM-polarized waves, conventional positive and negative, observed in the same

metamaterials. The modal coupling of plasmonic lattice resonances and nonlocality induced by partial screening across the nanolayer length are responsible for this effect. An analysis has been undertaken on the energy balance between this twin beams as a function of the PLM incidence angle.

Furthermore, a MD device capable to produce superresolving images out of the canalization regimen is demonstrated. A first MD superlattice with strong anisotropy converts evanescent fields into propagating Bloch modes. Beam spreading is compensated by means of negative refraction. For that purpose, a second MD superlattice with an isofrequency curve of opposite curvature collects the wide spectrum of Bloch waves and, subsequently, they are suitably focused just at the output plane of the superlensing device.

Major results presented in this Thesis are sustained in the PSF analysis. While this function is helpful in the image formation analysis, it is technically complicated to measure. We propose a version of the blind deconvolution algorithm including particular PLM thresholds that recovers the PSF throughout the experimental measures of the intensity at the superlens output interface. While standard blind deconvolution algorithm only recovers the PSF modulus, the version introduced in this Thesis is also able to recover the phase.

In addition to the canalization of evanescent waves in plasmonic-crystal superlenses enabling subwavelength-resolved images, we demonstrate the existence of auto-focused optical beams with subwavelength size propagating in more general photonic nanostructures. Specifically subwavelength BBs are analyzed in MD layered media and wire media. The origin of this interesting phenomenon lies in the phase-matched excitation of high-order SPPs in the superlattice. Dissipative effects in silver leads to a diffraction-free regime limited by its energy attenuation

length. Nevertheless, localization about the beam axis is maintained along a range which is higher than the energy attenuation length by more than one order of magnitude. The possibility to excite multiple BBs in these nanostructures opens the way for imaging formation with this kind of wave fields.

Finally, we consider a new family of non diffractive wave field, the Airy beam. In particular we have expressed the Gouy phase that can be measured on this sort of fields as a line integral. The equations describing the Poynting vector streamlines and the spatial variation of the phase velocity for these beams provide a general platform for exploring the flow of electromagnetic energy. This general analysis can be applied either to plasmon-assisted and free-space Airy beams.

7.1 Future lines

The results of this Thesis indicate the accessibility of tunable optical properties of nanomaterials. Combined with other existing photonic materials these structures facilitate the design of new materials classes with extraordinary applications. The following discussion highlights just a few potential avenues for future exploration including interaction between PLM and low dimensional systems, tunability with topological insulator and the design of resonant cavities which can operate in the canalization regime.

Quantum dots and nanowires are in state of art low dimensional systems enabling new optical and electronic capabilities. The possibilities of interaction between these elements and the superlenses studied in this Thesis may tailor electromagnetic properties. For instance, the use of metal in a PLM makes it lossy. Inserting quantum dots on it may provide some gain inside this structure [14, 17]. This

approach uses quantum degrees of freedom not to modify the effective properties, but to compensate the losses. Alternatively, doping a layered medium with quantum dots opens the way to tune the anisotropic effective permittivity tensor of this medium [285].

It is also interesting to consider the addition of alternative plasmonic materials as metallic alloys, metallic compounds, and graphene to superlenses. These materials are known to contain abundant free carriers. The oscillation of free electrons, when properly driven by electromagnetic waves, would excite SPPs in the vicinity of these surfaces same as in metals, resulting in extreme light confinement. It is likely that new PLM designs with improved properties can be done by tuning regular MD multilayers with these new materials.

Yet another possibility that we want to suggest comes by considering a multilayer in the periodicity direction as an open resonator, in which some modes exist [286]. Designing properly the band structure and bounding this piece of material with reflector will make it a resonant cavity.

Finally, a challenging task that remains unaccomplished is the image formation by means of AiBs. For that purpose, an array of subwavelength nondiffracting beams may be excited on a metallic surface. Each beam will act as a pixel in a 1D image. This idea can be extended to two-dimensional images by using BBs propagating in multilayered metamaterials or wire media.

Appendix A

Propagation Matrix Method

The relationship between the tangential components of the vectorial field, \mathbf{E} , in a layered medium is linear. In this Appendix we introduce the propagation matrix method: a useful tool to calculate the linear relations between the field amplitudes in a layered media.

Let us consider the multilayer structure from Fig. A.1, composed of two semi-infinite media sandwiching $J - 1$ media. For simplicity we assume that each

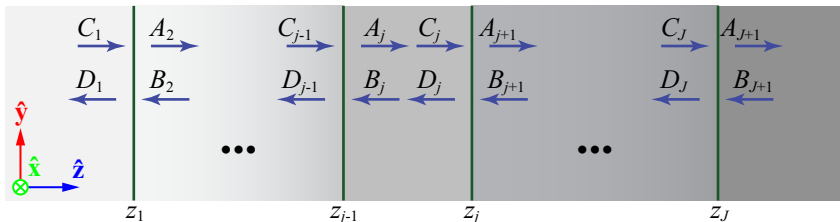


FIGURE A.1: Electric field amplitudes within an arbitrary multilayer. A_j and C_j (B_j and D_j) represents the right-going (left-going) waves. A_j and B_j are used for waves at the right-hand side of the interfaces, whereas C_j and D_j are used for waves at the left-hand side of the interface.

medium has a real permittivity, ϵ_j , and permeability, μ_j . We set a TE electric field in the direction of the unitary vector $\hat{\mathbf{x}}$. The field is a superposition of propagating and counterpropagating plane waves defined by the k_y components of the wave vector. Complex amplitude A_j and C_j goes for the right-going waves while the B_j and D_j describes the left-going waves. A_j and B_j implies waves at the right-hand side of an interface, whereas C_j and D_j implies waves at the left-hand side of an interface. Finally, the field amplitudes subscripts indicate the medium. The electric field at the j th layer ($z_{j-1} < z < z_j$) has a time-harmonic dependence $\exp(-i\omega t)$ and a spatial dependence

$$\begin{aligned} \mathbf{E}_j(y, z) &= \left[A_j e^{ik_{zj}(z-z_{j-1})} + B_j e^{-ik_{zj}(z-z_{j-1})} \right] e^{ik_y y} \hat{\mathbf{x}} = \\ &= \left[C_j e^{ik_{zj}(z-z_j)} + D_j e^{-ik_{zj}(z-z_j)} \right] e^{ik_y y} \hat{\mathbf{x}}, \end{aligned} \quad (\text{A.1})$$

where the z component of the wave vector satisfies $k_{zj}^2 = k_0^2 \epsilon_j \mu_j - k_y^2$.

By simple inspection of Eq. (A.1) we conclude that the constant amplitudes of the j th layer at z_{j-1} and z_j are related by

$$\begin{pmatrix} A_j \\ B_j \end{pmatrix} = \overset{\equiv}{P}_j \begin{pmatrix} C_j \\ D_j \end{pmatrix}, \quad (\text{A.2})$$

where we introduce the unimodular propagation matrix

$$\overset{\equiv}{P}_j = \begin{pmatrix} e^{ik_{zj}(z_{j-1}-z_j)} & 0 \\ 0 & e^{-ik_{zj}(z_{j-1}-z_j)} \end{pmatrix}. \quad (\text{A.3})$$

The magnetic field can be derived applying the Maxwell curl equation $\nabla \times \mathbf{E}_j = i\mu_j\mu_0\omega\mathbf{H}_j$ to Eq. (A.1) in each medium

$$\begin{aligned} \mathbf{H}_j(y, z) = & \frac{1}{\omega\mu_j\mu_0} [k_{zj} (C_j e^{ik_{zj}(z-z_j)} - D_j e^{-ik_{zj}(z-z_j)}) \hat{\mathbf{y}} + \\ & -k_y (C_j e^{ik_{zj}(z-z_j)} + D_j e^{-ik_{zj}(z-z_j)}) \hat{\mathbf{z}}] e^{iky}. \end{aligned} \quad (\text{A.4})$$

In absence of surface currents and charges, the boundary conditions at z_j are

$$\hat{\mathbf{x}} \cdot [\mathbf{E}_j(y, z_j) - \mathbf{E}_{j+1}(y, z_j)] = 0, \quad (\text{A.5a})$$

$$\hat{\mathbf{y}} \cdot [\mathbf{H}_j(y, z_j) - \mathbf{H}_{j+1}(y, z_j)] = 0. \quad (\text{A.5b})$$

If we substitute (A.1) and (A.4) in (A.5) then, the boundary conditions for the electric field amplitude are

$$C_j + D_j = A_{j+1} + B_{j+1}, \quad (\text{A.6a})$$

$$\frac{k_{zj}}{\mu_j} (C_j - D_j) = \frac{k_{zj+1}}{\mu_{j+1}} (A_{j+1} - B_{j+1}). \quad (\text{A.6b})$$

This linear system of equations can be rewritten as

$$\bar{\bar{D}}_{sj} \begin{pmatrix} C_j \\ D_j \end{pmatrix} = \bar{\bar{D}}_{sj+1} \begin{pmatrix} A_{j+1} \\ B_{j+1} \end{pmatrix}, \quad (\text{A.7})$$

being the unimodular dynamical matrix elements

$$\bar{\bar{D}}_{sj} = \begin{pmatrix} 1 & 1 \\ \frac{k_{zj}}{\mu_j} & -\frac{k_{zj}}{\mu_j} \end{pmatrix}. \quad (\text{A.8})$$

The product $\bar{\bar{D}}_{sj}^{-1} \bar{\bar{D}}_{sj+1}$ transforms the complex amplitudes at the exit of the j th

Dual quantities	
\mathbf{E}_j	\mathbf{H}_j
\mathbf{H}_j	$-\mathbf{E}_j$
ε_j	μ_j
μ_j	ε_j

TABLE A.1: Dual quantities for electric and magnetic current sources. Magnitudes in the left column have an analogous, or dual expression in the right column.

interface into the input amplitudes at the $(j + 1)$ th interface. The repeated application of the above transmission and propagation transformations for the $J - 1$ layers leads to:

$$\begin{pmatrix} C_1 \\ D_1 \end{pmatrix} = \bar{\bar{M}}_s \begin{pmatrix} A_{J+1} \\ B_{J+1} \end{pmatrix}, \quad (\text{A.9})$$

$\bar{\bar{M}}_s$ being a product of matrices 2×2 called the transfer matrix,

$$\bar{\bar{M}}_s = \begin{pmatrix} M_{11} & M_{12} \\ M_{21} & M_{22} \end{pmatrix} = \bar{\bar{D}}_{s1}^{-1} \left[\prod_{j=2}^J \bar{\bar{D}}_{sj} \bar{\bar{P}}_j \bar{\bar{D}}_{sj}^{-1} \right] \bar{\bar{D}}_{sJ+1}. \quad (\text{A.10})$$

If there is no source at the outside of a multilayer, then there are no left-going waves in the last media, $B_{J+1} = 0$. As a consequence, the matrix components M_{11} and M_{21} determine the multilayer transmission coefficient, $T = A_{J+1}/C_1$, and reflection coefficient, $R = D_1/C_1$,

$$T = \frac{1}{M_{11}}, \quad (\text{A.11a})$$

$$R = \frac{M_{21}}{M_{11}}. \quad (\text{A.11b})$$

The TE-modes amplitudes along parallel surfaces have been connected by the transfer matrix formulation. It is possible to repeat this process for TM-modes

by following an analogous procedure. Alternatively, expressions for TM-modes can be inferred by applying the duality theorem [287] on the earlier deduced TE-modes expressions. Theorem applies to a set of equations with null electric current density, $|\mathbf{J}| = 0$, or magnetic current density, $|\mathbf{M}| = 0$. A new set of equations for TM modes can be produced by substituting the EM parameters and fields for its dual quantities following the correspondences shown on Table A.1. Thus, the dynamic matrix for TM-modes

$$\bar{D}_{pj} = \begin{pmatrix} 1 & 1 \\ \frac{k_{zj}}{\epsilon_j} & -\frac{k_{zj}}{\epsilon_j} \end{pmatrix}, \quad (\text{A.12})$$

could be inferred from Eq. (A.7).

In this Appendix we have considered that the electric field, \mathbf{E} , is linearly polarized along the x axis. However, provided a s -polarization, this field can be oriented in other direction within the plane xy . In such a case it may also be used a new Cartesian coordinate system, (x', y', z) , where the electric field points along the x' axis. In particular, the transverse wave vector $k_{\perp} = \sqrt{k_x^2 + k_y^2}$ might be referred as $k_{y'}$ in this new coordinate system. After this transformation we may follow the transfer matrix formulation given above.

Bibliography

- [1] E. Abbe. Beiträge zur theorie des mikroskops und der mikroskopischen wahrnehmung. *Archiv für mikroskopische Anatomie*, 9(1):413, 1873.
- [2] V.G. Veselago. The electrodynamics of substances with simultaneously negative values of ϵ and μ . *Physics-Uspekhi*, 10(4):509, 1968.
- [3] J.B. Pendry. Negative refraction makes a perfect lens. *Phys. Rev. Lett.*, 85: 3966, 2000.
- [4] S.A. Ramakrishna, J.B. Pendry, M.C.K. Wiltshire, and W.J. Stewart. Imaging the near field. *J. Mod. Opt.*, 50(9):1419, 2003.
- [5] N. Garcia and M. Nieto-Vesperinas. Left-handed materials do not make a perfect lens. *Phys. Rev. Lett.*, 88(20):207403, 2002.
- [6] P.F. Loschialpo, D.L. Smith, D.W. Forester, F.J. Rachford, and J. Schelleng. Electromagnetic waves focused by a negative-index planar lens. *Phys. Rev. E*, 67:025602, 2003.
- [7] D.R. Smith, D. Schurig, M. Rosenbluth, S. Schultz, S.A. Ramakrishna, and J.B. Pendry. Limitations on subdiffraction imaging with a negative refractive index slab. *Appl. Phys. Lett.*, 82(10):1506, 2003.

- [8] S.A. Ramakrishna, J.B. Pendry, D. Schurig, D.R. Smith, and S. Schultz. The asymmetric lossy near-perfect lens. *J. Mod. Opt.*, 49(10):1747, 2002.
- [9] D. Güney, T. Koschny, and C.M. Soukoulis. Reducing ohmic losses in metamaterials by geometric tailoring. *Phys. Rev. B*, 80(12):125129, 2009.
- [10] S.A. Tretyakov. Meta-materials with wideband negative permittivity and permeability. *Microw. Opt. Techn. Lett.*, 31(3):163, 2001.
- [11] S.A. Ramakrishna and J.B. Pendry. Removal of absorption and increase in resolution in a near-field lens via optical gain. *Phys. Rev. B*, 67:201101, 2003.
- [12] J.B. Pendry and D.R. Smith. Reversing light with negative refraction. *Phys. Today*, 57:37, 2004.
- [13] T.A. Klar, A.V. Kildishev, V.P. Drachev, and V.M. Shalaev. Negative-index metamaterials: going optical. *J. Sel. Top. Quantum Electron.*, 12(6):1106, 2006.
- [14] A.K. Sarychev and G. Tartakovskiy. Magnetic plasmonic metamaterials in actively pumped host medium and plasmonic nanolaser. *Phys. Rev. B*, 75(8):085436, 2007.
- [15] S. Xiao, V.P. Drachev, A.V. Kildishev, X. Ni, U.K. Chettiar, H.-K. Yuan, and V.M. Shalaev. Loss-free and active optical negative-index metamaterials. *Nature*, 466(7307):735, 2010.
- [16] C.M. Soukoulis and M. Wegener. Optical metamaterials - more bulky and less lossy. *Science*, 330(6011):1633, 2010.

-
- [17] S. Wuestner, A. Pusch, K.L. Tsakmakidis, J.M. Hamm, and O. Hess. Overcoming losses with gain in a negative refractive index metamaterial. *Phys. Rev. Lett.*, 105(12):127401, 2010.
- [18] A.D. Boardman, V.V. Grimalsky, Y.S. Kivshar, S.V. Koshevaya, M. Lapine, N.M. Litchinitser, V.N. Malnev, M. Noginov, Y.G. Rapoport, and V.M. Shalaev. Active and tunable metamaterials. *Laser Photon. Rev.*, 5(2):287, 2011.
- [19] J.R. Minkel. Left-handed materials debate heats up. *Phys. Rev. Focus*, 9:23, 2002.
- [20] J. Valentine, S. Zhang, T. Zentgraf, E. Ulin-Avila, D.A. Genov, G. Bartal, and X. Zhang. Three-dimensional optical metamaterial with a negative refractive index. *Nature*, 455(7211):376, 2008.
- [21] N. Fang, H. Lee, C. Sun, and X. Zhang. Sub-diffraction-limited optical imaging with a silver superlens. *Science*, 308(5721):534, 2005.
- [22] Z. Liu, H. Lee, Y. Xiong, C. Sun, and X. Zhang. Far-field optical hyperlens magnifying sub-diffraction-limited objects. *Science*, 315(5819):1686, 2007.
- [23] D.R. Smith, W.J. Padilla, D.C. Vier, S.C. Nemat-Nasser, and S. Schultz. Composite medium with simultaneously negative permeability and permittivity. *Phys. Rev. Lett.*, 84(18):4184, 2000.
- [24] R.A. Shelby, D.R. Smith, and S. Schultz. Experimental verification of a negative index of refraction. *Science*, 292(5514):77, 2001.

- [25] C.G. Parazzoli, R.B. Gregor, K. Li, B.E.C. Koltenbah, and M. Tanielian. Experimental verification and simulation of negative index of refraction using Snell's law. *Phys. Rev. Lett.*, 90(10):107401, 2003.
- [26] K. Aydin, I. Bulu, and E. Ozbay. Focusing of electromagnetic waves by a left-handed metamaterial flat lens. *Opt. Express*, 13(22):8753, 2005.
- [27] J. Zhou, Th. Koschny, M. Kafesaki, E.N. Economou, J.B. Pendry, and C.M. Soukoulis. Saturation of the magnetic response of split-ring resonators at optical frequencies. *Phys. Rev. Lett.*, 95(22):223902, 2005.
- [28] C. García-Meca, J. Hurtado, J. Martí, A. Martínez, W. Dickson, and A.V. Zayats. Low-loss multilayered metamaterial exhibiting a negative index of refraction at visible wavelengths. *Phys. Rev. Lett.*, 106(6):067402, 2011.
- [29] D. Chanda, K. Shigeta, S. Gupta, T. Cain, A. Carlson, A. Mihi, A.J. Baca, G.R. Bogart, P. Braun, and J.A. Rogers. Large-area flexible 3D optical negative index metamaterial formed by nanotransfer printing. *Nat. Nanotechnol.*, 6(7):402, 2011.
- [30] C. Sabah. Novel, dual band, single and double negative metamaterials: nonconcentric delta loop resonators. *Prog. Electromagn. Res. B*, 25:225, 2010.
- [31] C. Sabah. Composition of non-concentric triangular split ring resonators and wire strip for dual-band negative index metamaterials. In *Proc. MMS*, page 303, 2010.
- [32] C. Sabah. Multiband planar metamaterials. *Microwave Opt. Tech. Lett.*, 53(10):2255, 2011.

-
- [33] C. Sabah. Tunable metamaterial design composed of triangular split ring resonator and wire strip for S-and C-microwave bands. *Prog. Electromagn. Res. B*, 22:341, 2010.
- [34] R.A. Shelby, D.R. Smith, and S. Schultz. Experimental verification of a negative index of refraction. *Science*, 292(5514):77, 2001.
- [35] A.A. Houck, J.B. Brock, and I.L. Chuang. Experimental observations of a left-handed material that obeys Snell's law. *Phys. Rev. Lett.*, 90(13):137401, 2003.
- [36] Z. Liu, N. Fang, T.-J. Yen, and X. Zhang. Rapid growth of evanescent wave by a silver superlens. *Appl. Phys. Lett.*, 83(25):5184, 2003.
- [37] N. Fang, Z. Liu, T.-J. Yen, and X. Zhang. Regenerating evanescent waves from a silver superlens. *Opt. Express*, 11(7):682, 2003.
- [38] S. Feng, J. Elson, and P. Overfelt. Optical properties of multilayer metal-dielectric nanofilms with all-evanescent modes. *Opt. Express*, 13(11):4113, 2005.
- [39] D. De Ceglia, M.A. Vincenti, M.G. Cappeddu, M. Centini, N. Akozbek, A. D'Orazio, J.W. Haus, M.J. Bloemer, and M. Scalora. Tailoring metal-lodielectric structures for superresolution and superguiding applications in the visible and near-IR ranges. *Phys. Rev. A*, 77(3):033848, 2008.
- [40] T.W. Allen and R.G. DeCorby. Assessing the maximum transmittance of periodic metal-dielectric multilayers. *J. Opt. Soc. Am. B*, 28(10):2529, 2011.

- [41] T.W. Allen and R.G. DeCorby. Conditions for admittance-matched tunneling through symmetric metal-dielectric stacks. *Opt. Express*, 20(105):A578, 2012.
- [42] S. Tomita, T. Yokoyama, H. Yanagi, B. Wood, J.B. Pendry, M. Fujii, and S. Hayashi. Resonant photon tunneling via surface plasmon polaritons through one-dimensional metal-dielectric metamaterials. *Opt. Express*, 16(13):9942, 2008.
- [43] E. Shamonina, V.A. Kalinin, K.H. Ringhofer, and L. Solymar. Imaging, compression and Poynting vector streamlines for negative permittivity materials. *Elect. Lett.*, 37(20):1243, 2001.
- [44] H. Cory and A. Barger. Surface-wave propagation along a metamaterial slab. *Opt. Tech. Lett.*, 38(5):392, 2003.
- [45] E. Verhagen, R. de Waele, L. Kuipers, and A. Polman. Three-dimensional negative index of refraction at optical frequencies by coupling plasmonic waveguides. *Phys. Rev. Lett.*, 105(22):223901, 2010.
- [46] L. Verslegers, P. Catrysse, Z. Yu, and S. Fan. Deep-subwavelength focusing and steering of light in an aperiodic metallic waveguide array. *Phys. Rev. Lett.*, 103:033902, 2009.
- [47] H. Wang, X. Wang, Y. Li, J. Chen, C. Guo, and J. Ding. A new type of vector fields with hybrid states of polarization. *Opt. Express*, 18(10):10786, 2010.
- [48] Y. Xiong, Z. Liu, C. Sun, and X. Zhang. Two-dimensional imaging by far-field superlens at visible wavelengths. *Nano Lett.*, 7(11):3360–5, 2007.

-
- [49] H.-T. Chien, H.-T. Tang, C.-H. Kuo, C.-C. Chen, and Z. Ye. Directed diffraction without negative refraction. *Phys. Rev. B*, 70(11):113101, 2004.
- [50] Z.-Y. Li and L.-L. Lin. Evaluation of lensing in photonic crystal slabs exhibiting negative refraction. *Phys. Rev. B*, 68(24):245110, 2003.
- [51] C.-H. Kuo and Z. Ye. Optical transmission of photonic crystal structures formed by dielectric cylinders: Evidence for non-negative refraction. *Phys. Rev. E*, 70:056608, 2004.
- [52] P.A. Belov, C.R. Simovski, and P. Ikonen. Canalization of subwavelength images by electromagnetic crystals. *Phys. Rev. B*, 71(19):193105, 2005.
- [53] Z. Jakšić and M. Maksimović. Ordered artificial nanocomposites for imaging beyond diffraction limit. In *Proc. 1st International Workshop on Nanoscience & Nanotechnology*, page 147, 2005.
- [54] K.J. Webb and M. Yang. Subwavelength imaging with a multilayer silver film structure. *Opt. Lett.*, 31(14):2130, 2006.
- [55] B. Wood, J.B. Pendry, and D.P. Tsai. Directed subwavelength imaging using a layered metal-dielectric system. *Phys. Rev. B*, 74:115116, 2006.
- [56] P.A. Belov and Y. Hao. Subwavelength imaging at optical frequencies using a transmission device formed by a periodic layered metal-dielectric structure operating in the canalization regime. *Phys. Rev. B*, 73(11):113110, 2006.
- [57] M. Scalora, G. D'Aguanno, N. Mattiucci, M.J. Bloemer, D. de Ceglia, M. Centini, A. Mandatori, C. Sibilìa, N. Akozbek, and M.G. Cappeddu. Negative refraction and sub-wavelength focusing in the visible range using transparent metallo-dielectric stacks. *Opt. Express*, 15(2):508, 2007.

174 Bibliography

- [58] A.J. Hoffman, L. Alekseyev, S.S. Howard, K.J. Franz, D. Wasserman, V.A. Podolskiy, E.E. Narimanov, D.L. Sivco, and C. Gmachl. Negative refraction in semiconductor metamaterials. *Nat. Mater.*, 6(12):946, 2007.
- [59] C.M. Soukoulis and M. Wegener. Past achievements and future challenges in the development of three-dimensional photonic metamaterials. *Nat. Photon.*, 5(9):523, 2011.
- [60] X. Ni, S. Ishii, M.D. Thoreson, V.M. Shalaev, S. Han, S. Lee, and A.V. Kildishev. Loss-compensated and active hyperbolic metamaterials. *Opt. Express*, 19(25):25242, 2011.
- [61] R. Wangberg, J. Elser, E.E. Narimanov, and V.A. Podolskiy. Nonmagnetic nanocomposites for optical and infrared negative-refractive-index media. *J. Opt. Soc. Am. B*, 23(3):498, 2006.
- [62] J. Yang, X. Hu, X. Li, Z. Liu, X. Jiang, and J. Zi. Cancellation of reflection and transmission at metamaterial surfaces. *Opt. Lett.*, 35(1):16, 2010.
- [63] R. Warmbier, G.S. Manyali, and A. Quandt. Surface plasmon polaritons in lossy uniaxial anisotropic materials. *Phys. Rev. B*, 85(8):085442, 2012.
- [64] Z. Liu, S. Durant, H. Lee, Y. Pikus, Y. Xiong, C. Sun, and X. Zhang. Experimental studies of far-field superlens for sub-diffractive optical imaging. *Opt. express*, 15(11):6947, 2007.
- [65] S. Durant, Z. Liu, J.M. Steele, and X. Zhang. Theory of the transmission properties of an optical far-field superlens for imaging beyond the diffraction limit. *J. Opt. Soc. Am. B*, 23(11):2383, 2006.
- [66] Z. Liu, S. Durant, H. Lee, Y. Pikus, N. Fang, Y. Xiong, C. Sun, and X. Zhang. Far-field optical superlens. *Nano Lett.*, 7(2):403, 2007.

-
- [67] Z. Jacob, L.V. Alekseyev, and E. Narimanov. Optical hyperlens: far-field imaging beyond the diffraction limit. *Opt. Express*, 14(18):8247, 2006.
- [68] A. Salandrino and N. Engheta. Far-field subdiffraction optical microscopy using metamaterial crystals: theory and simulations. *Phys. Rev. B*, 74(7):075103, 2006.
- [69] Y. Ben-Aryeh. Transmission enhancement by conversion of evanescent waves into propagating waves. *Appl. Phys. B*, 91(1):157, 2008.
- [70] C. Ma, R. Aguinaldo, and Z. Liu. Advances in the hyperlens. *Chin. Sci. Bull.*, 55(24):2618, 2010.
- [71] I.I. Smolyaninov, Y.-J. Hung, and C.C. Davis. Magnifying superlens in the visible frequency range. *Science*, 315(5819):1699, 2007.
- [72] J. Rho, Z. Ye, Y. Xiong, X. Yin, Z. Liu, H. Choi, G. Bartal, and X. Zhang. Spherical hyperlens for two-dimensional sub-diffractive imaging at visible frequencies. *Nat. Commun.*, 1:143, 2010.
- [73] G. Shvets, S. Trendafilov, J.B. Pendry, and A. Sarychev. Guiding, focusing, and sensing on the subwavelength scale using metallic wire arrays. *Phys. Rev. Lett.*, 99(5):053903, 2007.
- [74] A. Ono, J.-I. Kato, and S. Kawata. Subwavelength optical imaging through a metallic nanorod array. *Phys. Rev. Lett.*, 95(26):267407, 2005.
- [75] P. Ikonen, C. Simovski, S. Tretyakov, P. Belov, and Y. Hao. Magnification of subwavelength field distributions at microwave frequencies using a wire medium slab operating in the canalization regime. *Appl. Phys. Lett.*, 91(10):104102, 2007.

- [76] Y. Zhao, G. Palikaras, P.A. Belov, R.F. Dubrovka, C.R. Simovski, Y. Hao, and C.G. Parini. Magnification of subwavelength field distributions using a tapered array of metallic wires with planar interfaces and an embedded dielectric phase compensator. *New J. Phys.*, 12(10):103045, 2010.
- [77] S. Han, Y. Xiong, D. Genov, Z. Liu, G. Bartal, and X. Zhang. Ray optics at a deep-subwavelength scale: a transformation optics approach. *Nano Lett.*, 8(12):4243, 2008.
- [78] A.V. Kildishev and V.M. Shalaev. Engineering space for light via transformation optics. *Opt. Lett.*, 33(1):43, 2008.
- [79] M. Tsang and D. Psaltis. Magnifying perfect lens and superlens design by coordinate transformation. *Phys. Rev. B*, 77(3):035122, 2008.
- [80] J. Li, S. Han, S. Zhang, G. Bartal, and X. Zhang. Designing the Fourier space with transformation optics. *Opt. Lett.*, 34(20):3128, 2009.
- [81] C. Ma and Z. Liu. A super resolution metalens with phase compensation mechanism. *Appl. Phys. Lett.*, 96(18):183103, 2010.
- [82] C. Ma and Z. Liu. Focusing light into deep subwavelength using metamaterial immersion lenses. *Opt. Express*, 18(5):4838, 2010.
- [83] C. Ma, M.A. Escobar, and Z. Liu. Extraordinary light focusing and Fourier transform properties of gradient-index metalenses. *Phys. Rev. B*, 84(19):195142, 2011.
- [84] C. Ma and Z. Liu. Breaking the imaging symmetry in negative refraction lenses. *Opt. Express*, 20(3):2581, 2012.

-
- [85] A. Boltasseva and H.A. Atwater. Low-loss plasmonic metamaterials. *Science*, 331(290), 2011.
- [86] G.V. Naik, J. Liu, A.V. Kildishev, V.M. Shalaev, and A. Boltasseva. Demonstration of Al:ZnO as a plasmonic component for near-infrared metamaterials. *Proc. Nat. Acad. Sci. U.S.A.*, 109(23):8834, 2012.
- [87] J.N. Anker, W.P. Hall, O. Lyandres, N.C. Shah, J. Zhao, and R.P. Van Duyne. Biosensing with plasmonic nanosensors. *Nat. Mater.*, 7(6):442, 2008.
- [88] J. Yao, Z. Liu, Y. Liu, Y. Wang, C. Sun, G. Bartal, A.M. Stacy, and X. Zhang. Optical negative refraction in bulk metamaterials of nanowires. *Science*, 321(5891):930, 2008.
- [89] V.M. Shalaev, W. Cai, U.K. Chettiar, H. Yuan, A.K. Sarychev, V.P. Drachev, and A.V. Kildishev. Negative index of refraction in optical metamaterials. *Opt. Lett.*, 30(24):3356, 2005.
- [90] S. Zhang, W. Fan, N.C. Panoiu, K.J. Malloy, R.M. Osgood, and S.R.J. Brueck. Experimental demonstration of near-infrared negative-index metamaterials. *Phys. Rev. Lett.*, 95:137404, 2005.
- [91] J.B. Pendry, D. Schurig, and D.R. Smith. Controlling electromagnetic fields. *Science*, 312(5781):1780, 2006.
- [92] C.M. Soukoulis, S. Linden, and M. Wegener. Negative refractive index at optical wavelengths. *Science*, 315(5808):47, 2007.
- [93] V.M. Shalaev. Optical negative-index metamaterials. *Nat. Phot.*, 1(1):41, 2007.

- [94] T.J. Yen, W.J. Padilla, N. Fang, D.C. Vier, D.R. Smith, J.B. Pendry, D.N. Basov, and X. Zhang. Terahertz magnetic response from artificial materials. *Science*, 303(5663):1494, 2004.
- [95] S. Linden, C. Enkrich, M. Wegener, J. Zhou, T. Koschny, and C.M. Soukoulis. Magnetic response of metamaterials at 100 terahertz. *Science*, 306(5700):1351, 2004.
- [96] C. Enkrich, M. Wegener, S. Linden, S. Burger, L. Zschiedrich, F. Schmidt, J.F. Zhou, Th. Koschny, and C.M. Soukoulis. Magnetic metamaterials at telecommunication and visible frequencies. *Phys. Rev. Lett.*, 95:203901, 2005.
- [97] C. Enkrich, F. Pérez-Willard, D. Gerthsen, J.F. Zhou, T. Koschny, C.M. Soukoulis, M. Wegener, and S. Linden. Focused-ion-beam nanofabrication of near-infrared magnetic metamaterials. *Adv. Mater.*, 17(21):2547, 2005.
- [98] M.W. Klein, C. Enkrich, M. Wegener, C.M. Soukoulis, and S. Linden. Single-slit split-ring resonators at optical frequencies: limits of size scaling. *Opt. Lett.*, 31(9):1259, 2006.
- [99] G. Dolling, C. Enkrich, M. Wegener, C.M. Soukoulis, and S. Linden. Simultaneous negative phase and group velocity of light in a metamaterial. *Science*, 312(5775):892, 2006.
- [100] S. Xiao, U.K. Chettiar, A.V. Kildishev, V.P. Drachev, and V.M. Shalaev. Yellow-light negative-index metamaterials. *Opt. Lett.*, 34(22):3478, 2009.
- [101] J.D. Jackson. *Classical electrodynamics*. Wiley, 1998.
- [102] D.J. Griffiths. *Introduction to electrodynamics*. Pearson, 1999.

-
- [103] P.B. Johnson and R.W. Christy. Optical constants of the noble metals. *Phys. Rev. B*, 6:4370, 1972.
- [104] E.D. Palik. *Handbook of optical constants of solids*, volume 3. Elsevier Science, 1998.
- [105] M.A. Ordal, R.J. Bell, R.W. Alexander, L.L. Long, and M.R. Query. Optical properties of fourteen metals in the infrared and far infrared: Al, Co, Cu, Au, Fe, Pb, Mo, Ni, Pd, Pt, Ag, Ti, V, and W. *Appl. Opt.*, 24(24):4493, 1985.
- [106] A. Sommerfeld. Über die ausbreitung der wellen in der drahtlosen telegraphie [Tr. Propagation of electro-dynamic waves along a cylindrical conductor]. *Annalen der Physik*, 333(4):665, 1909.
- [107] K.A. Norton. The propagation of radio waves over the surface of the earth and in the upper atmosphere. *Proc. IRE*, 24(10):1367, 1936.
- [108] A. Otto. Experimental investigation of surface polaritons on plane interfaces. In *Festkörperprobleme 14*, page 1. Springer Berlin Heidelberg, 1974.
- [109] G. Boisdé and A. Harmer. *Chemical and biochemical sensing with optical fibers and waveguides*, volume 5. Artech House Norwood, 1996.
- [110] V.M. Agranovich and D.L. Mills. *Surface polaritons: electromagnetic waves at surfaces and interfaces*. North-Holland Pub. Co., 1982.
- [111] H. Raether. *Surface plasmons on smooth and rough surfaces and on gratings*, volume 111. Springer Berlin Heidelberg, 1988.
- [112] H.E. Ponath and G.I. Stegeman. *Nonlinear surface electromagnetic phenomena*. North-Holland Publ., 1991.

180 Bibliography

- [113] A.D. Boardman. *Electromagnetic surface modes*. John Wiley & Sons Australia, Limited, 1982.
- [114] R. Marqués, F. Martín, and M. Sorolla. *Metamaterials with negative parameter: theory, design, and microwave applications*. Wiley-Interscience, 2008.
- [115] R. Ruppin. Surface polaritons of a left-handed medium. *Phys. Lett. A*, 277(1):61, 2000.
- [116] S.A. Maier. *Plasmonics: fundamentals and applications*. Springer, 2010.
- [117] L. Novotny and B. Hecht. *Principles of nano-optics*. Cambridge University Press, 2006.
- [118] J.E. Sipe. New Green-function formalism for surface optics. *J. Opt. Soc. Am. B*, 4(4):481, 1987.
- [119] G.S. Agarwal. Quantum electrodynamics in the presence of dielectrics and conductors. I. Electromagnetic-field response functions and black-body fluctuations in finite geometries. *Phys. Rev. A*, 11:230, 1975.
- [120] T. Hakkarainen, T. Setälä, and A.T. Friberg. Subwavelength electromagnetic near-field imaging of point dipole with metamaterial nanoslab. *J. Opt. Soc. Am. A*, 26(10):2226, 2009.
- [121] P. Yeh. *Optical waves in layered media*, volume 95. Wiley New York, 1988.
- [122] C.J. Zapata-Rodríguez, D. Pastor, J.J. Miret, and S. Vuković. Uniaxial epsilon-near-zero metamaterials: from superlensing to double refraction. *J. Nanophoton.*, 8(1):083895, 2014.

-
- [123] V.A. Podolskiy and E.E. Narimanov. Near-sighted superlens. *Opt. Lett.*, 30(1):75, 2005.
- [124] E. Plum, V.A. Fedotov, P. Kuo, D.P. Tsai, and N.I. Zheludev. Towards the lasing spaser: controlling metamaterial optical response with semiconductor quantum dots. *Opt. Express*, 17(10):8548, 2009.
- [125] M.A. Noginov, G. Zhu, M. Mayy, B.A. Ritzo, N. Noginova, and V.A. Podolskiy. Stimulated emission of surface plasmon polaritons. *Phys. Rev. Lett.*, 101(22):226806, 2008.
- [126] S.M. Rytov. Electromagnetic properties of layered media. *Sov. Phys.*, 2:466, 1956.
- [127] C.J. Zapata-Rodríguez, J.J. Miret, S. Vuković, and M.R. Belić. Engineered surface waves in hyperbolic metamaterials. *Opt. Express*, 21(16):19113, 2013.
- [128] S.M. Vuković, I.V. Shadrivov, and Y.S. Kivshar. Surface Bloch waves in metamaterial and metal-dielectric superlattices. *Appl. Phys. Lett.*, 95(4):041902, 2009.
- [129] C.J. Zapata-Rodríguez, D. Pastor, P. Cencillo, M. Avellaneda, S. Vuković, and J.J. Miret. Dual hyperbolic-elliptic media. In *Proc. SPIE*, volume 8423, page 84231Z, 2012.
- [130] A.A. Orlov, P.M. Voroshilov, P.A. Belov, and Y.S. Kivshar. Engineered optical nonlocality in nanostructured metamaterials. *Phys. Rev. B*, 84(4):045424, 2011.
- [131] R.-L. Chern, D. Han, Z.Q. Zhang, and C.T. Chan. Additional waves in the graphene layered medium. *Opt. Express*, 22(26):31677, 2014.

182 Bibliography

- [132] C.J. Zapata-Rodríguez, D. Pastor, L.E. Martínez, M.T. Caballero, and J.J. Miret. Single-Polarization Double Refraction in Plasmonic Crystals: Considerations on Energy Flow. *Appl. Mech. Mater.*, 472:729, 2014.
- [133] S.A. Cummer. Simulated causal subwavelength focusing by a negative refractive index slab. *Appl. Phys. Lett.*, 82(10):1503, 2003.
- [134] G. Dolling, M. Wegener, C.M. Soukoulis, and S. Linden. Negative-index metamaterial at 780 nm wavelength. *Opt. Lett.*, 32(1):53, 2007.
- [135] U.K. Chettiar, A.V. Kildishev, H. Yuan, W. Cai, S. Xiao, V.P. Drachev, and V.M. Shalaev. Dual-band negative index metamaterial: double negative at 813 nm and single negative at 772 nm. *Opt. Lett.*, 32(12):1671, 2007.
- [136] P.A. Belov, Y. Zhao, S. Tse, P. Ikonen, M.G. Silveirinha, C.R. Simovski, S. Tretyakov, Y. Hao, and C. Parini. Transmission of images with sub-wavelength resolution to distances of several wavelengths in the microwave range. *Phys. Rev. B*, 77(19):193108, 2008.
- [137] B.D.F. Casse, W.T. Lu, Y.J. Huang, E. Gultepe, L. Menon, and S. Sridhar. Super-resolution imaging using a three-dimensional metamaterials nanolens. *Appl. Phys. Lett.*, 96(2):023114, 2010.
- [138] G. Gomez-Santos. Universal features of the time evolution of evanescent modes in a left-handed perfect lens. *Phys. Rev. Lett.*, 90(7):077401, 2003.
- [139] C.J. Zapata-Rodríguez, D. Pastor, and J.J. Miret. Three-dimensional point spread function and generalized amplitude transfer function of near-field flat lenses. *Appl. Opt.*, 49(30):5870, 2010.
- [140] C.J. Zapata-Rodríguez, D. Pastor, V. Camps, M.T. Caballero, and J.J. Miret. Three-dimensional point spread function of multilayered flat lenses and its

-
- application to extreme subwavelength resolution. *J. Nanophoton.*, 5(1):051807, 2011.
- [141] M. Nieto-Vesperinas. Problem of image superresolution with a negative-refractive-index slab. *J. Opt. Soc. Am. A*, 21(4):491, 2004.
- [142] K. Miyamoto and E. Wolf. Generalization of the Maggi-Rubinowicz theory of the boundary diffraction wave—Part I. *J. Opt. Soc. Am.*, 52(6):615, 1962.
- [143] E. Collett and E. Wolf. Symmetry properties of focused fields. *Opt. Lett.*, 5(6):264, 1980.
- [144] C.W. McCutchen. Generalized aperture and the three-dimensional diffraction image. *J. Opt. Soc. Am.*, 54(2):240, 1964.
- [145] R. Marques, M.J. Freire, and J.D. Baena. Theory of three-dimensional subdiffraction imaging. *App. Phys. Lett.*, 89(21):211113, 2006.
- [146] M. Born, E. Wolf, and A.B. Bhatia. *Principles of optics: electromagnetic theory of propagation, interference and diffraction of light*, chapter Optics of crystals. Cambridge University Press, 1999.
- [147] C. Girard and A. Dereux. Near-field optics theories. *Rep. Prog. Phys.*, 59(5):657, 1996.
- [148] P.F. Loschialpo, D.W. Forester, D.L. Smith, F.J. Rachford, and C. Monzon. Optical properties of an ideal homogeneous causal left-handed material slab. *Phys. Rev. E*, 70:036605, 2004.
- [149] Z. Lin and Y. Zou. Low-order aberration corrections of multilayer flat lenses using negative-index materials. *Appl. Opt.*, 45(27):6925, 2006.

184 Bibliography

- [150] P.M. Valanju, R.M. Walser, and A.P. Valanju. Wave refraction in negative-index media: always positive and very inhomogeneous. *Phys. Rev. Lett.*, 88:187401, 2002.
- [151] T. Matsumoto, S. Fujita, and T. Baba. Wavelength demultiplexer consisting of photonic crystal superprism and superlens. *Opt. Express*, 13(26):10768, 2005.
- [152] T. Matsumoto, K. Eom, and T. Baba. Focusing of light by negative refraction in a photonic crystal slab superlens on silicon-on-insulator substrate. *Opt. Lett.*, 31(18):2786, 2006.
- [153] T. Dumelow, J.A.P. da Costa, and V.N. Freire. Slab lenses from simple anisotropic media. *Phys. Rev. B*, 72:235115, 2005.
- [154] H. Luo, Z. Ren, W. Shu, and F. Li. Construction of a polarization insensitive lens from a quasi-isotropic metamaterial slab. *Phys. Rev. E*, 75:026601, 2007.
- [155] I. Bulu, H. Caglayan, and E. Ozbay. Negative refraction and focusing of electromagnetic waves by metallodielectric photonic crystals. *Phys. Rev. B*, 72:045124, 2005.
- [156] J. Li and C.T. Chan. Imaging using nano metallic films: from evanescent wave lens to resonant tunnelling lens. *ArXiv Physics e-prints*, page physics/0701172, 2007.
- [157] Qi Wu, John M. Gibbons, and W. Park. Graded negative index lens by photonic crystals. *Opt. Express*, 16(21):16941, 2008.
- [158] D. Schurig and D.R. Smith. Negative index lens aberrations. *Phys. Rev. E*, 70:065601, 2004.

-
- [159] J. Chen, C. Radu, and A. Puri. Aberration-free negative-refractive-index lens. *App. Phys. Lett.*, 88(7):071119, 2006.
- [160] V.N. Mahajan. *Optical imaging and aberrations, part I: ray geometrical optics*. SPIE, 1998.
- [161] N. Calander. Surface plasmon-coupled emission and Fabry-Perot resonance in the sample layer: a theoretical approach. *J. Phys. Chem. B*, 109(29):13957, 2005.
- [162] R. Kotyński and T. Stefaniuk. Multiscale analysis of subwavelength imaging with metal-dielectric multilayers. *Opt. Lett.*, 35(8):1133, 2010.
- [163] C.J. Zapata-Rodríguez, D. Pastor, L.E. Martínez, and J.J. Miret. Left-handed metamaterial coatings for subwavelength-resolution imaging. *J. Opt. Soc. Am. A*, 29(9):1992, 2012.
- [164] Z. Jakšić and M. Maksimović. Ordered artificial nanocomposites for imaging beyond diffraction limit. In *Proc. 1st International Workshop on Nanoscience & Nanotechnology*, page 147, Berlin, 2005.
- [165] K.J. Webb, M. Yang, D.W. Ward, and K.A. Nelson. Metrics for negative-refractive-index materials. *Phys. Rev. E*, 70(3):035602, 2004.
- [166] R. Kotyński, T.J. Antosiewicz, K. Król, and K. Panajotov. Two-dimensional point spread matrix of layered metal-dielectric imaging elements. *J. Opt. Soc. Am. A*, 28(2):111, 2011.
- [167] J.B. Pendry and S.A. Ramakrishna. Refining the perfect lens. *Phys. B Cond. Matter*, 338(1):329, 2003.

- [168] M. Scalora, M.J. Bloemer, A.S. Pethel, J.P. Dowling, C.M. Bowden, and A.S. Manka. Transparent, metallo-dielectric, one-dimensional, photonic band-gap structures. *J. Appl. Phys.*, 83(5):2377, 1998.
- [169] A. Yariv and P. Yeh. Electromagnetic propagation in periodic stratified media. II. Birefringence, phase matching, and X-ray lasers. *J. Opt. Soc. Am. A*, 67(4):438, 1977.
- [170] R.W. Ziolkowski. Propagation in and scattering from a matched metamaterial having a zero index of refraction. *Phys. Rev. E*, 70(4):046608, 2004.
- [171] M. Silveirinha and N. Engheta. Tunneling of electromagnetic energy through subwavelength channels and bends using ϵ -near-zero materials. *Phys. Rev Lett.*, 97(15):157403, 2006.
- [172] V. Torres, V. Pacheco-Peña, P. Rodríguez-Ulibarri, M. Navarro-Cía, M. Beruete, M. Sorolla, and N. Engheta. Terahertz epsilon-near-zero graded-index lens. *Opt. Express*, 21(7):9156, 2013.
- [173] P.A. Belov, C.R. Simovski, P. Ikonen, M.G. Silveirinha, and Y. Hao. Image transmission with the subwavelength resolution in microwave, terahertz, and optical frequency bands. *J. Commun. Technol. El+*, 52(9):1009, 2007.
- [174] H. Liu, Shivanand, and K.J. Webb. Subwavelength imaging opportunities with planar uniaxial anisotropic lenses. *Opt. Lett.*, 33(21):2568, 2008.
- [175] J. Elser, V.A. Podolskiy, I. Salakhutdinov, and I. Avrutsky. Nonlocal effects in effective-medium response of nanolayered metamaterials. *Appl. Phys. Lett.*, 90(19):191109, 2007.

-
- [176] A. Orlov, I. Iorsh, P. Belov, and Y. Kivshar. Complex band structure of nanostructured metal-dielectric metamaterials. *Opt. Express*, 21(2):1593, 2013.
- [177] J. Luo, H. Chen, B. Hou, P. Xu, and Y. Lai. Nonlocality-induced negative refraction and subwavelength imaging by parabolic dispersions in metal-dielectric multilayered structures with effective zero permittivity. *Plasmonics*, 8(2):1095, 2013.
- [178] J.B. Theeten, D.E. Aspnes, and R.P.H. Chang. A new resonant ellipsometric technique for characterizing the interface between GaAs and its plasma-grown oxide. *J. Appl. Phys.*, 49(12):6097, 1978.
- [179] J.T. Shen and P.M. Platzman. Near field imaging with negative dielectric constant lenses. *Appl. Phys. Lett.*, 80(18):3286, 2002.
- [180] A. Pastuszczyk and R. Kotyński. Optimized low-loss multilayers for imaging with sub-wavelength resolution in the visible wavelength range. *J. Appl. Phys.*, 109(8):084302, 2011.
- [181] C.J. Zapata-Rodríguez, D. Pastor, J.J. Miret, and S. Vuković. Uniaxial epsilon-near-zero metamaterials: from superlensing to double refraction. *J. Nanophoton.*, 8(1):083895, 2014.
- [182] N. Fabre, L. Lalouat, B. Cluzel, X. Mélique, D. Lippens, Fr. de Fornel, and O. Vanbésien. Optical near-field microscopy of light focusing through a photonic crystal flat lens. *Phys. Rev. Lett.*, 101(7):073901, 2008.
- [183] S. Kocaman, M.S. Aras, P. Hsieh, J.F. McMillan, C.G. Biris, N.C. Panoiu, M.B. Yu, D.L. Kwong, A. Stein, and C.W. Wong. Zero phase delay in

- negative-refractive-index photonic crystal superlattices. *Nat. Photonics*, 5 (8):499, 2011.
- [184] M. Conforti, M. Guasoni, and C. De Angelis. Subwavelength diffraction management. *Opt. Lett.*, 33(22):2662, 2008.
- [185] Y. Liu, G. Bartal, and X. Zhang. All-angle negative refraction and imaging in a bulk medium made of metallic nanowires in the visible region. *Opt. Express*, 16(20):15439, 2008.
- [186] C. Yan, D.H. Zhang, Y. Zhang, D. Li, and M.A. Fiddy. Metal-dielectric composites for beam splitting and far-field deep sub-wavelength resolution for visible wavelengths. *Opt. Express*, 18(14):14794, 2010.
- [187] C.J. Zapata-Rodríguez, D. Pastor, M.T. Caballero, and J.J. Miret. Diffraction-managed superlensing using plasmonic lattices. *Opt. Commun*, 285(16):3358, 2012.
- [188] G.R. Ayers and J.C. Dainty. Iterative blind deconvolution method and its applications. *Opt. Lett.*, 13(7):547, 1988.
- [189] P.Y. Rotha and D.M. Paganin. Blind phase retrieval for aberrated linear shift-invariant imaging systems. *New J. Phys.*, 12(7):073040, 2010.
- [190] D. Pastor, T. Stefaniuk, P. Wróbel, C.J. Zapata-Rodríguez, and R. Kotyński. Determination of the point spread function of layered metamaterials assisted with the blind deconvolution algorithm. *Opt. Quant. Electron.*, 47 (1):17–26, 2014.
- [191] J. DeVore. Refractive indices of rutile and sphalerite. *J. Opt. Soc. Am. A*, 41(6):416, 1951.

-
- [192] J.A. Stratton. *Electromagnetic theory*. McGraw-Hill, 1941.
- [193] J. Durnin. Exact solutions for nondiffracting beams. I. The scalar theory. *J. Opt. Soc. Am. A*, 4(4):651, 1987.
- [194] J. Durnin, J. Jr Miceli, and J.H. Eberly. Diffraction-free beams. *Phys. Rev. Lett.*, 58(15):1499, 1987.
- [195] J. Lu, J.F. Greenleaf, and E. Recami. Limited-diffraction solutions to Maxwell and to Schroedinger equations. *arXiv preprint physics/9610012*, 1996.
- [196] D. Mugnai, A. Ranfagni, and R. Ruggeri. Observation of superluminal behaviors in wave propagation. *Phys. Rev. Lett.*, 84(21):4830, 2000.
- [197] R.M. Herman and T.A. Wiggins. Production and uses of diffractionless beams. *J. Opt. Soc. Am. A*, 8(6):932, 1991.
- [198] A. Vasara, J. Turunen, and A.T. Friberg. Realization of general nondiffracting beams with computer-generated holograms. *J. Opt. Soc. Am. A*, 6(11):1748, 1989.
- [199] K. Uehara and H. Kikuchi. Generation of nearly diffraction-free laser beams. *Appl. Phys. B*, 48(2):125, 1989.
- [200] J. Lu, H. Zou, and J.F. Greenleaf. Biomedical ultrasound beam forming. *Ultrasound Med. Biol.*, 20(5):403, 1994.
- [201] J. Lu and J.F. Greenleaf. Evaluation of a nondiffracting transducer for tissue characterization. In *Proc. IUS*, page 795, 1990.

190 Bibliography

- [202] J. Lu, X. Xu, H. Zou, and J.F. Greenleaf. Application of Bessel beam for Doppler velocity estimation. *IEEE Trans. Ultrason. Ferroelectr. Freq. Control*, 42(4):649, 1995.
- [203] J.-Y. Lu and J.F. Greenleaf. Producing deep depth of field and depth-independent resolution in NDE with limited diffraction beams. *Ultrasonic Imaging*, 15(2):134, 1993.
- [204] V. Garcés-Chávez, D. McGloin, H. Melville, W. Sibbett, and K. Dholakia. Simultaneous micromanipulation in multiple planes using a self-reconstructing light beam. *Nature*, 419(6903):145, 2002.
- [205] D. McGloin, V. Garcés-Chávez, and K. Dholakia. Interfering Bessel beams for optical micromanipulation. *Opt. Lett.*, 28(8):657, 2003.
- [206] M.P. MacDonald, L. Paterson, K. Volke-Sepulveda, J. Arlt, W. Sibbett, and K. Dholakia. Creation and manipulation of three-dimensional optically trapped structures. *Science*, 296(5570):1101, 2002.
- [207] J. Arlt, V. Garces-Chavez, W. Sibbett, and K. Dholakia. Optical micromanipulation using a Bessel light beam. *Opt. Commun.*, 197(4):239, 2001.
- [208] D.P. Rhodes, G.P.T. Lancaster, J. Livesey, D. McGloin, J. Arlt, and K. Dholakia. Guiding a cold atomic beam along a co-propagating and oblique hollow light guide. *Opt. Commun.*, 214(1):247, 2002.
- [209] J. Fan, E. Parra, and H.M. Milchberg. Resonant self-trapping and absorption of intense Bessel beams. *Phys. Rev. Lett.*, 84(14):3085, 2000.
- [210] J. Arlt, T. Hitomi, and K. Dholakia. Atom guiding along Laguerre-Gaussian and Bessel light beams. *Appl. Phys. B*, 71(4):549, 2000.

-
- [211] M. Erdelyi, Z.L. Horvath, G. Szabo, Zs Bor, F.K. Tittel, J.R. Cavallaro, and M.C. Smayling. Generation of diffraction-free beams for applications in optical microlithography. *J. Vac. Sci. Technol., B*, 15(2):287, 1997.
- [212] R.W. Ziolkowski. Localized transmission of electromagnetic energy. *Phys. Rev. A*, 39(4):2005, 1989.
- [213] R.W. Ziolkowski. Localized wave physics and engineering. *Phys. Rev. A*, 44(6):3960, 1991.
- [214] J. Ježek, T. Čižmár, V. Nedela, and P. Zemánek. Formation of long and thin polymer fiber using nondiffracting beam. *Opt. Express*, 14(19):8506, 2006.
- [215] M.K. Bhuyan, F. Courvoisier, P.-A. Lacourt, M. Jacquot, L. Furfaro, M.J. Withford, and J.M. Dudley. High aspect ratio taper-free microchannel fabrication using femtosecond Bessel beams. *Opt. Express*, 18(2):566, 2010.
- [216] B. Hafizi, E. Esarey, and P. Sprangle. Laser-driven acceleration with Bessel beams. *Phys. Rev. E*, 55(3):3539, 1997.
- [217] Y.V. Kartashov, V.A. Vysloukh, and L. Torner. Rotary solitons in Bessel optical lattices. *Phys. Rev Lett.*, 93(9):093904, 2004.
- [218] T. Wulle and S. Herminghaus. Nonlinear optics of Bessel beams. *Phys. Rev. Lett.*, 70(10):1401, 1993.
- [219] L. Van Dao, K.B. Dinh, and P. Hannaford. Generation of extreme ultraviolet radiation with a Bessel-Gaussian beam. *Appl. Phys. Lett.*, 95(13):131114, 2009.
- [220] P. Polesana, A. Couairon, D. Faccio, A. Parola, M.A. Porras, A. Dubietis, A. Piskarskas, and P. Di Trapani. Observation of conical waves in focusing,

- dispersive, and dissipative Kerr media. *Phys. Rev. Lett.*, 99(22):223902, 2007.
- [221] D. Faccio and P. Di Trapani. Conical-wave nonlinear optics: From Raman conversion to extreme UV generation. *Laser Phys.*, 18(3):253, 2008.
- [222] H. Kano, D. Nomura, and H. Shibuya. Excitation of surface-plasmon polaritons by use of a zeroth-order Bessel beam. *App. Opt.*, 43(12):2409, 2004.
- [223] Q. Zhan. Evanescent Bessel beam generation via surface plasmon resonance excitation by a radially polarized beam. *Opt. Lett.*, 31(11):1726, 2006.
- [224] A. Bouhelier, F. Ignatovich, A. Bruyant, C. Huang, G. Colas des Francs, J.-C. Weeber, A. Dereux, G.P. Wiederrecht, and L. Novotny. Surface plasmon interference excited by tightly focused laser beams. *Opt. Lett.*, 32(17):2535, 2007.
- [225] W. Chen and Q. Zhan. Realization of an evanescent Bessel beam via surface plasmon interference excited by a radially polarized beam. *Opt. Lett.*, 34(6):722, 2009.
- [226] K.J. Moh, X.-C. Yuan, J. Bu, S.W. Zhu, and B.Z. Gao. Radial polarization induced surface plasmon virtual probe for two-photon fluorescence microscopy. *Opt. Lett.*, 34(7):971, 2009.
- [227] S. Longhi, D. Janner, and P. Laporta. Propagating pulsed Bessel beams in periodic media. *J. Opt. B-Quantum S. O.*, 6(11):477, 2004.
- [228] W.B. Williams and J.B. Pendry. Generating Bessel beams by use of localized modes. *J. Opt. Soc. Am. A*, 22(5):992, 2005.

-
- [229] C.J. Zapata-Rodríguez, M.T. Caballero, and J.J. Miret. Angular spectrum of diffracted wave fields with apochromatic correction. *Opt. Lett.*, 33(15): 1753, 2008.
- [230] A.V. Novitsky and L.M. Barkovsky. Total internal reflection of vector Bessel beams: Imbert-Fedorov shift and intensity transformation. *J. Opt. A-Pure Appl. Opt.*, 10(7):075006, 2008.
- [231] V.N. Belyi, N.S. Kazak, S.N. Kurilkina, and N.A. Khilo. Generation of TE- and TH-polarized Bessel beams using one-dimensional photonic crystal. *Opt. Commun.*, 282(10):1998, 2009.
- [232] D. Mugnai and P. Spalla. Electromagnetic propagation of Bessel-like localized waves in the presence of absorbing media. *Opt. Commun.*, 282(24): 4668, 2009.
- [233] G. Rui, Y. Lu, P. Wang, H. Ming, and Q. Zhan. Evanescent Bessel beam generation through filtering highly focused cylindrical vector beams with a defect mode one-dimensional photonic crystal. *Opt. Commun.*, 283(10): 2272, 2010.
- [234] J. Durnin, J.H. Eberly, and J.J. Miceli. Comparison of Bessel and Gaussian beams. *Opt. Lett.*, 13(2):79, 1988.
- [235] O. Manela, M. Segev, and D.N. Christodoulides. Nondiffracting beams in periodic media. *Opt. Lett.*, 30(19):2611, 2005.
- [236] A. Salandrino and D.N. Christodoulides. Airy plasmon: a nondiffracting surface wave. *Opt. Lett.*, 35(12):2082, 2010.
- [237] H.M. Antia. *Numerical methods for scientists and engineers*. Amer. Math. Soc., 2012.

194 Bibliography

- [238] C.J. Zapata-Rodríguez, S. Vuković, M.R. Belić, D. Pastor, and J.J. Miret. Nondiffracting Bessel plasmons. *Opt. Express*, 19(20):19572, 2011.
- [239] J.J. Miret, D. Pastor, and C.J. Zapata-Rodríguez. Subwavelength surface waves with zero diffraction. *J. Nanophoton.*, 5(1):051801, 2011.
- [240] A.H. Sihvola. *Electromagnetic mixing formulas and applications*. Institution of Electrical Engineers, 1999.
- [241] G.B. Arfken, H.J. Weber, and F.E. Harris. *Mathematical methods for physicists: a comprehensive guide*. Elsevier, 2012.
- [242] M.V. Berry and N.L. Balazs. Nonspreading wave packets. *Am. J. Phys.*, 47(3):264, 1979.
- [243] K. Unnikrishnan and A.R.P. Rau. Uniqueness of the Airy packet in quantum mechanics. *Am. J. Phys.*, 64(8):1034, 1996.
- [244] G.A. Siviloglou and D.N. Christodoulides. Accelerating finite energy Airy beams. *Opt. Lett.*, 32(8):979, 2007.
- [245] G.A. Siviloglou, J. Broky, A. Dogariu, and D.N. Christodoulides. Observation of accelerating Airy beams. *Phys. Rev. Lett.*, 99(21):213901, 2007.
- [246] J.C. Gutiérrez-Vega, M.A. Bandrés-Motola, and S. Chávez-Cerda. Parabolic beams: a new class of invariant optical fields. *Opt. Lett.*, 25:1493, 2000.
- [247] G.A. Siviloglou, J. Broky, A. Dogariu, and D.N. Christodoulides. Ballistic dynamics of Airy beams. *Opt. Lett.*, 33(3):207, 2008.
- [248] J. Baumgartl, M. Mazilu, and K. Dholakia. Optically mediated particle clearing using Airy wavepackets. *Nat. Photonics*, 2(11):675, 2008.

-
- [249] J. Broky, G.A. Siviloglou, A. Dogariu, and D.N. Christodoulides. Self-healing properties of optical Airy beams. *Opt. Express*, 16(17):12880, 2008.
- [250] H.I. Sztul and R.R. Alfano. The Poynting vector and angular momentum of Airy beams. *Opt. Express*, 16(13):9411, 2008.
- [251] P. Zhang, J. Prakash, Z. Zhang, M.S. Mills, N.K. Efremidis, D.N. Christodoulides, and Z. Chen. Trapping and guiding microparticles with morphing autofocusing Airy beams. *Opt. Lett.*, 36(15):2883, 2011.
- [252] Z. Zheng, B.-F. Zhang, H. Chen, J. Ding, and H.-T. Wang. Optical trapping with focused Airy beams. *Appl. Opt.*, 50(1):43, 2011.
- [253] P. Rose, F. Diebel, M. Boguslawski, and C. Denz. Airy beam induced optical routing. *App. Phys. Lett.*, 102(10):101101, 2013.
- [254] H. Choi, D.F. Pile, S. Nam, G. Bartal, and X. Zhang. Compressing surface plasmons for nano-scale optical focusing. *Opt. Express*, 17(9):7519, 2009.
- [255] V.J. Sorger, Z. Ye, R.F. Oulton, Y. Wang, G. Bartal, X. Yin, and X. Zhang. Experimental demonstration of low-loss optical waveguiding at deep sub-wavelength scales. *Nat. Commun.*, 2:331, 2011.
- [256] A. Vakil and N. Engheta. Transformation optics using graphene. *Science*, 332(6035):1291, 2011.
- [257] V.E. Demidov, S. Urazhdin, and S.O. Demokritov. Direct observation and mapping of spin waves emitted by spin-torque nano-oscillators. *Nat. Mater.*, 9(12):984, 2010.

- [258] A. Minovich, A.E. Klein, N. Janunts, T. Pertsch, D.N. Neshev, and Y.S. Kivshar. Generation and near-field imaging of Airy surface plasmons. *Phys. Rev. Lett.*, 107(11):116802, 2011.
- [259] P. Zhang, S. Wang, Y. Liu, X. Yin, C. Lu, Z. Chen, and X. Zhang. Plasmonic Airy beams with dynamically controlled trajectories. *Opt. Lett.*, 36(16):3191, 2011.
- [260] L. Li, T. Li, S.M. Wang, C. Zhang, and S.N. Zhu. Plasmonic Airy beam generated by in-plane diffraction. *Phys. Rev. Lett.*, 107(12):126804, 2011.
- [261] I. Epstein and A. Arie. Dynamic generation of plasmonic bottle-beams with controlled shape. *Opt. Lett.*, 39(11):3165, 2014.
- [262] A.E. Klein, A. Minovich, M. Steinert, N. Janunts, A. Tünnermann, D.N. Neshev, Y.S. Kivshar, and T. Pertsch. Controlling plasmonic hot spots by interfering Airy beams. *Opt. Lett.*, 37(16):3402, 2012.
- [263] P. Zhang, S. Wang, Y. Liu, X. Yin, C. Lu, Z. Chen, and X. Zhang. Dynamically routing surface plasmon polaritons along arbitrary trajectories. In *Proc. CLEO*, page QF1D.1, 2012.
- [264] I. Dolev, I. Epstein, and A. Arie. Surface-plasmon holographic beam shaping. *Phys. Rev. Lett.*, 109(20):203903, 2012.
- [265] I. Epstein and A. Arie. Arbitrary bending plasmonic light waves. *Phys. Rev. Lett.*, 112(2):023903, 2014.
- [266] W. Liu, D.N. Neshev, I.V. Shadrivov, A.E. Miroshnichenko, and Y.S. Kivshar. Plasmonic Airy beam manipulation in linear optical potentials. *Opt. Lett.*, 36(7):1164, 2011.

-
- [267] F. Bleckmann, A. Minovich, J. Frohnhaus, D.N. Neshev, and S. Linden. Manipulation of Airy surface plasmon beams. *Opt. Lett.*, 38(9):1443, 2013.
- [268] T. Zentgraf, Y. Liu, M.H. Mikkelsen, J. Valentine, and X. Zhang. Plasmonic Luneburg and Eaton lenses. *Nat. Nanotechnol.*, 6(3):151, 2011.
- [269] N.K. Efremidis. Airy trajectory engineering in dynamic linear index potentials. *Opt. Lett.*, 36(15):3006, 2011.
- [270] A.V. Novitsky and D.V. Novitsky. Nonparaxial Airy beams: role of evanescent waves. *Opt. Lett.*, 34(21):3430, 2009.
- [271] L.G. Gouy. Sur une propriété nouvelle des ondes lumineuses. *Compt. Rendue Acad. Sci. (Paris)*, (110):1251, 1890.
- [272] S. Feng and H.G. Winful. Physical origin of the Gouy phase shift. *Opt. Lett.*, 26(8):485, 2001.
- [273] T.D. Visser and E. Wolf. The origin of the Gouy phase anomaly and its generalization to astigmatic wavefields. *Opt. Commun.*, 283(18):3371, 2010.
- [274] R.W. Boyd. Intuitive explanation of the phase anomaly of focused light beams. *J. Opt. Soc. Am. A*, 70(7):877, 1980.
- [275] A.E. Siegman. *Lasers*. University Science Books, 1986.
- [276] G.G. Paulus, F. Lindner, H. Walther, A. Baltuška, E. Goulielmakis, M. Lezius, and F. Krausz. Measurement of the phase of few-cycle laser pulses. *Phys. Rev. Lett.*, 91(25):253004, 2003.
- [277] A. Apolonski, P. Dombi, G.G. Paulus, M. Kakehata, R. Holzwarth, Th. Udem, Ch. Lemell, K. Torizuka, J. Burgdörfer, and Theodor W. Hänsch.

198 Bibliography

- Observation of light-phase-sensitive photoemission from a metal. *Phys. Rev. Lett.*, 92(7):073902, 2004.
- [278] X. Pang, G. Gbur, and T.D. Visser. The Gouy phase of Airy beams. *Opt. Lett.*, 36(13):2492, 2011.
- [279] M.A. Bandres. Accelerating beams. *Opt. Lett.*, 34(24):3791, 2009.
- [280] P. Polynkin, M. Kolesik, J.V. Moloney, G.A. Siviloglou, and D.N. Christodoulides. Curved plasma channel generation using ultraintense Airy beams. *Science*, 324(5924):229, 2009.
- [281] J. Baumgartl, M. Mazilu, and K. Dholakia. Optically mediated particle clearing using Airy wavepackets. *Nat. Photonics*, 2(11):675, 2008.
- [282] M.A. Porras, C.J. Zapata-Rodríguez, and I. Gonzalo. Gouy wave modes: undistorted pulse focalization in a dispersive medium. *Opt. Lett.*, 32(22):3287, 2007.
- [283] C.J. Zapata-Rodríguez and M.A. Porras. Controlling the carrier-envelope phase of few-cycle focused laser beams with a dispersive beam expander. *Opt. Express*, 16(26):22090, 2008.
- [284] C.J. Zapata-Rodríguez, D. Pastor, and J.J. Miret. Considerations on the electromagnetic flow in Airy beams based on the Gouy phase. *Opt. Express*, 20(21):23553, 2012.
- [285] J. Plumridge, E. Clarke, R. Murray, and C. Phillips. Ultra-strong coupling effects with quantum metamaterials. *Solid State Commun.*, 146(9):406, 2008.

- [286] A. Mandatori and M. Bertolotti. Spectral properties for 1D multilayer systems and application to super resolution. *J. Eur. Opt. Soc-Rapid*, 6, 2011.
- [287] C.A. Balanis. *Advanced engineering electromagnetics*. Wiley, 2012.